Ordered arrangements of selective-area grown MnAs nanoclusters as components for novel, planar magneto-electronic devices

Flächenselektiv gewachsene MnAs-Nanocluster als Bausteine für neuartige, planare, magnetoelektronische Bauteile

Dissertation
zur Erlangung des Doktorgrades
der Naturwissenschaften
(Dr. rer. nat.)

vorgelegt von

Martin Fischer, M.Sc.

betreut durch Prof. Dr. Peter J. Klar

2015

Contents

Part I

Introduction

The discovery of the Giant magnetoresistance (GMR) had a massive impact on science, technology and industry regarding non-volatile storage media. New possibilities for the miniaturization of magnetoresistive (MR) structures arose and offered pathways for novel devices with a previously unimaginable performance.[Par95 Pri98] Today, a multi billion dollar market is depending on devices based on GMR and tunnel-magnetoresistance (TMR) effects.[Rei09] In addition to that, novel concepts such as racetrack memory devices or planar logic elements based on ferromagnetic materials are subject of today's research.[All02 All05 Par08 Wol01] However, there are certain limits which will have to be faced by the established technology.

The common way to achieve a miniaturized MR device starts with a macroscopic set of layers which is miniaturized by an etching process. Also common planar approaches are based on an etching process performed on a macroscopic magnetic layer.[Gou07] Since etching is a controlled destruction and removal of material, it also has an impact on the properties of the residual structure. While wet-chemical etching offers poor controllability of its parameters concerning nanoscale processes, the favorable technique of physical etching induces damage in the vicinity the surface: Plasma and (focused-) ion beam etching methods are based on kinetic processes, which involve sputter events leading to hardly controllable damage in the designated device areas.[Rey01] With device sizes on the two-digit nanometer scale, this may strongly affect the performance, lifetime and production outcome of high-performance magnetoresistive devices. The research on the avoidance of etching-induced damage has become a central aspect in the research on new miniaturized magnetoresistive device concepts. Thus, new approaches and possibilities need to be considered to keep up an ongoing miniaturization. Additionally, the classical approach shows limited possibilities concerning the integrability into more complex electric circuits. The possibility of easily integratable nanoscopic magnetic structures seems inspiring yet ambitious.[Aws07] A promising model kit for novel approaches can be found by combining such magnetic structures with the III-V semiconductor family.[Ala11]

Manganese arsenide (MnAs) is a metallic material which shows ferromagnetism at room temperature. Up to now, it has attracted most attention in combination with GaAs, either as MnAs/GaAs hybrid system or as ternary dilute magnetic semiconductor (DMS) (Ga,Mn)As.[Ohn96 Eid13 Gid05 Ye03] In particular, the hybrid materials are based on synthesis processes including self-assembly mechanisms, which offer the possibility of controlling the obtained structural properties (e.g.

grain sizes or -densities in hybrid structures) by tuning the growth process parameters. However, they do not allow the exact determination of the size, shape and position of a single grain in the matrix. Additionally, the obtainable Curie temperatures for (Ga,Mn)As alloys are also still far below room temperature, which poses significant limitations for their application suitability.[Che11] However, it is possible to grow sub-micrometer sized ferromagnetic crystalline MnAs grains, called 'nanoclusters', by a selective area metal-organic vapor-phase epitaxy (SA-MOVPE) process. This approach combines the versatility and material quality of MOVPE with the precision of electron-beam lithography. This is achieved by a mask patterning process of a growth-inhibiting layer on the (111) face of GaAs wafers. The growth on GaAs wafers provides the integrability into III-V based concepts, which play a huge role in the modern semiconductor research and industry. The obtainable crystal quality, controllability of position and size of the nanoclusters grown as well as their magnetic properties have been subject of numerous publications.[Har06 Har08 El10a El11a El11b Har02] The Curie temperature of GaAs:Mn/MnAs hybrid systems can reach values of up to 340 K, which is significantly above room temperature and thus in a region of high interest for applications.[Kru06] In addition, the magnetic properties of MnAs show several interesting anisotropy effects, which will be furtherly addressed in what follows.

SA-MOVPE yields the opportunity of not only freely defining the size of the grown nanoclusters, but also controlling its shapes and exact positions on the sample as desired. This means that one can freely design nanoscale arrangements built up from ferromagnetic nanoclusters, while the possibilities of combining those structures with other materials, such as nonmagnetic metals, are widespread. Since the positions of the SA-MOVPE grown structures are exactly known, the application of more than one lithography process for the device build-up is possible with sufficiently precise aligning techniques.

The listed properties of MnAs as material together with the possibilities offered by SA-MOVPE as the growth method of choice form an inspiring construction kit for novel magneto-electronic device structures based on a planar geometry. Recently, Heiliger et al. have investigated domain interfaces in MnAs nanocluster arrangements by ab-initio calculations, in order to access their MR properties. Here, MR ratios of up to 300% were achieved in idealized systems. In this publication, the MR is described as a function of the relative angle of the magnetizations of the involved two domains. The next step after the exploration of SA-MOVPE as a suitable growth process for ferromagnetic MnAs nanoclusters and the prediction of possibly high and thus technologically interesting MR ratios is the realization of GMR-like device schemes based on this material system, and the experimental exploration of the properties these arrangements

are offering. The presented work will give a short overview of the material system and the synthesis techniques used as well as of related physical concepts. Afterwards, the performance of GMR-like MnAs device structures will be investigated, and the influence of thermal effects on the observed phenomena will be evaluated.

1 Manganese arsenide nanocluster arrangements

The field of III-V compound semiconductor materials is one of the most important cornerstones in today's semiconductor industry. The III-V compounds are commonly categorized by the group V elements involved as nitrides (N), phosphides (P), arsenides (As) or antimonides (Sb). One central advantage of this group of materials is that they possess a comparatively widespread variety of different bandgaps, starting from InSb with a gap of 0.18 eV[Kit91] going up to AlN with 6.2 eV[Chr94], both at room temperature. Regarding ternary or quarternary compounds, it becomes possible to tune the bandgap freely between the binary materials' values by varying the stoichiometry of the respective alloy. Amongst others, this advantage has lead to numerous industrial products based on III-V materials, such als many LED concepts or highly efficient solar cells. Thereby, the most common and nearly exclusively used synthesis method is epitaxial growth. Amongst the III-V family, GaAs plays a major role as building block for heterostructures in the (Al,Ga)As system or as the basic material for low noise devices. It is an intrinsic semiconductor with a direct bandgap of 1.43 eV.

The whole functionality of common semiconductor electronic devices is based on the charge of the electron and its transport through material. The introduction of magnetic phenomena introduces a whole new dimension, since the spin of the electron and the interaction with magnetic properties of materials can be used as tools in the processing, transfer and storage of information. Possible application concepts are manifold, and some *spin-tronic*, i.e. spin-electronic, concepts have already found their way into the market: magnetoresistive random access memory (MRAM) storage devices, for example, are commercially available for several years now.[Fre06] Their principle is based on the data storage in miniaturized cells consisting of two ferromagnetic domains, one of them with a free, switchable magnetization containing the information and one with a fixed magnetization serving as a reference. They are separated by an insulating layer, which forms a magnetic tunnel junction. The entire arrangement takes on different resistance values depending on the relative angle between the magnetizations of the two ferromagnetic layers.[Khv13] The combination of conventional electronics with spin-dependent components in optical devices is named *spin-optoelectronics*. An example for this category of devices is a vertical-cavity surface-emitting laser (VCSEL), which yields circular polarized coherent light when it is run on a spin-polarized current. This spin polarization can be induced by a ferromagnetic layer in the device setup.[Hol05]

Both exemplarily shown concepts (logical electronic elements in case of the MRAM and a multilayer, GaAs-based VCSEL setup in case of the circular polarized laser) take advantage of

spin-dependent phenomena (free and reference layer in the MRAM cells and the spin-polarization layer in the VCSEL). This demonstrates the importance of a controllable integration of magnetic materials into the growth processes of classical semiconducting devices. The synthesis of the circular polarized VCSEL, which is based on the above-mentioned III-V-semiconductor GaAs, accomplishes this with a special approach: the *dilute magnetic semiconductor* (DMS), alloying a semiconductor (here: GaAs) with a chemical element exhibiting large localized magnetic moments (here: Mn) in order to obtain a ferromagnetic material. The main goal of this approach is to combine the advantages and properties of both semiconductors and ferromagnetic materials not only in one device, but in one *material*. The pioneering work in this field was performed by the group of Hideo Ohno in the late 1980s, when ferromagnetism could be observed first in manganese doped III-V-compound semiconductors (In,Mn)As and later (Ga,Mn)As[Mun89]. This accomplishment is prominent in particular because III-V-materials show a comparatively poor solubility for the introduction of ferromagnetic elements. Later, a manifold of possible device applications has been proposed and demonstrated, for example utilizing nanostructured DMS layers as possible building blocks for storage media[Pap07]. However, these applications are mostly constricted to laboratory conditions, since the Curie temperatures of the most DMS are far below room temperature. The highest Curie temperatures observed for (Ga,Mn)As up to now do not exceed values of about 200 K[Che11 Jun05].

As an alternative approach for achieving ferromagnetism at higher Curie temperatures in a semiconducting material, one may introduce ferromagnet-semiconductor hybrid materials. The ferromagnetic material is not dissolved in the semiconductor here, forming an alloy as in the case of a DMS, but it is present as small ferromagnetic clusters in a semiconducting matrix. For the III-V material family, it is suitable to use MnAs nanoclusters for the synthesis of such hybrid materials, since it shares a common atom with GaAs, which supports the thermodynamical stability. In addition, it can be grown epitaxially on GaAs, and the arsenic precursor material which is needed for the growth procedure can be used for both GaAs and MnAs growth[Tan02]. The Curie temperature of bulk MnAs is about $T_C = 330\,\mathrm{K}$, while for MnAs nanoclusters, a slightly higher T_C of 340 K has been observed.[Har02 El10a] This is a strong advantage compared to DMS materials, whose T_C is, as mentioned, significantly lower.

Manganese arsenide (MnAs) is a polymorphic material. Okamoto defines three phases with a stoichiometry of $\frac{n_{\mathrm{Mn}}}{n_{\mathrm{As}}} = 1$:[Oka89]

α-MnAs It exists in a NiAs-type crystal structure (see figure 1) and shows ferromagnetic behavior. At about 40 °C, it performs a polymorphic transition to β-MnAs.[Das03]

β-MnAs β-MnAs is paramagnetic and crystallizes in a MnP-type structure.

γ-MnAs This paramagnetic phase exists above 125 °C, and crystallizes in NiAs type.

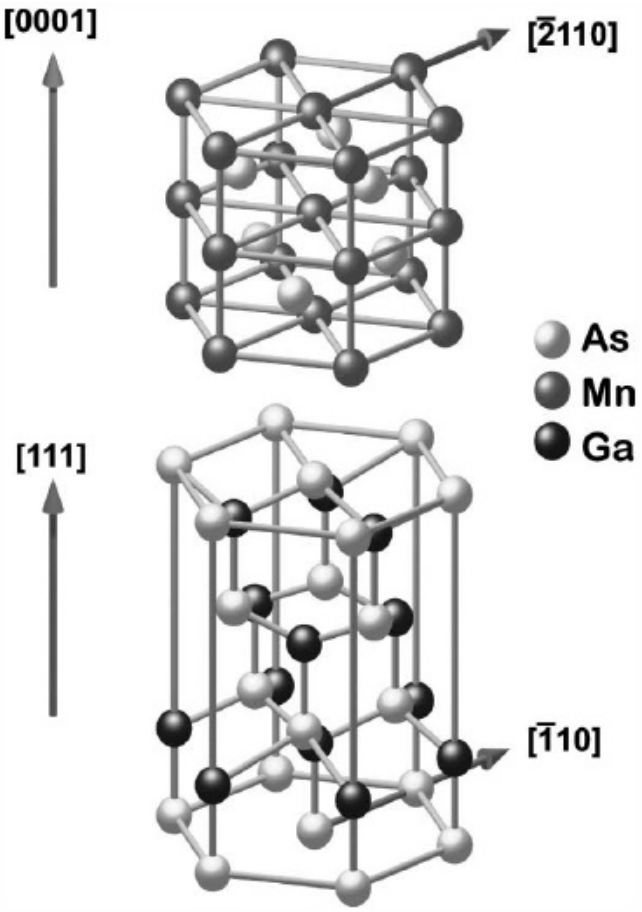

Figure 1: Upper structure: MnAs crystallizing in NiAs-type. Lower structure: Zincblende-type GaAs oriented along the (111) direction. Image taken from[Kae02]

Since this work focuses on the investigation of novel ferromagnetic nanostructures, the only suitable and interesting phase for our considerations is α-MnAs, which is stable at room temperature and at all temperatures below. In the following, the expression "MnAs" always refers to this phase, if not explicitly stated otherwise.

When grown on single crystalline GaAs, the orientation of the deposited MnAs layer is determined by the orientation of the substrate surface[Mor97]. The [111]B-surface of GaAs forms a pseudo-hexagonal lattice which is suitable for any epitaxial growth of MnAs in its [0001]-direction, as depicted in figure 1[Kae02]. Using [0001]-grown MnAs, the synthesis of a layered TMR

device structure has been demonstrated[Sug02] and much work on the properties of unordered, self-assembled MnAs nanocluster systems has been published[Elm08 El10a Har06 Joh10 Kru06 Har02 Har12]. However, both approaches for ferromagnet-semiconductor hybrids show strong restrictions concerning the miniaturizability.

1.1 SA-MOVPE growth

MnAs can be grown on GaAs substrates by a MOVPE deposition process. The direct deposition of a metal alloy like MnAs from its elements for example by an evaporization process, demands very high temperatures, since the melting and boiling points of the elemental substances at standard conditions are usually comparatively high. The stoichiometry and growth rate (which influences the achievable crystal structure quality) are difficult to control in such a synthesis process. MOVPE uses metal-organic compounds as precursors, which possess much lower melting and boiling points as the involved metallic elements. The precursors come into contact with the substrate in their gaseous states, using an inert gas as a carrier gas in the reactor. At a defined substrate temperature, the metal-organic precursors decompose on the substrate and the metal atoms may react to form the desired compound. Besides metal-organic precursors, one may also add anorganic gases like AsH_3 or SiH_4 to the reactor, which offers a high variety of possible compounds to be grown. Since the process is completely based on gas phase reactions, the amounts of the involved substances can be adjusted very precisely by controlling their gas flow into the reactor.
Highlighted by this advantages, MOVPE is one of the most important synthesis methods in today's semiconductor industry and research. By the use of self-assembly mechanisms depending on the combination of substrate, precursors and reaction conditions, it is possible to control the structural properties of the grown material very well, which enables the growth of layers as well as lower-dimensional structures like quantum dots or nanowires.[For08 Pet94] This is mainly sufficient for the use in collective processes, for example the use of cluster structures as active material in a quantum dot laser device. If one requires a precise control of a structure's position, size and shape, additional measures have to be taken.

Selective area MOVPE (SA-MOVPE) introduces a top-down pre-patterning process for a precise control of the MOVPE growth.[Kom11] Before growth, the substrates are covered with a thin layer of a growth-inhibiting material. By using electron-beam lithography followed by a dry-etching process, precisely-defined openings in the growth-inhibiting layer are achieved, which results in a mask pattern defining the desired structure to be grown. In these openings, the surface of the substrate is exposed, and in the following MOVPE process, the deposited

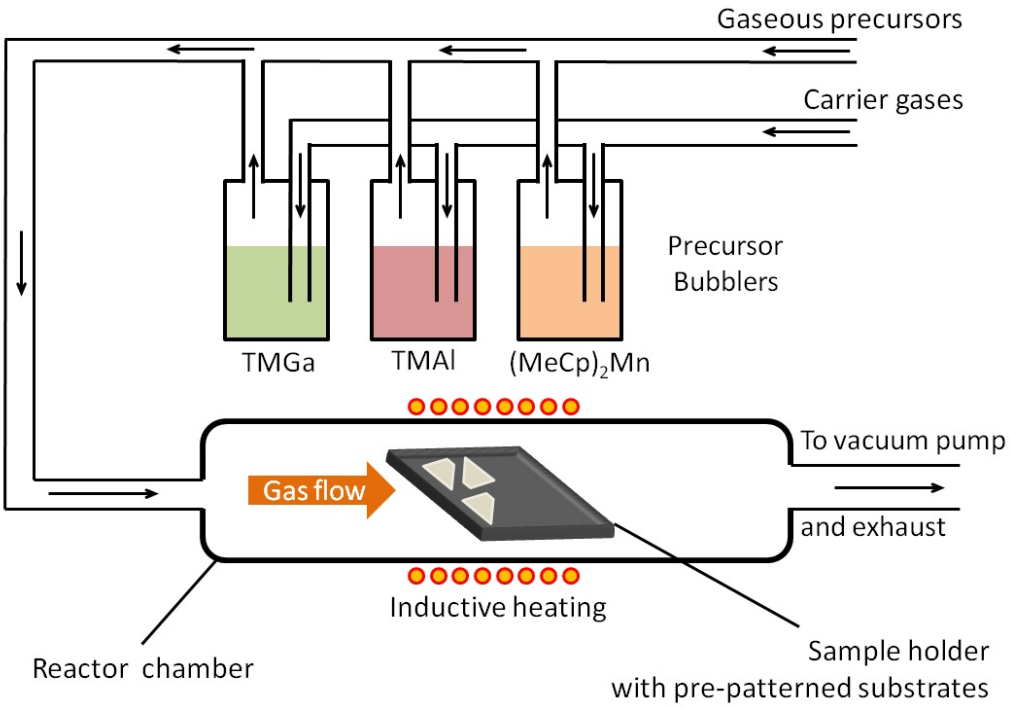

Figure 2: Schematic, simplified drawing of a MOVPE reactor system with precursor bubblers, gas piping, growth reactor and sample holder.

material will preferentially grow in the mask openings previously etched free. The adaption of the growth parameters and the mask pattern structure offers the possibility of a growth taking place exclusively in the mask openings, which practically leads to an accurate control of size, shape and position of the MOVPE-grown material.

In case of MnAs growth directly on GaAs, Wakatsuki et al. have presented a suitable growth process with parameters yielding a good area selectivity [Wak09]. Here, the precursor Bis(methylcyclopentadienyl)manganese ($(MeCp)_2Mn$) is used as organometallic source for manganese. An approximately 30 nm thick SiO_2-layer serves as growth inhibiting mask layer on the GaAs (111)B-substrates. The arsenic is provided by gaseous arsine (AsH_3). Several different parameter sets concerning the V/Mn-ratio were applied to identify a suitable parameter window for an optimized area-selective growth. The variation of the precursor concentration ratio at a fixed growth temperature of 750 °C showed that the selectivity gets well-defined for a high V/Mn-ratio, which expresses itself in a lower density of clusters on the SiO_2-layer. The influence of the growth temperature was evaluated at two different temperatures, 750 °C and 850 °C, with an identical, fixed precursor ratio of V/Mn = 1125. At 850 °C, a very good area selectivity could be observed, showing no growth on the SiO_2-mask.
Besides the growth parameters, the quality of the nanoclusters as well as the area selectivity

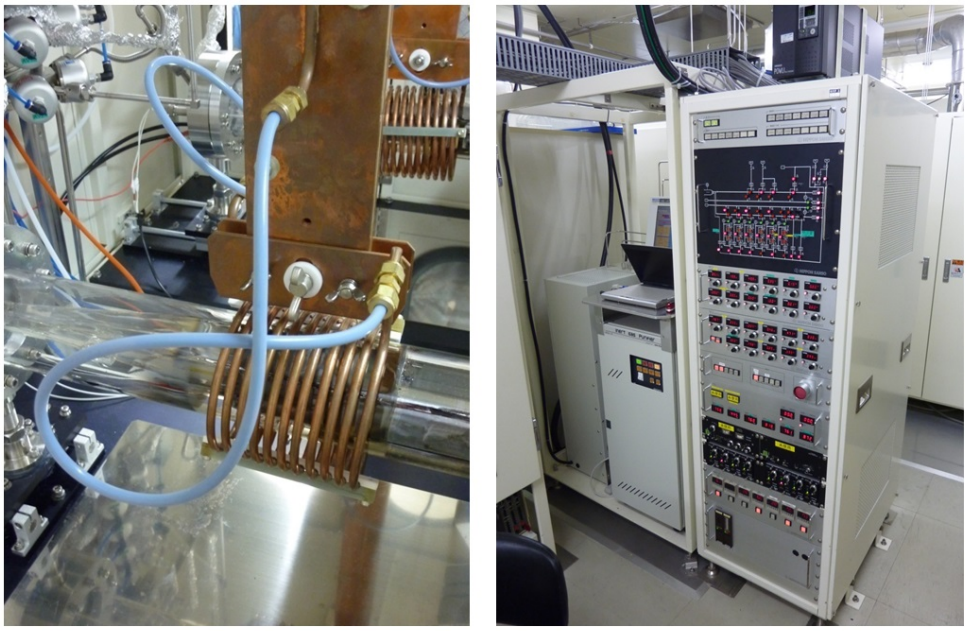

Figure 3: The MOVPE system which was used for the growth of the investigated MnAs nanocluster samples. Left image: the growth reactor surrounded by the inductive heating coil. Right image: control panel for the precursor and purge gas regulation, driven automatically by a personal computer.

are also enhanced by a buffer area consisting of large openings in the SiO_2-layer which surround the nanocluster structures. These buffer areas can be seen in figure 4. Their purpose can be interpreted as a disposal area, where exuberant amounts of precursor material can be deposited during the growth process.
In case of the MnAs nanoclusters used in this work, the growth process is performed with slightly different parameters and enhanced by the deposition of a buffer layer, consisting of (Al,Ga)As with an Al content of about 10 to 20 %,[Kom11] which is grown prior to the MnAs deposition. This layer serves several purposes:

- The (Al,Ga)As buffer layer yields better growth results for the MnAs clusters, especially concerning the uniformity of the grown structures[Ito09].
- It reduces diffusion processes between the GaAs substrate and the MnAs clusters during growth.
- Since the MnAs clusters are supposed to undergo electrical characterization, the (Al,Ga)As layer additionally isolates them electrically from the substrate.

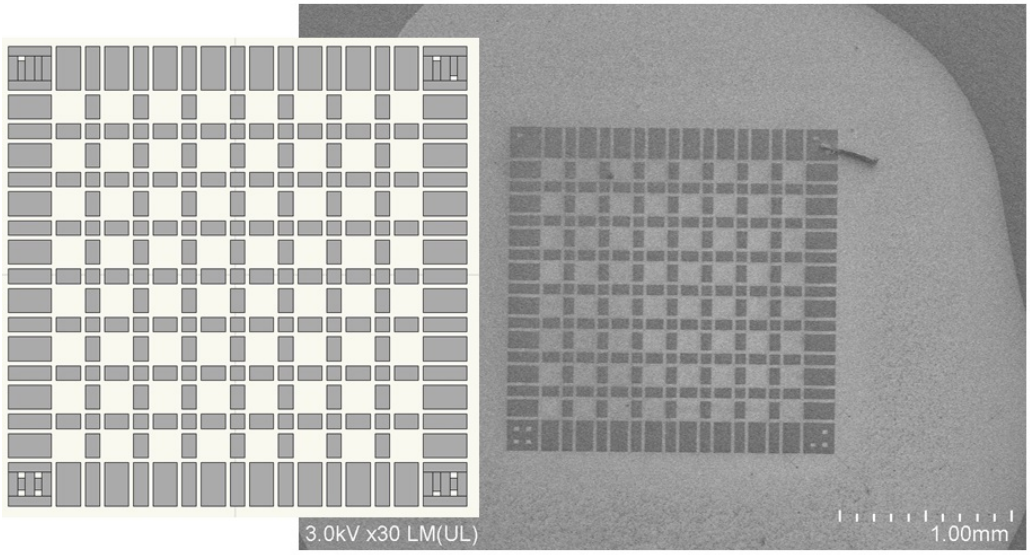

Figure 4: Buffer areas surrounding the 8x8 nanocluster pattern structure.

The buffer layer is grown at a temperature of 750 °C for two minutes with an AsH_3 partial pressure of 81 Pa, a tri-methyl-gallium (TMGa) partial pressure of 1.8 mPa and a tri-methyl-aluminum (TMAl) partial pressure of 0.3 mPa.

Directly after the growth of the buffer layer, the MnAs nanoclusters are grown, which secures an optimized and non-contaminated interface between the two materials. The growth of MnAs takes place at 800 °C for 10 minutes at partial pressures of 52.4 Pa for $(MeCp)_2Mn$ and 58.8 Pa for AsH_3, which yields a V/Mn - ratio of 1120.

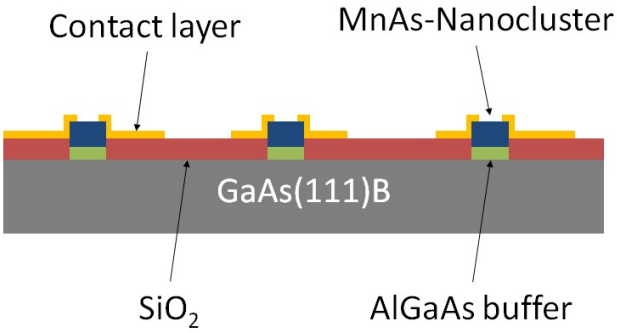

Figure 5: Schematic sectional drawing of the layer structures of the MnAs nanocluster samples. The growth-inhibiting SiO_2-layer, the (Al,Ga)As buffer layer, the MnAs nanoclusters, the contacts and the substrate are shown.

With constant growth parameters, the shape of the clusters is strongly determined by the mor-

phology of the openings in the SiO_2-mask layer. Since these openings are generated by a mostly isotropic plasma etching step through a resist mask generated by electron-beam lithography (EBL), their depths as well as their widths depend strongly on the applied EBL dose. On each sample which has been prepared for this thesis, the EBL dose is varied over eight different values to achieve a higher variety of mask opening profiles. This variation shows that a small dose, yielding comparatively shallow and narrow openings, leads to a MnAs growth showing clearly the hexagonally arranged cluster facets in the (0001) layer. The facets and edges of the cluster appear to be flat and well-defined. However, the lateral aspect ratio of the elongated MnAs clusters is comparatively low in this case, and the MnAs seems to have grown over the SiO_2-layer near the openings.
For a high EBL dose, the mask openings are etched deeper and wider. In this case, the MnAs growth is more strictly limited to the area of the openings, which yields a higher controllability of the cluster shape, resulting also in comparatively high aspect ratios. However, the cluster's facets are less distinct here, and the edges tend to show a more disrupted and less flat structure, which indicates possible structural defects like dislocations. SEM images showing the impact of the EBL dose on the clusters based on an identical pattern can be seen in figure 6.
The reason for this dependence between EBL dose and cluster shape might be found in the influence of the etching process on the substrate material as well as directly in the mask opening's morphology. Plasma etching causes disruptions in the material near the ablated volume.[Rah01] In case of the smaller openings written with lower EBL dose, this effect is less pronounced, which provides a better substrate crystal quality for the growth, resulting in better articulated crystal facets. At the same time, the samples with lower EBL dose show higher growth rates in the lateral direction over the SiO_2-layer. For the samples written with higher EBL dose, this effect is reduced or completely inhibited, since the deeper etching profile limits growth to the vertical direction. However in this case, the disruption of the substrate material is supposed to be stronger, resulting in less facet-like and less flat-edged cluster structures.

Since the MnAs nanocluster samples are based on a layout comprehending 8x8 fields with 8 different structure patterns and 8 different EBL dose values each, the cluster quality on one sample varies strongly. This enables one to choose the desired suitable and qualitatively best cluster arrangements for the subsequent electrical contacting procedure. Different EBL doses as well as the variation of the arrangement geometries and mask opening distances in the initial pattern design assures a high probability of usable and interesting MnAs nanocluster arrangements on each sample. After growth, the samples are investigated by SEM to identify areas of suitable quality and to choose possible candidate arrangements for the electrical characterization.

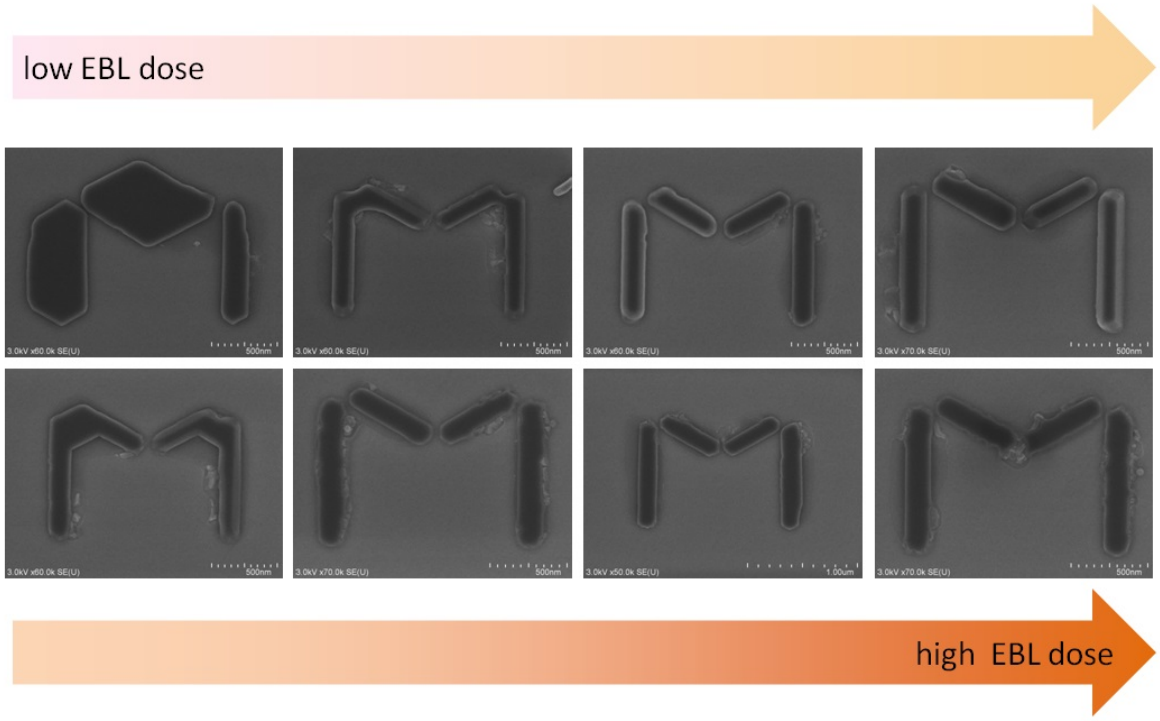

Figure 6: Eight SEM images from nanocluster arrangements grown on an identical, four-cluster pattern which have been structured with different EBL doses. The upper left arrangement was structured with the lowest, the lower right arrangement with the highest dose.

1.2 Contacting of single MnAs nanocluster arrangements

The contacting of single MnAs nanocluster arrangements by a second, aligned electron beam lithography process is a crucial step in the whole experimental procedure. It enables magnetoresistance measurements on single arrangements and thus opens the door for establishing relations between microscopic magnetic effects and the electrical properties. However, this step also comprehends several critical and sophisticated processes, which strongly influence the later performance of the samples in the electrical measurements.

First, one has to identify interesting and suitable nanocluster arrangements on a sample. Since one sample, depending on the used mask patterns, can contain around 40000 or more individual MnAs nanocluster arrangements and the number of possible, practically usable macroscopic contact pad groups is usually not higher than eleven, one has to identify a set of interesting cluster arrangements which fulfill the requirements in terms of quality, model conformity (possibility to describe the structure's properties by a reasonably simple model), ideality of the individual clusters forming the desired kind of arrangement as well as suitable

access for contacting. This is done by SEM imaging of the entire sample surface after the growth process. After roughly identifying the quality of the clusters related to the different mask patterns and EBL doses, the arrangements with the highest suitability for the electrical measurements are identified and characterized by several more detailed SEM images. The coordinates of the individual arrangements are defined by a three-step orientation method. Each of the 8x8 patterns on the sample contains an identical identification marker pattern besides the desired nanocluster structures, which are shown in figure 7. These identification markers consist of 64 unique and well defined marker structures with a pitch of 12 µm, thus this structure enables one to identify a single cluster arrangement's position in a pattern. The arrangement of the 8x8 patterns is labelled in a chess-like scheme using numbers 1 to 8 in one dimension and characters A to H in the other one. Two large global marker structures, defined in a cross-like geometry consisting of a characteristic arrangement of squares, mark the exact position of the entire structure on the substrate. Since the relative positions of cluster patterns, identification markers, 8x8 pattern arrangement and global markers are accurately known, it is sufficient to manually detect the two global markers when contacting a chosen cluster arrangement.

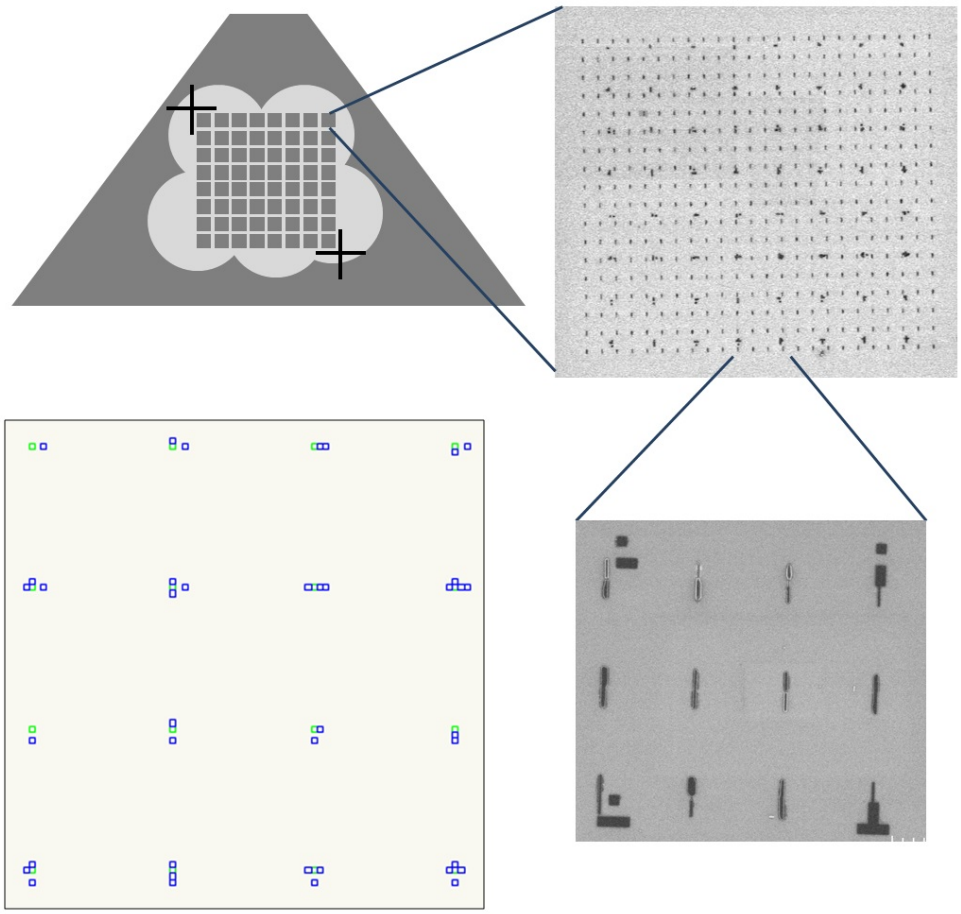

Figure 7: Marker scheme on the MnAs nanocluster samples. The alignment of the second EBL process for the contact structuring is established by locating two large cross markers outside of the nanocluster pattern area, which can be seen on the upper left schematic drawing of a sample. One sample holds 64 cluster patterns in a 8x8 chess board-like structure. Each of the cluster patterns contains the openings for the cluster growth as well as a pattern of small, unique cluster markers which help to identify the exakt position of single clusters and arranegments by SEM imaging. The cluster markers have a pitch of 12 µm.

With the knowledge of the exact position of the cluster arrangements which are to be contacted, a contact structure pattern is designed using a CAD software. This pattern comprises the microscopic contacts to the clusters as well as the connecting circuit paths and the pads for the macroscopic contacting to the sample holder. In addition, microscopic spacer elements between non-merged clusters may be also included to achieve GMR-like devices. A whole contact

structure in CAD design and the corresponding, readily-patterned sample can be seen in figure 8. Since even small deviations in the alignment lead to gaps between the contact structures and the nanoclusters and thus to unusable samples, a very precise positioning of the markers is crucial. The electron beam lithography of the contact structure is followed by a metal evaporation, where the contact layer, consisting of 10 nm titanium, serving as adhesive layer, and 100 nm gold are deposited on the sample.

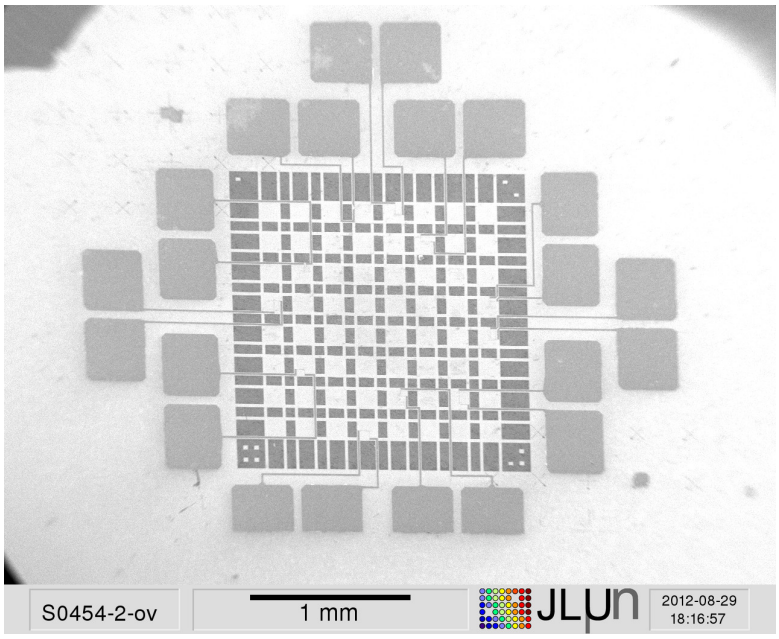

Figure 8: SEM image of a whole MnAs nanocluster sample structure, comprising the 8x8-arranged cluster patterns surrounded by the buffer areas, the contact lanes and the bonding pads.

Before the MR investigation, it has been found that the coverage of the MnAs nanocluster arrangements with a polymer is helpful to ensure that the nanoclusters do not get into contact with water condensating on the cold sample from the laboratory atmosphere after being extracted from the cryostat following the measurements. It has been observed during the synthesis process that the exposure of the samples to water affects the material quality of the clusters, causing the formation of a broken surface morphology and even the detachment of whole clusters. To prevent this, the cluster samples have been covered with a polymer layer based on diluted photoresist. Reference measurements have proven that this coating does not affect the magnetoresistance measurements, however, the structural investigation should be performed in advance to the application of the coating, since the resist layer strongly affects the nanocluster's visibility in an SEM image.

2 Magnetism in solids

Magnetism is a phenomenon basically arising from the interaction of magnetic moments in matter. Electrons have an intrinsic property called the *spin*, which, together with the electron's orbital momentum, causes a magnetic moment. The spin is a quantum-mechanical effect and cannot be fully described by classical approaches. The concept of an exchange energy is used to determine whether electron spin pairs are arranged parallel or antiparallel to each other. It is a basic principle leading to an order of spins, and can be described and understood approximatively as an 'exchange field' arising from the overall average magnetization of a high number of spins, which acts on the magnetic moment of a single spin resulting in its alignment to the field.[Kit91] More basical, one can define the energy of two interacting localized spins as

$$U = -2J\overrightarrow{S}_i \cdot \overrightarrow{S}_j, \tag{1}$$

where $\overrightarrow{S}_{i,j}$ are the spins of the atoms i and j and J is the exchange integral, related to the overlapping of the charge distributions of the involved atoms. This concept of spin coupling is referred to as the "Heisenberg model".[Kas56] The spins stand here for localized magnetic moments. Neither the contribution of orbital angular moments, nor the influence of an external field on the magnetic properties of a solid are taken into account here.

Edmund C. Stoner has developed a model for the description of ferromagnetism in metals like Fe, Co and Ni, which is based on the interaction of band electrons.[Sto39 Iba09] It follows an ansatz which distinguishes between electrons of different spin states:

$$E_\uparrow(\mathbf{k}) = E(\mathbf{k}) - I\frac{n_\uparrow}{N} \tag{2}$$

$$E_\downarrow(\mathbf{k}) = E(\mathbf{k}) - I\frac{n_\downarrow}{N}\ , \tag{3}$$

where $E(\mathbf{k})$ is the electron energy in the band structure, $n_{\uparrow/\downarrow}$ are the numbers of electrons with respective spin state and N is the number of atoms. I describes the energy gain caused by the exchange interaction, which is considered to be approximatively independent from $\mathbf{k}$. Based on this equation pair, one can introduce a ratio R representing the difference in relative occupation of spin states:

$$R = \frac{n_\uparrow - n_\downarrow}{N}. \tag{4}$$

Using Fermi statistics and an approximation of the equation for small R at $T = 0$, one can deduce a criterion for the occurence of band ferromagnetism,

$$I \cdot \widetilde{D}(E_F) > 1. \tag{5}$$

It is referred to as the Stoner criterion, with $\widetilde{D}(E_F)$ as the density of states near the Fermi level, normalized per atom and spin state. It predicts ferromagnetism for the metals Fe, Co and Ni, while in case of the second-row transition metals, the density of states and the spin state ratio are too low.

Magnetism as a collective phenomenon of a macroscopic solid can be described as

$$\overrightarrow{B} = \mu_0(\overrightarrow{H} + \overrightarrow{M}) \ , \tag{6}$$

with $\overrightarrow{B}$ as magnetic flux density, μ_0 as the magnetic permeability constant in vacuum, $\overrightarrow{H}$ as an external magnetic field and $\overrightarrow{M}$ as the magnetization, which is the volume density of magnetic moments in a solid. In case of small external magnetic fields, the magnetization is proportional to the external field:

$$\overrightarrow{M} = \chi \cdot \overrightarrow{H} \ , \tag{7}$$

with χ describing the magnetic susceptibility. It depends, amongst others, on the respective material, the frequency of the external field and the temperature.

There are several different entities of magnetic behavior in solids:

Ferromagnetism This is the most popularly known phenomenon, which in general linguistic usage is mostly and wrongly referred to as "magnetism". In a ferromagnetic material, magnetic moments are aligned in parallel to each other, which results in an overall collective magnetic momentum. The exchange integral J has a positive value, resulting in the system's energy being reduced by the pairing of adjacent spins. Above a certain temperature characterized as *Curie-Temperature* T_C, the thermal energy is large enough to let the momentums become disordered, and the material exhibits a paramagnetic behavior. Ferromagnetic materials expose a spontaneous magnetization below T_C.

Paramagnetism This is a phenomenon where the spins in the solid material are disordered without any present external magnetic field. However, in presence of an external magnetic field, they get aligned to the external field's direction. This results in an increase of the magnetic flux density in the material.

Antiferromagnetism Antiferromagnetism is comparable to ferromagnetism, however, the electron spins get aligned not parallel but antiparallel to each other. This creates an order in the spins of the material, however, results in an overall magnetic moment of zero, since all the magnetic moments have the same value and cancel each other out. The exchange

integral J has a negative value in this case, since the coupling energy between neighbored spins becomes minimized when the spins have an antiparallel orientation.

Ferrimagnetism In this case, the order of the magnetic moments in a material is subdivided into two sublattices, whereas each of the sublattices consists of magnetic momentums of different value and/or orientation. In the majority of cases, this results in an overall magnetization of the material. Antiferromagnetism can be seen as a special case of ferrimagnetism.

Superparamagnetism Superparamagnetism plays a special role amongst these categories, since it is not an effect observable in a bulk material, but in a dense arrangement of small, ferromagnetic single domain particles. Below a certain *blocking temperature*, the single domain particles tend to couple and align their magnetizations and show an overall, ferromagnetism-like magnetization. If the sample temperature exceeds this blocking temperature, the thermal energy is high enough to induce magnetization direction changes in the single domain particles, which is comparable to the macroscopically observed effect of paramagnetism. Note that in this case, the sample temperature is still below the Curie temperature of the particles, thus, ferromagnetism is still observed. However, the energy barrier restricting magnetization reversal scales with the domain volume, what limits this effect to arrangements of small particles in the sub-micron range. Further considerations on the thermally activated magnetization reversal in small particles will be given in chapter 6.1.

2.1 Magnetocrystalline anisotropy

In crystals, the symmetry of the crystal structure can have an influence on the macroscopic magnetic properties of the material. Since the atoms are arranged with a periodic, long range order, the magnetic moments of the crystal sites also follow this order in their coupling behavior. This leads to the effect that the macroscopic magnetization of the material can have preferential, energetically favorable orientations, which are called the easy magnetic axes of the material. Unfavorable directions are referred to as hard magnetic axes.

Early experiments on (0001)-axis oriented MnAs single crystals, also regarding the material's magnetocrystalline anisotropy properties, have been performed and published by De Blois and Rodbell.[De63a De63b] They found a strong uniaxial anisotropy where the c-axis represents a hard magnetic axis. In addition to that, one can observe a six-fold magnetic anisotropy in the (0001) plane.[Har06 El11b] It is caused by the hexagonal NiAs symmetry of the NiAs crystal struc-

ture, which can be seen in figure 1. Since the experiments in this work focus on magnetization rotations performed within the (0001)-plane, one can reduce the problem to the rotational angle of the magnetization in this plane here. An easy quantitative description of the six-fold in-plane anisotropy of this ferromagnetic material can be achieved by the concept of a *magnetocrystalline anisotropy energy* $E_{\mathrm{A,mc}}$ with

$$E_{\mathrm{A,mc}} = -K_{mc} \cdot cos(6\Phi), \tag{8}$$

where K_{mc} is the magnetocrystalline anisotropy constant and Φ the angle relative to the $(\bar{1}10)$ axis in the (0001) plane. A value for the corresponding anisotropy constant has been determined by M.T. Elm by a fit of ferromagnetic resonance spectra, finding $1.62 \cdot 10^5 \frac{J}{m^3}$ in SI units.[El10b] The six-fold symmetry is represented by the factor 6 in the sine factor. This is expressed by six minima with a distance of 60 ° in the energy-angle curve. A schematic drawing of the magnetocrystalline anisotropy energy against the in-plane angle is shown in figure 9. This simple concept also was used in the numerical calculations which are performed to describe the experimental results as will be shown in what follows.

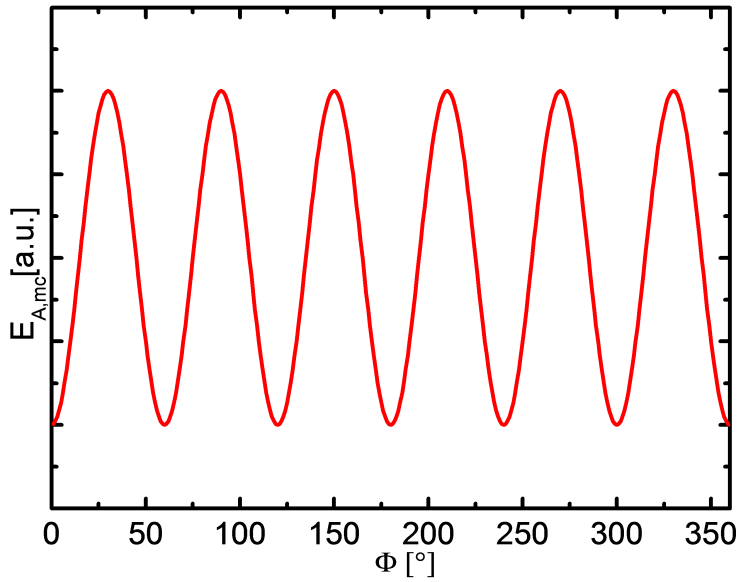

Figure 9: Energy scheme of a six-fold symmetry magnetocrystalline anisotropy in the (0001)-plane, exposing minima with a distance of 60 °. The 0 °-direction is parallel to the $(\bar{1}10)$-direction.

2.2 Shape anisotropy

The shape of a ferromagnetic structure also has an important impact on the formation of preferred magnetization directions.[All94 Kru06] Early considerations on the influence of a specimen's shape on the magnetic anisotropy observed in ferromagnetic resonance absorption experiments have been made by Charles Kittel.[Kit48] He discussed the influence of a demagnetizing field or stray field $B_{str} = \mu_0 H_{str} = -\mu_0 \mathbf{N} \overrightarrow{M}$, defined by the demagnetizing factor $\mathbf{N}$, depending on the shape of the specimen, and the specimen's magnetization $\overrightarrow{M}$. Using this expression, one can calculate the stray energy arising from this effect:[Jag96]

$$E_{str} = -\frac{1}{2} \int_V \mu_0 \overrightarrow{M} H_{str} \mathrm{d}V = V \frac{1}{2} \mu_0 \overrightarrow{M} \mathbf{N} \overrightarrow{M}. \tag{9}$$

In general, the demagnetization factor of the magnetization vector $\overrightarrow{M}$ is written as a tensor $\mathbf{N}$. For an ellipsoidal shape, it has the diagonalized form

$$\mathbf{N} = \begin{pmatrix} N_x & 0 & 0 \\ 0 & N_y & 0 \\ 0 & 0 & N_z \end{pmatrix}, \tag{10}$$

where the diagonal elements of this tensor are N_x, N_y and N_z, defined by the three principal axes of an ellipsoid. They have to fulfill the relation $N_x + N_y + N_z = 1$.[Aha64] This simple approach can be also used to describe more complex objects by determining an 'equivalent ellipsoid'.[Bel06] There are several symmetric shapes which can be described with a diagonalized demagnetization tensor: for a sphere, the matrix elements are $N_x = N_y = N_z = \frac{1}{3}$. An ellipsoid with rotational symmetry around the z-axis is described by $N_x = N_y$ and $N_z = 1 - 2N_x$. An infinitely expanded thin layer in the x-y-plane has $N_z = 1$ while N_x and N_y vanish.

In case of the MnAs nanoclusters, an uniaxial shape anisotropy effect is assumed for elongated nanoclusters. The weak magnetic axis caused by this anisotropy points in the direction of the nanocluster's elongation. This has to be considered as a simplification of the problem, since the complete three dimensional shape of the cluster has an influence on its magnetic behavior. However, the assumption of a uniaxial anisotropy holds well in accordance with the observed magnetization directions in the MFM imaging experiments. It is described by a shape anisotropy energy $E_{\mathrm{A,sh}}$ with

$$E_{\mathrm{A,sh}} = -K_{\mathrm{sh}} \cdot cos(\Phi - \epsilon)^2, \tag{11}$$

where K_{sh} serves as a scalar shape anisotropy constant and ϵ is the direction of the structure's elongation. This approach is comparable to the description of Aharoni.[Aha64] Again, this simplified

term only takes in account magnetizations in the (0001) plane, which is sufficient for the description of the observed planar structures.

2.3 Coupling to external magnetic fields

Magnetic moments interact with external magnetic fields. In the presence of an external field, the magnetic dipole moments have the tendency to align to the external field. With an orientation parallel to the external field, a magnetic moment will be in the state of lowest energy. In a solid, the entity of uniformly aligned magnetic moments can be described as magnetization, which can be understood as a density of magnetic moments per volume. Now, one can observe the effect of an external magnetic field B acting on a volume V with the uniform magnetization M. The energy caused by the interaction between the external field and the magnetic moments in the solid is defined as Zeeman energy E_{Z}. In a simplified approach based on a planar geometry defined by the field and magnetization orientation in a plane, one can write the Zeeman energy as

$$E_{\mathrm{Z}} = -V_{\mathrm{D}} M B \cdot cos(\Phi - \Theta). \tag{12}$$

Here, Φ represents the in-plane orientation of the magnetization of volume V, and Θ stands for the direction of the external field. With increasing relative angle between field and magnetization orientation, the energy caused by this inteaction will rise, increasing the tendency to align the volume's magnetization in the direction of the external field.

2.4 Inter-domain coupling

As described above, the interaction between localized magnetic moments can be described by a Heisenberg coupling term. When a magnetic system has a non-trivial domain structure containing several domains with different magnetizations separated by domain walls, one also has to take into account that this system's total energy contains a certain energy arising from the interaction of neighboring differently magnetized domains. Since the exact morphology and types of the domain walls are not always known in experiment, this energy will be described as a simple, Heisenberg-like coupling energy:

$$E_{\mathrm{cpl}} = -J_{\mathrm{D}} \cdot M^2 \cdot cos(\Phi - \gamma_{\mathrm{D}}) = -J \cdot V_1 V_2 M^2 \cdot cos(\Phi - \gamma_{\mathrm{D}}) \tag{13}$$

This expression is based on the exchange energy shown in equation 1, however, it comprises the coupling between two magnetic domains of the same material, oriented in the planar angles Φ and γ_{D}. This expression will be used in the later chapters for the description of coupling effects between several domains in the models used for the explanations of the observed MR

phenomena. It can be seen as a simple approach to embed domain coupling effects in the used numerical fit functions, where the coupling constant J_{D} will serve as a fitting parameter. For simplification, J_{D} contains the volumes of the two involved domains as a factor.

3 Magnetoresistance effects

Electric transport in solids is influenced by manifold effects of interaction between the charge carriers, the material itself and external influences such as temperature or electromagnetic fields. Thus, the measured overall resistance of a current-carrying system is a combination of several resistance phenomena. When an external magnetic field comes into play and, in addition, when the investigated material itself shows magnetic phenomena, a set of various specific effects related to the magnetic interaction between carriers, material and field have to be taken into account.

In general, magnetoresistance effects are defined as the difference between the resistance of the observed system with an applied external magnetic field to the resistance without field, normalized on the resistance without field:

$$MR(B) = \frac{R(B) - R(0)}{R(0)}, \tag{14}$$

where MR(B) depicts the magnetoresistance ratio and R(B) and R(0) the system's resistance with and without external magnetic field B, respectively. This ratio is often used to compare the various magnetoresistance effects with each other. It also serves as a figure of merit for the comparison of different materials and structural approaches for MR devices - the higher the MR ratio, the better.

The resistance measurements on the MnAs nanocluster arrangements are affected by both, a ferromagnetic conducting material and external magnetic fields. In the following, an overview of the magnetoresistance effects which are crucial for the explanations of the observed phenomena in MnAs cluster arrangements will be given, and their relation to the performed measurements will be discussed.

3.1 Ordinary Magnetoresistance

The transport properties in solids can be theoretically described using the Boltzmann equation, which is an integro-differential expression based on an electron distribution function $f(\overrightarrow{r}, \overrightarrow{k}, t)$ in six-dimensional phase space (momentum and space coordinates). The following considerations are based on the explanations in the textbook "Survey of semiconductor physics" by K.W. Böer (1990). In a steady state approach, the Boltzmann equation presumes that the change of the electron distribution per time, caused by collisions between the electrons, is the sum of the

change in momentum and the change in space:[Boe90]

$$\left(\frac{\partial f(\overrightarrow{r},\overrightarrow{k},t)}{\partial t}\right)_{coll.} = \dot{\overrightarrow{k}}\cdot\Delta_k f + \dot{\overrightarrow{r}}\cdot\Delta_r f, \text{ with} \tag{15}$$

$$\dot{\overrightarrow{k}} = -\frac{e}{\hbar}\overrightarrow{F} \text{ and} \tag{16}$$

$$\dot{\overrightarrow{r}} = \frac{1}{\hbar}\Delta_k E(k) = \overrightarrow{v}. \tag{17}$$

The $\dot{\overrightarrow{k}}$-summand describes the alteration in momentum caused by the external forces $\overrightarrow{F}$ acting on the electrons, while the $\dot{\overrightarrow{r}}$-summand represents the spatial alteration by carrier movement.

The ordinary or transverse magnetoresistance effect, discovered by William Thomson in 1856,[Tho57] can be explained using the equation of motion for quasi-free electrons under the influence of external electric and magnetic fields:

$$m_n\frac{d\overrightarrow{v}}{dt} = e(\overrightarrow{F} + \overrightarrow{v}\times\overrightarrow{B}), \tag{18}$$

with m_n for the electron mass, $\overrightarrow{v}$ as velocity, $\overrightarrow{F}$ as electric field and $\overrightarrow{B}$ as magnetic field. If one reduces the problem by assuming a magnetic field oriented in z-direction, one obtains an x- and y-component, which can be treated together as a complex number. After a multiplication with $e^{i\omega_c t}$, where $\omega_c = \frac{eB_z}{m_n}$ stands for the cyclotron frequency, the expression for the drift velocity

$$v_D = v_0 e^{-i\omega_c t} + \frac{eF}{i\omega_c m_n}(1 - e^{-i\omega_c t}), \text{ with} \tag{19}$$

$$v = v_x + iv_y \text{ and} \tag{20}$$

$$F = F_x + iF_y \tag{21}$$

is found after integration. Since the relaxation times the carriers experience between the collision events are distributed, one can calculate a mean drift velocity $\overline{v_D}$ determined by an average momentum relaxation time τ_m. Based on this consideration, the current densities $j = en\overline{v_D}$ can be expressed. Assuming that $\omega_c\tau_m \ll 1$ is fulfilled, which can be understood as the fact that the carriers undergo a collision event often enough that their trajectory will not describe a full circle, and that the current flows in x-direction ($j_y = 0$), the current density in x-direction reads

$$j_x = en\frac{e}{m_n}\langle\tau_m\rangle F_x\left(1 - \frac{e^2B_z^2}{m_n^2}\frac{\langle\tau_m^3\rangle\langle\tau_m\rangle - \langle\tau_m^2\rangle^2}{\langle\tau_m\rangle^2}\right). \tag{22}$$

The magnetoresistance ratio can be calculated with the resistivity as the reciprocal of the conductivity $\rho = \sigma^{-1}$, the electron mobility $\mu_n = \frac{e\langle\tau_m\rangle}{m_n}$ and the current density $j_x = \sigma F_x(1 - f(B_z^2))$:

$$\frac{\Delta\rho}{\rho} = B_z^2\mu_n\frac{\langle\tau_m^3\rangle\langle\tau_m\rangle - \langle\tau_m^2\rangle^2}{\langle\tau_m\rangle^4}. \tag{23}$$

Here, one can see that the magnetoresistance ratio for a current in x-direction is proportional to the square of the external magnetic field strength, B_z^2, when the magnetic field is oriented in z-direction. The observability of this effect however depends on the scattering effects in the respective material as well as the strength of the external magnetic field, since the assumption was made that the average relaxation time is significantly lower than the reciprocal of the cyclotron frequency.

3.2 Linear Magnetoresistance in Mn-doped and disordered GaAs

In the MR investigations on the MnAs nanoclusters described in the following chapter, one can observe the occurence of a linear MR effect (see chapter 5.3). This effect has previously been observed by Johnson et al. in strongly disordered MnAs-GaAs samples, grown in a self-assembly based MBE process.[Joh10] They discuss their findings using a network model for inhomogeneous conductors, presented by Parish and Littlewood in 2005, originally developed for the explanation of MR effects in silver chalcogenides.[Par05] The network model is based on a two-dimensional grid consisting of heterogeneous, randomized four-terminal elements and is evaluated numerically. For the MnAs-GaAs hybrids, a strong relation between the linear MR effect and the mobility distributions is found. Johnson et al. define a crossover field value H_{CR}, above which the linear MR becomes dominant. With a broad mobility distribution, the linear MR as well as H_{CR} itself are determined by the width of the mobility distribution. With the dominating transport mechanism being percolation, the mobility distribution becomes narrow. Here, the MR and H_{CR} are functions of the average mobility value.

3.3 Spin-valve phenomena

Besides the charge and its orbital momentum, an electron has a spin as an intrinsic property, which has the nature of an angular momentum. Since the electron is understood as a point-like particle with no spatial extension, the spin cannot be described classically as a rotating mass distribution but has to be described quantum-mechanically. As a particle having a charge and an angular momentum arising from both its orbital motion and spin, the electron shows a magnetic dipole moment. This magnetic moment can interact with magnetic fields caused by the conducting material and/or external influences, resulting in an alignment with respect to the field direction and thus a spin polarization of an electron current. This means that an electrical current is coupled to a magnetic current when spin polarization occurs.[Joh85] The spin transport channels, i.e. the areas in the Brillouin zone where the transport of a certain spin polarized current takes place, can have different locations in the reciprocal space. This means that when a spin current with a polarization A gets injected in a material privileging spin polarization B, a

scattering process can occur.[Die94] This spin-dependent scattering is the basic principle of one of the most important magnetoresistance effects, which has been subject of excessive research work, has been the base for whole industry branches and as well has brought its discoverers the Nobel prize in Physics 2007: the Giant Magnetoresistance effect (GMR), discovered by Peter Grünberg and Albert Fert in 1988.[Bai88 Bin89]

The GMR is based on a conductive structure of two ferromagnetic layers separated by a non-ferromagnetic spacer layer. While passing the first magnetic layer, the current undergoes a spin polarization. The spin polarization is conserved when passing through the non-ferromagnetic layer, and entering the second magnetic layer, a spin-dependent scattering process occurs: when the magnetization of the second layer is oriented in the same direction as in the first layer, the spin-polarized electrons can enter the material with a higher probability than in the case that the second layer has a magnetization different from the first one. This effect is reflected in the conductivity of the structure, leading to the term "spin valve" for this setup, since the relative angle of the two magnetizations serves like a valve handle for the transmittance of the structure. An important effect in this context is the spin relaxation, which takes place when the electrons diffuse through the material. It describes the loss of spin polarization and thus is to be minimized in GMR structures to achieve high MR ratios.
A comparable effect was already discovered by Jullière in 1975.[Jul75] Here, the setup consists again of two separated ferromagnetic layers. The difference compared to the GMR arrangement is found in the separator layer, which here is an isolator. The transport of electrons happens in a tunneling process from one side to another, and the tunneling probability increases with a smaller relative angle between the magnetizations of the two layers.

In the TMR and GMR concepts, the most simple arrangements consist of two ferromagnetic layers with a spacer layer is also based on the assumption that the magnetization in the ferromagnetic elements of the structure possess a single domain magnetic structure. This concept is also realizable using planar, SA-MOVPE grown MnAs nanoclusters, when the nanoclusters are small enough and exhibit a simple shape, which is the case for e.g. a round or elongated cluster with a width of about 300 nm and below and a sub-micron length (in case of an elongated structure). With suitably-positioned nanoclusters separated by a sufficiently narrow gap for the insertion of a non-ferromagnetic spacer material, it is thus possible define a GMR-like structure. However, if the morphology of the nanocluster system exceeds the limits of a 'simple' shape, e.g. in the case of two merged nanoclusters, possibly with a relative angle between them like shown in figure 10, the formation of a more complex domain structure is likely, including more than two domains with differently oriented magnetizations.

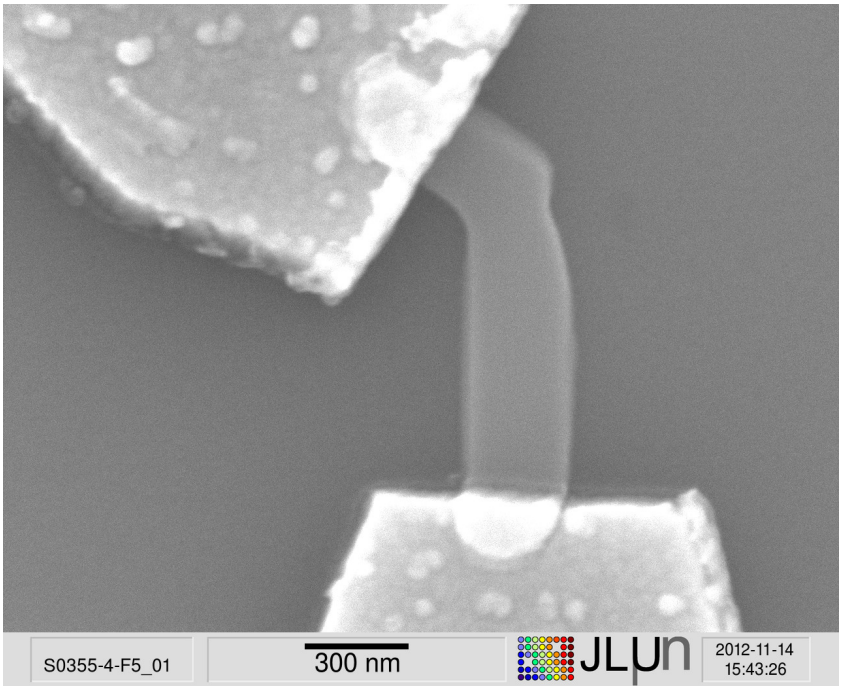

Figure 10: SEM image of a merged two-cluster arrangement. The relative angle between the two elongated clusters is 120 °. Due to the growth parameters, the clusters are strongly merged at their interface.

The case of current passing through such a magnetic structure with several domain walls is different from the case of conventional GMR- and TMR-like device arrangements, since in this case, the functional part of the structure consists of only one material system instead of a heterostructure consisting of ferromagnetic and non-ferromagnetic layers. However, in this case, one can also expect spin-dependent transport caused by scattering events at the domain walls.

Heiliger et al. have investigated the conductivity behavior of ideal domain walls in MnAs[Hei10] by performing ab initio calculations. They found a cosine-like relation between the domain wall conductivity and the relative in-plane angle of the adjacent domains' magnetizations:

$$\sigma \sim cos(\Phi_1 - \Phi_2), \tag{24}$$

with σ for the domain wall conductivity and Φ_x for the magnetization orientation of the two neighboring domains. The magnetoresistance ratio for such an ideal arrangement is determined to about 300% with a spin polarization of 40%. The comparatively high magnetoresistance ratio can be related to the different positions of the spin transport channels in the Brillouin zone.

This causes spin-dependent scattering of charge carriers over the domain wall, which increases with the relative angle between the magnetizations. However, the calculations are based on ideal crystal quality as well as an ideal abrupt domain wall, thus can be seen as an upper limit of achievable magnetoresistance performance. The cosine-like behavior of the conductivity depending on the relative angle of the magnetizations is a central and important information serving the interpretations of the observations made on the MnAs nanocluster arrangements which will be discussed later.

Part II

Investigation of MnAs nanoclusters

4 Magnetic Force Microscopy

Since the revolutionary invention of Scanning Tunneling Microscopy (STM) in 1981, many different techniques based on this principle have been developed, which can all be summarized under the term *Scanning Probe Microscopy* (SPM). They all have in common that a sub-micron scale tip, serving as a probe, is moved over a surface to gain information on its morphology and/or the material properties of the volume below. The tip is mounted on a cantilever consisting of silicon, silicon-oxide or silicon-nitride, which is able to perform mechanical displacement and vibrations. This cantilever can be positioned very precisely in all three spatial dimensions (x and y are the two coordinates parallel to the surface and z is perpendicular to the surface) by changing the bias voltage on piezoelectric crystals on which it is fixed. The cantilever deflection is determined by a laser beam being reflected on its surface and being detected by a CCD sensor. Using this method, even very fine cantilever deflection angles can be detected. Usually, the distance between the probe tip and the surface is in the range of 10 nm and below[Mir04]. In case of STM, one can detect tunnel currents between tip and surface, if both are electrically conductive and a potential difference is applied between them. When performing measurements based on force interactions between the tip and the surface, e.g. atomic force microscopy (AFM), one can detect a cantilever displacement when the tip is approaching the surface. In this case, a feedback control can be introduced to keep the tip-surface distance constant by regulating the z-position on a certain cantilever displacement value. In this case, the information about the surface morphology is given by the adjusted z-position as function of the lateral coordinates. If the z-position of the cantilever is kept constant, the displacement as a function of the lateral coordinates serves as morphology information.

A different approach is possible when the cantilever is brought into a state of oscillation in z-direction, induced by the z-piezo crystal being stimulated by an AC voltage tuned near a resonance frequency of the cantilever. In this case, interactions between the surface and the tip cause a damping of the actual cantilever's oscillation behavior, resulting in a detuning of the resonance frequency and a phase shift. With stronger interaction forces, the disturbance of the cantilever oscillation gets stronger. The frequency offset and the phase shift thus delivers a measure for the strength of the interacting forces.

Since SPM techniques are based on a rather uncomplicated experimental setup, it is possible to realize a sophisticated measurement system yielding nanometer-scale resolutions as a desk-top

tool. The SPM setup used in this work was a commercial NanoScope system manufactured by Digital Instruments, where the measurements are performed in atmosphere and at room temperature. It is also possible to set up a SPM assembly in a vacuum chamber, to install a thermostat to control the sample temperature and even to include the system directly into growth facilities for an in situ analysis, which however brings on the respectively higher apparative complexity. Commercial state-of-the-art systems are able to operate at ultra high vacuum conditions and in a temperature range of around 1.5 K up to 1000 K.
Magnetic force microscopy (MFM) is one of the most widespread methods to analyze micro- and nanoscopic magnetic structures. It is based on the comparatively simple STM setup described above, and most common utilizes the vibrating cantilever operation mode. The significant difference to other SPM techniques is the use of a ferromagnetic tip, which exhibits a permanent magnetization. The magnetization of the tip can be optimized by applying a well-defined external magnetic field to it before performing the measurement. When the tip is approaching a surface of a ferromagnetic sample which possesses a certain magnetic structure, the magnetic dipole of the tip interacts with the magnetic stray fields, which causes a disturbance in the cantilever oscillation. The detected frequency detuning and phase shift as functions of the lateral coordinates x and y serve as a 'map' indicating the stray field intensity above the surface, which allows one to draw conclusions about the magnetic structure of the material near the surface.

In case of the MnAs nanocluster arrangement investigation, MFM plays a key role concerning two central issues:

- **Determination of the magnetic structure** The formation of isolated and well-defined magnetic domains is of major importance for the interpretation of the nanocluster arrangement's behavior. A MFM image of a MnAs nanocluster arrangement can be used to find possible domain wall pinning sites (like strutural features such as constrictions), domain magnetization directions influenced by the cluster's geometry, and possible volumes with a more complex magnetic structure consisting of an ensemble of smaller domains, e.g. at the merging area between two nanoclusters. Gaining knowledge about the domain formation behavior in MnAs nanocluster system enables one to obtain an
- **Additional verification of the formation of a ferromagnetic phase.** MnAs may occur in three different phases depending mainly on the temperature, as described in section 1. Although one expects the formation of the ferromagnetic α-MnAs-phase below 40 °C, possible disruptions in the synthesis process leading to deviations in the material properties and thus the formation of the desired ferromagnetic phase can be additionally excluded by observing the ferromagnetic behavior of the samples in MFM. There are

other methods to confirm and even quantify the ferromagnetic behavior, e.g. ferromagnetic resonance measurements, however, MFM offers a rather simple and fast experimental method to observe a magnetic structure.

Prior to the MFM investigations of the MnAs nanocluster arrangements, the samples were magnetized in an external magnetic field in order to achieve a controlled and comparable initial magnetization state for all samples, since in most cases the MFM was carried out between the growth process and the electrical contact lithography. The applied homogeneous magnetic field was generated in the gap between the poles of an electromagnet where the sample was located. The field direction was parallel to the $[\bar{1}10]$ direction of MnAs and had a flux density of 0.25 T or 0.57 T, depending on the respective laboratory setup. The procedure took place in atmosphere and at room temperature and was carried out with constant maximum flux density for at least one minute. The MFM experiments were carried out exemplarily on several different cluster arrangements after growth or after the contacting process.

4.1 MFM investigations on MnAs nanoclusters after growth

Figure 11 shows a magnetic force microscopy (MFM) image of a single elongated nanocluster. The cluster has a length of approximately 900 nm and a width of approximately 500 nm.

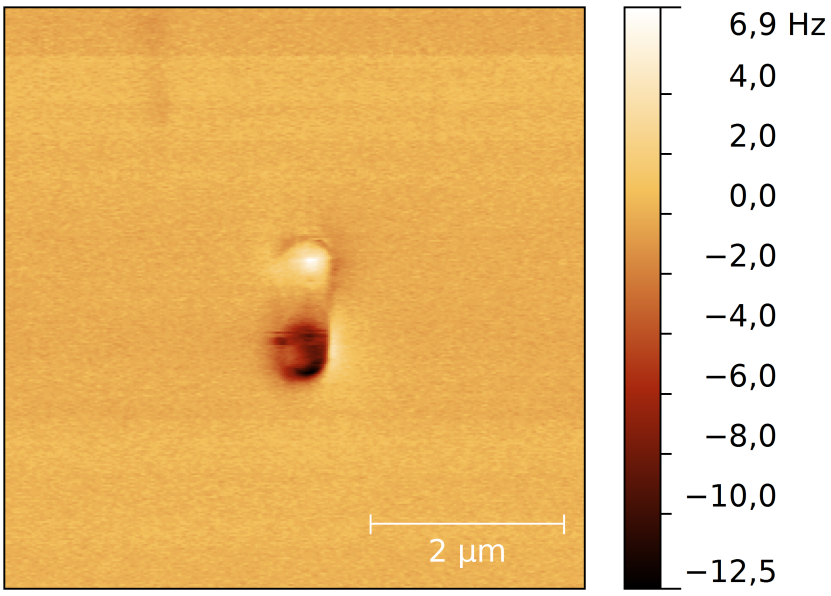

Figure 11: Magnetic force microscopy image of a single, elongated cluster. The formation of a single magnetic domain with a magnetization aligned to the cluster's elongation direction is clearly visible.

The stray fields which are visible in the MFM image imply that one single magnetic domain is formed in the cluster, which is parallel to the $[\bar{1}10]$ direction of the MnAs crystal structure. In this direction, one finds a magnetic easy axis regarding the magnetoctrystalline anisotropy of MnAs as well as the shape anisotropy caused by the elongated form.

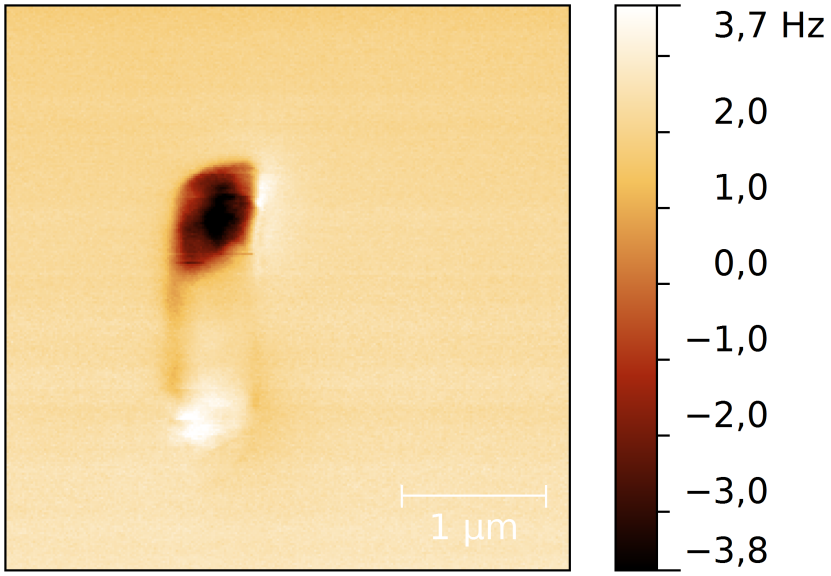

Figure 12: Magnetic force microscopy image of a cluster arrangement consisting of two elongated nanoclusters which are merged at their interfaces.

Figure 12 shows the MFM image of a MnAs nanocluster arrangement consisting of two elongated clusters with a length of 900 nm and a rather large width of approximately 500 nm each. The clusters are merged at their interfaces and form one uniform cluster with a length of approximately 1.8 µm. The MFM image, comparable to the one in figure 11, clearly shows that one single domain is formed in the cluster, whose magnetization direction is oriented along the $[\bar{1}10]$ direction of MnAs, parallel to the cluster's elongation direction.

When the single clusters of an arrangement are not merged, one can observe the formation of single, isolated magnetic domains in each cluster. This can be observed in the arrangement shown in figure 13. It consists of two clearly separated nanoclusters with a length of approximately 900 nm and a width of approximately 500 nm each. The magnetizations are both aligned to the $[\bar{1}10]$ direction of MnAs, which is also the elongation direction of both clusters.
In figure 14, one can see an arrangement of two elongated clusters, both of them with a length of approximately 1 µm and a width of 200 nm. The elongation directions of the clusters are aligned to the [010] (upper cluster) and [100] (lower cluster) direction, respectively, resulting in a relative angle of 60°. The MFM image shows that the clusters form two clearly separated

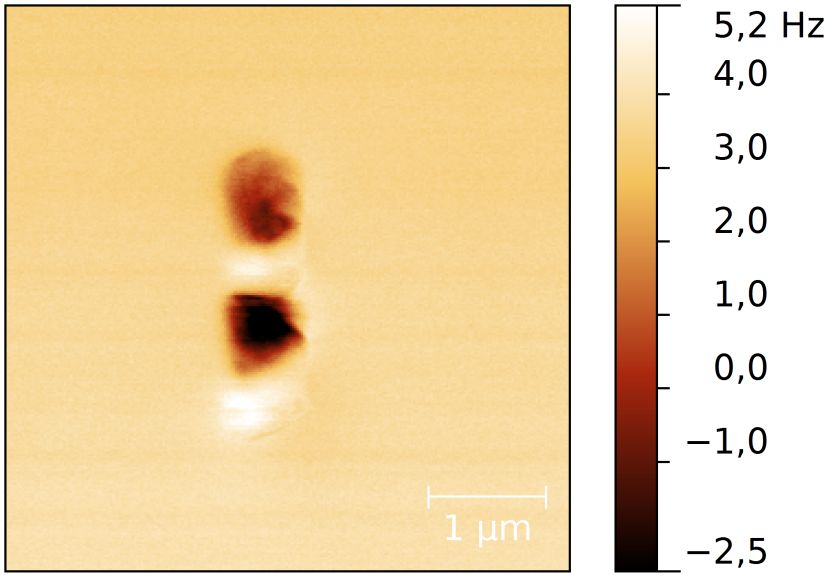

Figure 13: Magnetic force microscopy of an arrangement of two separated, elongated nanoclusters.

magnetic domains, both with the magnetization directions aligned to the respective elongation direction. The [010] and [100] directions also represent easy magnetic axes resulting from the magnetocrystalline anisotropy of MnAs. This observation shows the dominance of the shape anisotropy energy in clusters with comparatively high aspect ratio, since the external field applied in advance to the MFM measurement showed in $[\bar{1}10]$ direction, where one can also find an easy magnetic axis.

The cluster arrangement shown in figure 15 is, comparable to the one in figure 14, composed of two elongated clusters with a length of approximately 1 µm each and a relative angle of 60°. However, they are strongly merged at their ends, resulting in an approximately 500 nm wide agglomeration of MnAs between the clusters in the merging area. As one can see in the MFM image, this agglomeration leads to the formation of multiple magnetic domains with different magnetization orientations. The elongated parts of the two contributing clusters form domains with a magnetization orientation aligned along their elongation directions in the [010] and [100] direction, respectively. In the agglomeration area, two magnetic domains are formed with magnetization orientations parallel to the $[\bar{1}10]$ direction and antiparallel to each other. The more complex micromagnetic structure in this case leads to the assumption that MnAs nanocluster structures with a low lateral aspect ratio and lateral extensions of 500 nm and more tend to form multiple domains with different magnetization orientations.

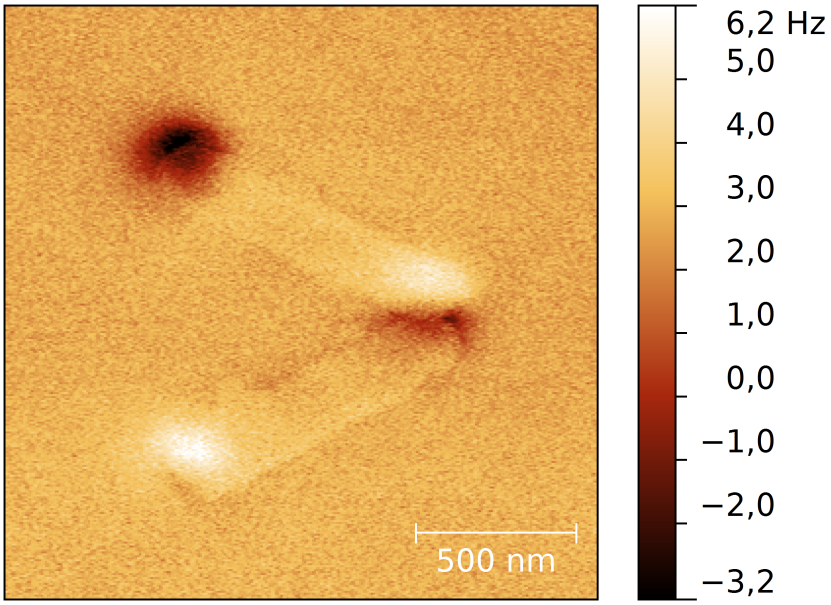

Figure 14: Magnetic force microscopy of an arrangement of two elongated nanoclusters with a relative angle of 60°. The upper cluster is parallel to the [010] direction of Mnas, the lower cluster is parallel to the [100] direction.

4.2 MFM investigations on contacted MnAs nanoclusters

The contact structures which are applied on the nanocluster arrangements after growth have a thickness of around 110 nm, which is significantly more than the MnAs nanocluster thickness of less than 100 nm. This complicates the MFM imaging on the nanoclusters, since the interaction between the magnetic stray fields of the clusters and the magnetized probe tip depends on the distance between surface and tip. The height of the contact structure reduces the exchange integral for the interaction between the stray fields of the MnAs clusters and the magnetized tip, disturbing the stray field detection.

However, it is experimentally possible to observe the magnetization of contacted clusters, when the domains are large enough to yield sufficiently strong stray fields to achieve a detectable interaction even above the contact layers. Figure 16 shows an arrangement of two merged elongated nanoclusters with a length of 900 nm and a width of 400 nm each. One can observe the formation of a single magnetic domain in the $[\bar{1}10]$ direction and parallel to the cluster's elongation direction.

The MFM imaging experiments confirm that the grown clusters consist of a ferromagnetic material, which is with a high probability the expected α-phase of MnAs. In every MFM image, an interaction between the stray fields caused by the cluster's magnetic domains and the magnetic probe can be observed. Furthermore, the orientation of the cluster's magnetizations is

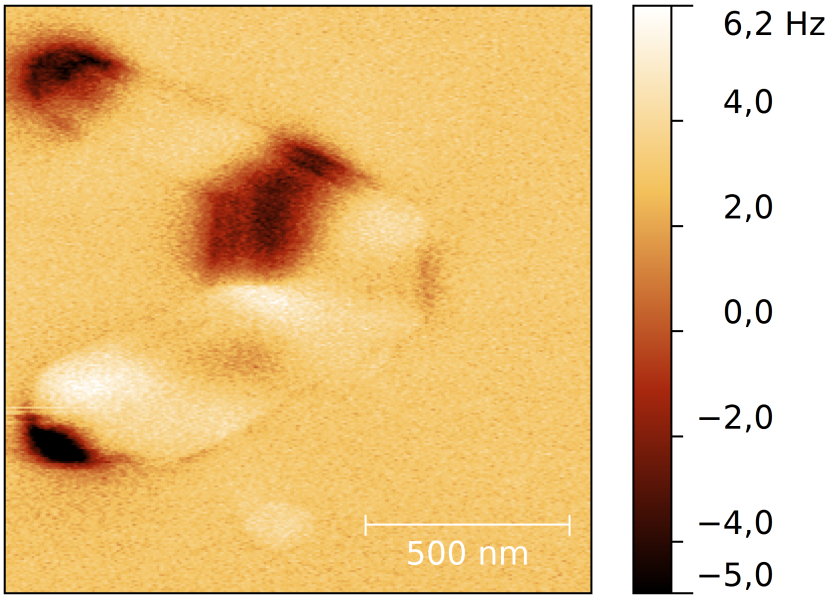

Figure 15: Magnetic force microscopy of an arrangement of two elongated nanoclusters with a relative angle of 60°, which are merged at their interfaces. During growth, MnAs has accumulated in the pointed angle between the clusters, which forms a bulk area with a width of around 500 nm.

strongly influenced by their shape. Although there is an external magnetic field, oriented in the $[\bar{1}10]$ direction of MnAs, applied to the sample in advance to the imaging procedure, one can observe that the magnetization of elongated clusters is preferably aligned to the respective elongation direction of the cluster, even if this direction is different from the external magnetic field direction. This denotes the dominance of the magnetic shape anisotropy.

In case of a cluster shape with a lower lateral aspect ratio, one can observe the formation of a multiple domain structure. Figure 15 shows that the bulk-like structure promotes the establishment of two counterwise aligned magnetic domains, whereas the left domain in the bulk area is also aligned to the poles of the adjacent elongated cluster parts. This information is of greater importance in particular for the interpretation of the investigations on merged cluster systems.

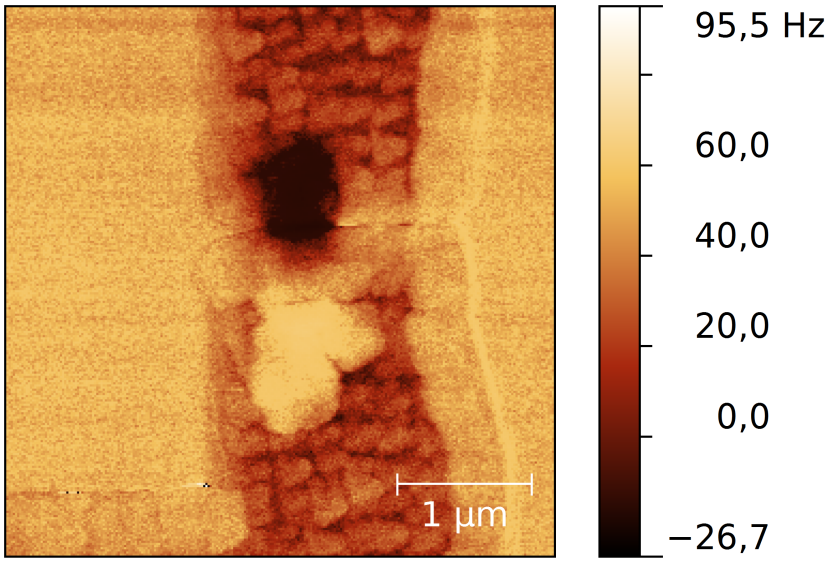

Figure 16: Magnetic force microscopy of an arrangement of two elongated nanoclusters with a length of 900 nm each and contacted by a structure consisting of 10 nm Ti and 100 nm Au.

5 Magnetoresistance measurements on MnAs nanoclusters

The purpose of the present thesis is to investigate the possibilities of applying MnAs nanoclusters and nanocluster arrangements as building blocks for novel, planar magnetoelectronic device structures. To get insight into the electrical transport properties of the clusters, they have been equipped with electric contacts, allowing one to connect them to laboratory equipment for the conduction of magnetotransport experiments. A high variety of measurements on many different sample structures and under varying several external parameters like the magnetic field and the sample temperature has been performed.

The experimental setup in which these measurements were carried out is based on a commercial

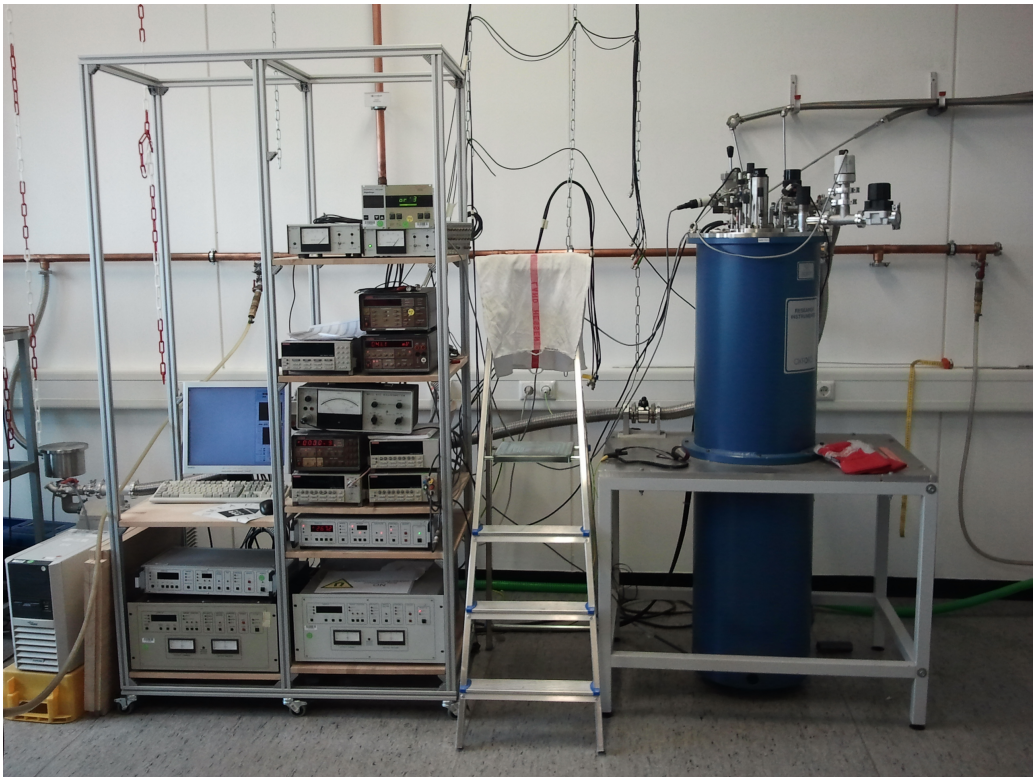

Figure 17: The transport measurement system, including the cryostat (blue cylinder) comprising the helium bath and superconducting magnet coil and a rack containing the whole automatized measurement device setup.

Oxford VTI-cryostat embedded in a superconducting magnet system. It allows to adjust the sample temperature between 1.6 and 280 K, while external magnetic fields of up to 10 T can be applied with a defined orientation with respect to the sample. Usually, the samples are mounted on a sample holder which allows one to adjust and vary the sample orientation about two axes which then remain fixed during the actual measurement procedure in the cryostat. The sample

holder is equipped with a special temperature sensor showing a low magnetoresistance influence. The sample cooling is achieved by a flow of liquid helium into the evacuated sample chamber, regulated by a needle valve. Without helium flow, the vacuum in the sample chamber usually reaches values in the upper mPa range. For the adjustment and regulation of the temperature, the helium flow is set to a constant level yielding a chamber pressure of 1 kPa, while the cooling counteracts to a PID-controlled heater coil connected to the sample chamber. The heating power is controlled by an Oxford ITC-4 temperature control, which is connected to a separate temperature sensor located inside the sample chamber. This setup allows one a sufficiently precisely control of the measurement temperature, which usually shows a deviation below 0.1 K. The magnetic field is generated by a superconducting coil bearing currents of up to 120 A and located in a liquid helium bath. The power and control for the magnetic fields is provided by an Oxford PS-120-10 magnet power source, which allows one to conduct measurements at constant fields with a step-wise change as well as in sweeping fields with a well-defined sweeping rate. Usually, the transport measurements are performed at a constant current, which is provided and controlled by a Keithley 220 power current source. For achieving a higher precision in the resistance measurements, this current is measured by a separate Keithley 6485 picoamperemeter in serial connection. The voltage drop over the sample is measured by a Keithley 2182 nanovoltmeter. The connection between the sample contacts and the measuring equipment is performed by a Keithley 7001 switch system with a 7065 Hall card, which provides a high variety of possible measuring configurations without the manual change of any plug-in connections.

The whole measurement setup is centrally controlled by a personal computer over GPIB and serial bus systems. By using the custom-made measurement software *Caesar 2*, it is possible to conduct fully automatized transport measurement sequences with a free choice of measurement conditions. An automatically generated measurement protocol contains a set of values characterizing each performed measurement step, recording the applied current, measured voltage, sample temperature, applied external magnetic field and the time at which the measurement took place as well as the predefined target parameters. With this set of information, it is possible to observe relations between the transport properties of the sample and the input parameters field, temperature and time.

There are several different measurement modes which were applied on the MnAs nanoclusters. They are based on the acquisition of a series of predefined measurement setpoints at certain temperatures and external magnetic fields. The *magnetic field dependence* measurement is usually carried out at a constant temperature, with the magnetic field varying from setpoint to setpoint. For the *temperature dependence* measurement, the external magnetic field is held at a constant value (mostly zero), and the temperature is changed from setpoint to setpoint.

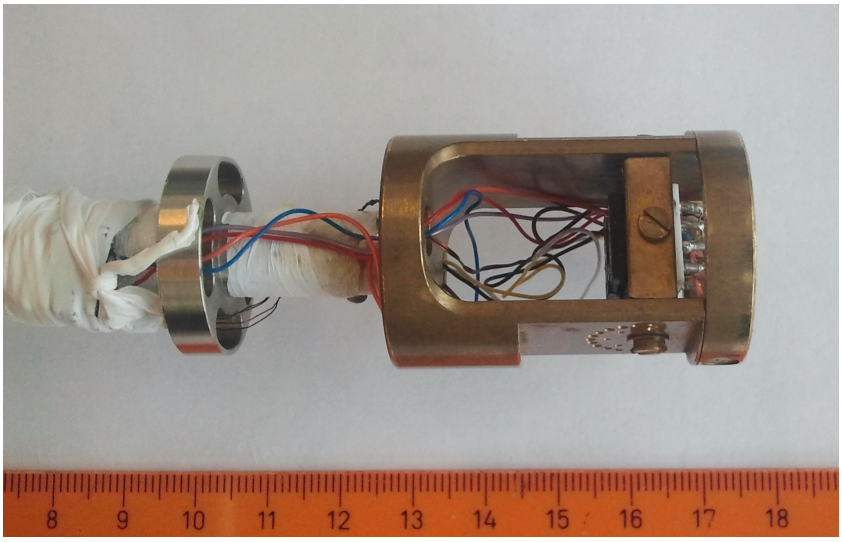

Figure 18: The lowest part of the sample holder, which is located on the level of the superconducting coil during the measurement. The sample is positioned on the movable socket by using an eight-pin plug holder. Below the socket, a resistive temperature sensor with low magnetic field sensitivity provides information on the sample temperature during the measurements. The socket plate can be panned to the vertical sample holder axis in steps of 15 °, while the socket can be rotated in this plane by 90 °.

For the *time dependence* measurements, the magnetic field dependence measuring scheme is applied with the use of constant field sequences. In this case, the repetition rate is determined by the adjustable waiting times between and during the measurements as well as the times the measurement itself takes to be performed.

5.1 Current-voltage characteristics

A contacted MnAs nanocluster arrangement includes several different interfaces: two interfaces between gold bond wire and bondpad as well as two interfaces between contact structure and MnAs cluster. To determine that the interfaces show an ohmic behavior, a current-voltage characteristics measurement has been performed on several samples. In every case, the characteristic yields a straight line, confirming the ohmic behavior of the whole contact chain. Figure 19 shows the measurement for sample S0355(3)-B7, exemplarily. The voltage has been varied in a range of ±10 mV, resulting in a current of up to 50 nA.

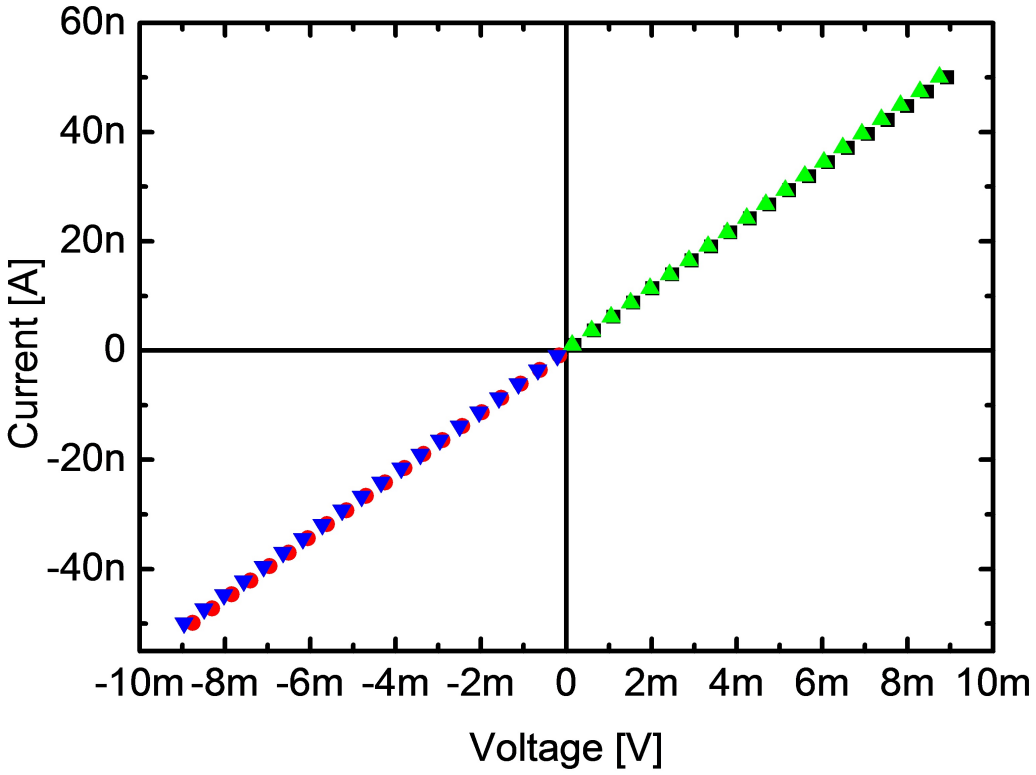

Figure 19: Current-voltage characteristics measurement on sample S0355(3)-B7. The two curves result from two different measurement configurations of the four-point-contacting with two bond contacts on each of the two bondpads.

5.2 Magnetoresistance jumps

When a current is passing through a system containing two or more magnetic domains and thus one or more magnetic domain walls, the relative angle of the adjacent domain magnetizations of the domain wall influences its conductivity with a cosine-like behavior. As described above, the magnetoresistance in MnAs nanocluster-based systems has a theoretically determined upper limit of about 300%[Hei10], which depicts the possible impact of magnetoresistance effects based on the domain structure. When the relative angle of the adjacent magnetizations of a domain wall changes abruptly, one can expect an abrupt change in the resistance of the system. These magnetization changes can be related to external influences such as the external magnetic field or the temperature and are also influenced by the magnetic anisotropy effect, which will be explained in detail when discussing the respective measurements.

One of the first magnetoresistance measurements on the sample S0308(1)-B8, shown in figure 20, illustrates the possibilities for the observation of discrete magnetoresistance phenomena in MnAs nanoclusters. The sample, which can be seen in figure 21, consists of two elongated

nanoclusters with a length of 900 nm each and a relative angle of 120 ° merged to a round cluster between them, resulting in structure widths of about 200 nm and 300 nm in the merging area around the intermediate cluster. Based on earlier considerations about shape anisotropy effects and MFM investigations on comparable systems, one can expect a rather complicated domain structure here, which leads to the formation of several small domains in the merging area. The numerous observed jump events can be related to thermally activated magnetization changes in small domains in the merging area as well as the changing external magnetic field. The field was oriented perpendicular to the $(\bar{1}10)$ direction (parallel to the vertical elongated cluster in the image) in the sample plane between -10 T and 10 T and in case of one measurement cycle between -5 T and 5 T. However, in case of this sample, the rather random jump characteristics inhibits a further explanation of the magnetization change events leading to the jumps. The fact that the jumps occur at several different fields yielding numerous different, non-reproducable resistance values, leads to the conclusion that a highly disordered magnetic domain structure is present at least in the merging area around the round structure between the two elongated clusters. In addition, the influence of thermally activated effects can be considered as important at 280 K, since in other samples, thermal effects on MnAs were observed even at significantly lower temperature ranges between 65 K and 165 K.

This series of interesting measurements shows that discrete MR jumps can be observed in MnAs even at room temperature. For a better understanding of the effects comprising the influence of the external magnetic field as well as that of the thermal energy, a number of investigations has been performed on several different nanocluster arrangements, allowing one to distinguish between the effects of the external parameters on the magnetoresistance behavior.

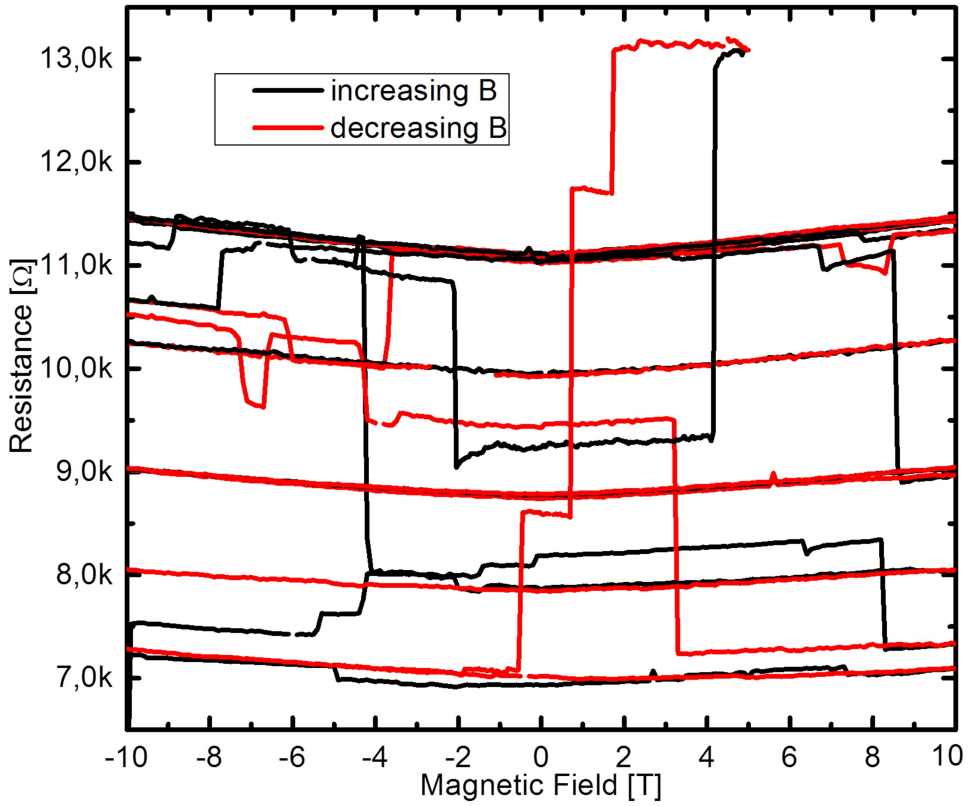

Figure 20: Stack plot of magnetoresistance measurements, performed under the influence of a varying external magnetic field at 280K on the MnAs nanocluster sample S0308(1)-B8. Numerous discrete changes in the resistance can be observed.

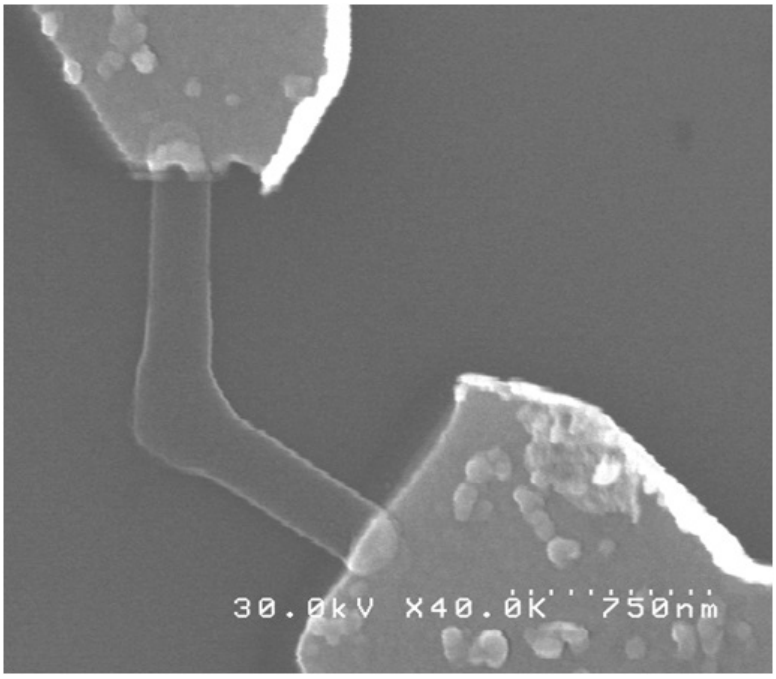

Figure 21: MnAs nanocluster sample S0308(1)-B8, consisting of two elongated nanoclusters merged with a round cluster between them, forming a large, merged three-cluster system.

The images shown in figure 23 show two MR measurements on sample S0355(3)-B7, shown in figure 22.

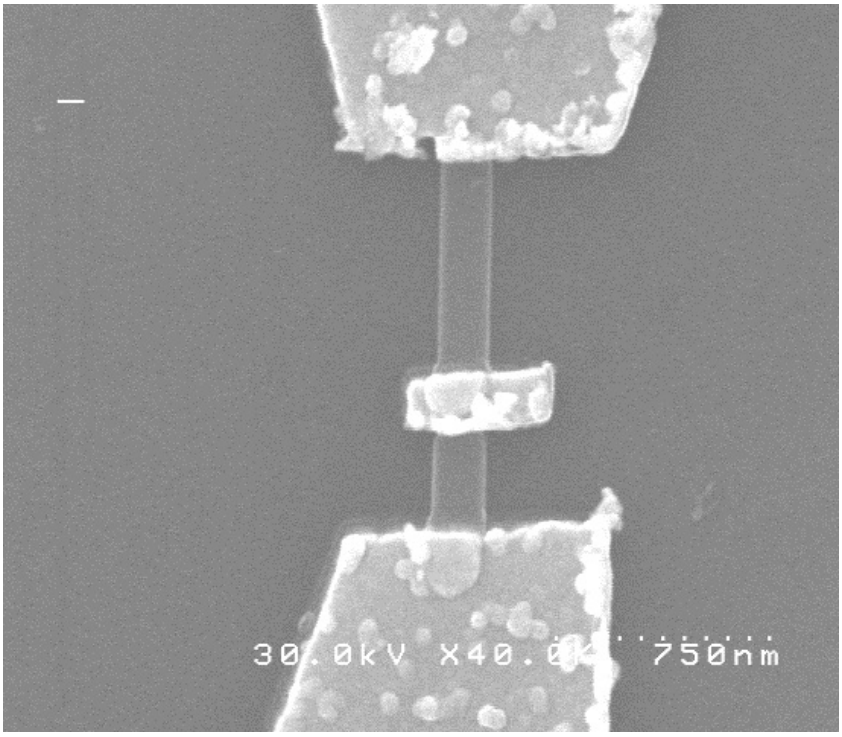

Figure 22: MnAs nanocluster sample S0355(3)-B7-1, consisting of two clearly separated, elongated nanoclusters connected by a metal (Au) spacer.

This nanocluster arrangement consists of two elongated clusters which are both oriented parallel to the $(\bar{1}10)$-axis of MnAs. They have a length of 1 µm and 750 nm, respectively, and a width of 150 nm for both clusters. At their merging point, the clusters are connected by a metal spacer layer, which consists of 100 nm gold grown on 10 nm titanium as adhesive layer, both deposited by a thermal evaporation process. The concept of this magnetoelectronic structure is comparable to a GMR setup, where two magnetic layers are separated by a nonmagnetic conductive material. The MR effect in GMR devices originates from the spin conservation of charge carriers, which are injected from the first ferromagnetic layer into the nonmagnetic material, experiencing spin-dependent scattering at the interface between the nonmagnetic and the second ferromagnetic layer. For a parallel configuration of the magnetizations of the two ferromagnetic regimes, one expects less spin-dependent scattering compared to an antiparallel configuration, resulting in a lower resistance. Such a GMR-like effect should also occur in case of the MnAs nanocluster arrangement shown in figure 22, just in the geometry arranged in the sample plane, although different from the layered arrangement of the classical GMR geometry.

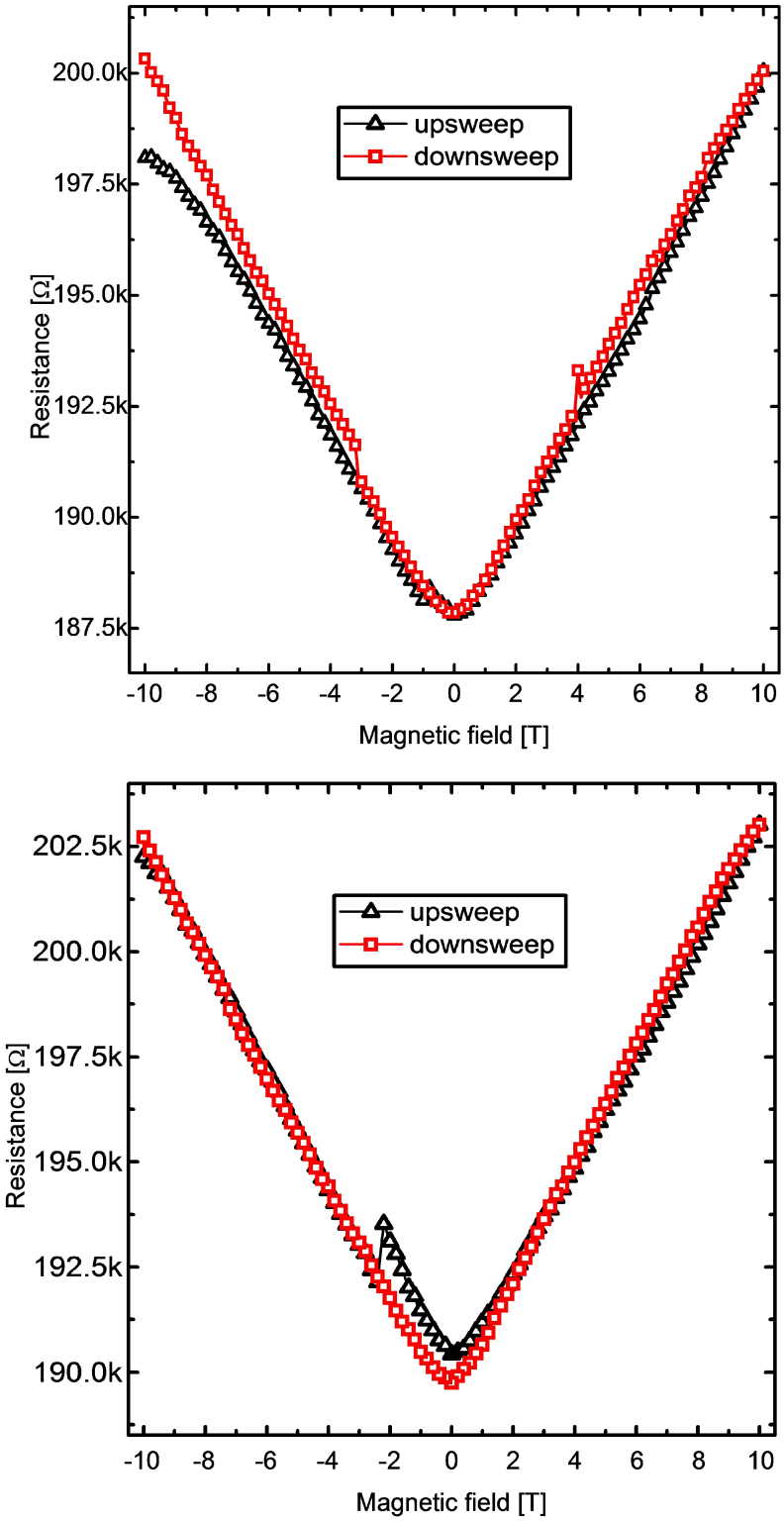

Figure 23: Raw MR measurements on sample S0355(3)-B7. The external magnetic field was varied between -10 T and 10 T in parallel or perpendicular configuration relative to the $(\bar{1}10)$ direction in sample plane.

The measurements on sample S0355(3)-B7 (figure 23) show a strong linear MR effect resulting from shunting currents through the matrix below the nanoclusters, as described in chapter 3.2. Both measurements have been performed starting from an external magnetic field of -10 T, rising to +10 T and sweeping back to -10 T, all with an increment of 0.1 T between the measurement steps. In the measurement graph for the parallel configuration, one can observe a slightly lower resistance at the starting point of the upsweep branch, which was performed at the beginning of the measurement. This effect is caused by the thermal influence on the system's ohmic resistance while the sample temperature was not yet adjusted to the equilibrium value at the beginning of the measurement sequence.
In contrast to the continuous and smooth background characteristics caused by the two mentioned effects, one can identify several discrete changes of the resistance which can be related to magnetization jumps. To achieve a better visibility of those resistance jumps, the background has been subtracted for both configurations. The magnetoresistance graphs corrected in this manner can be seen in figure 25 for the parallel configuration and figure 24 for the perpendicular configuration of cluster symmetry axis and external magnetic field direction.

After subtracting the background, the magnetoresistance measurement in figure 24 shows one large resistance jump on the first, rising field branch of the measurement. The jump has a relative height of 1.38 $k\Omega$, which yields a MR ratio of around 7.2 ‰ when normalized to the zero-field resistance of the upsweep branch of 190.43 $k\Omega$. This is comparatively small, however, considering the observed linear background MR, one can assume that a significant part of the electrical current is flowing through a shunting path in the Mn-doped GaAs matrix beyond the nanoclusters. Thus, one finds that only a part of the measured current is actually passing the nanocluster arrangement. This allows one to assume that the actual MR effect in the arrangement is higher, since the measurement of the zero-field resistance comprises the transport through both, cluster arrangement and matrix, because a subtraction of the linear MR background is only possible for the magnetic-field dependent contribution. The observed MR jump extends over three measurement points, starting at -2.2 T and ending at -2.0 T. Afterwards, the high resistance value decreases slowly until it meets again with the baseline at around +4 T. On the measurement branch back from +10 T to -10 T, no jump-like phenomenon can be observed, and the resistance stays on a comparatively smooth level.

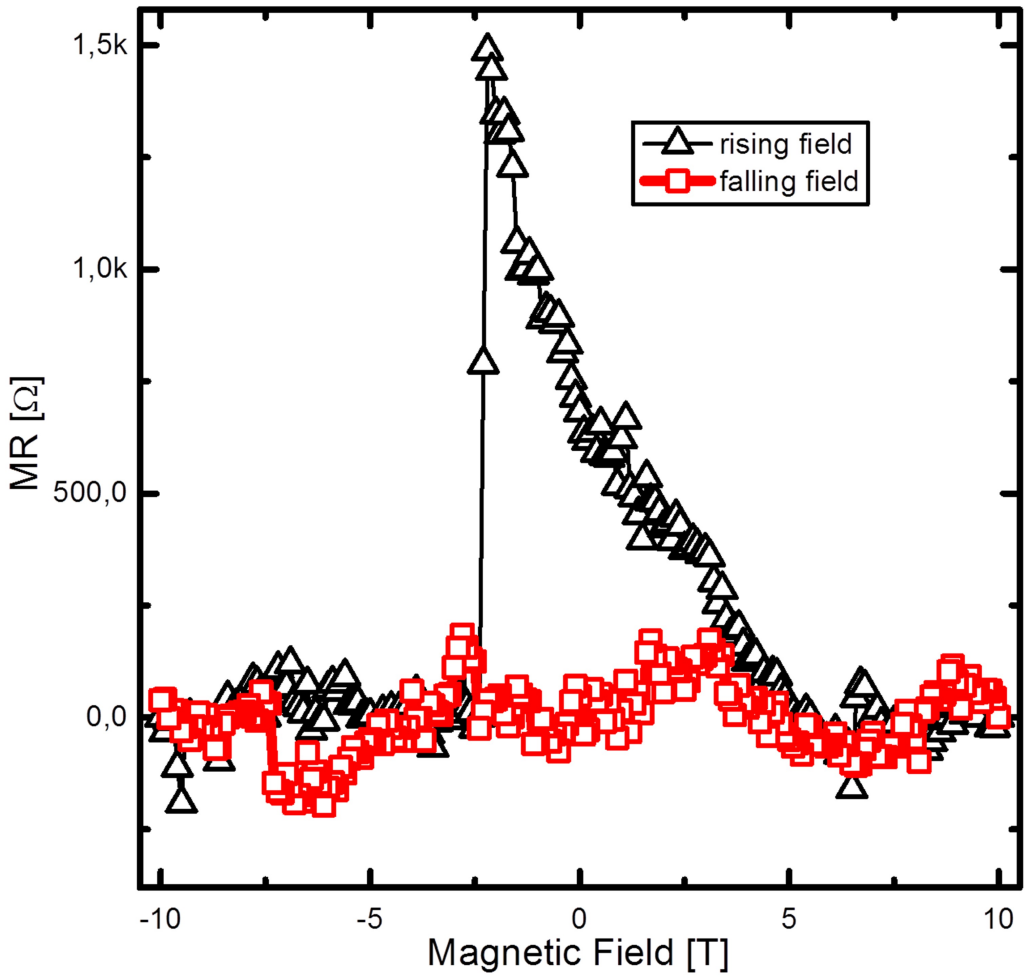

Figure 24: MR measurement with the external field perpendicular to S0355(3)-B7 and with subtracted background function. A MR jump around -2.1 T is clearly visible.

In case of the parallel orientation of the external magnetic field and the nanocluster arrangement, one can observe two jump features, one on each branch of the measurement. The first jump on the upsweep branch extends from -1 T to -0.8 T, afterwards it decays slowly with rising external field until it reaches the baseline at around +1 T. On the downsweep branch, a jump occurs at -3.1 T and ends at -3.2 T, afterwards the resistance value decreases again slowly down to the baseline value at around 7 T. For both jumps, one achieves a MR ratio of around 2.7 ‰, which is again comparatively low while the actual MR performance of the arrangement can be suspected higher due to shunting currents below the nanoclusters.

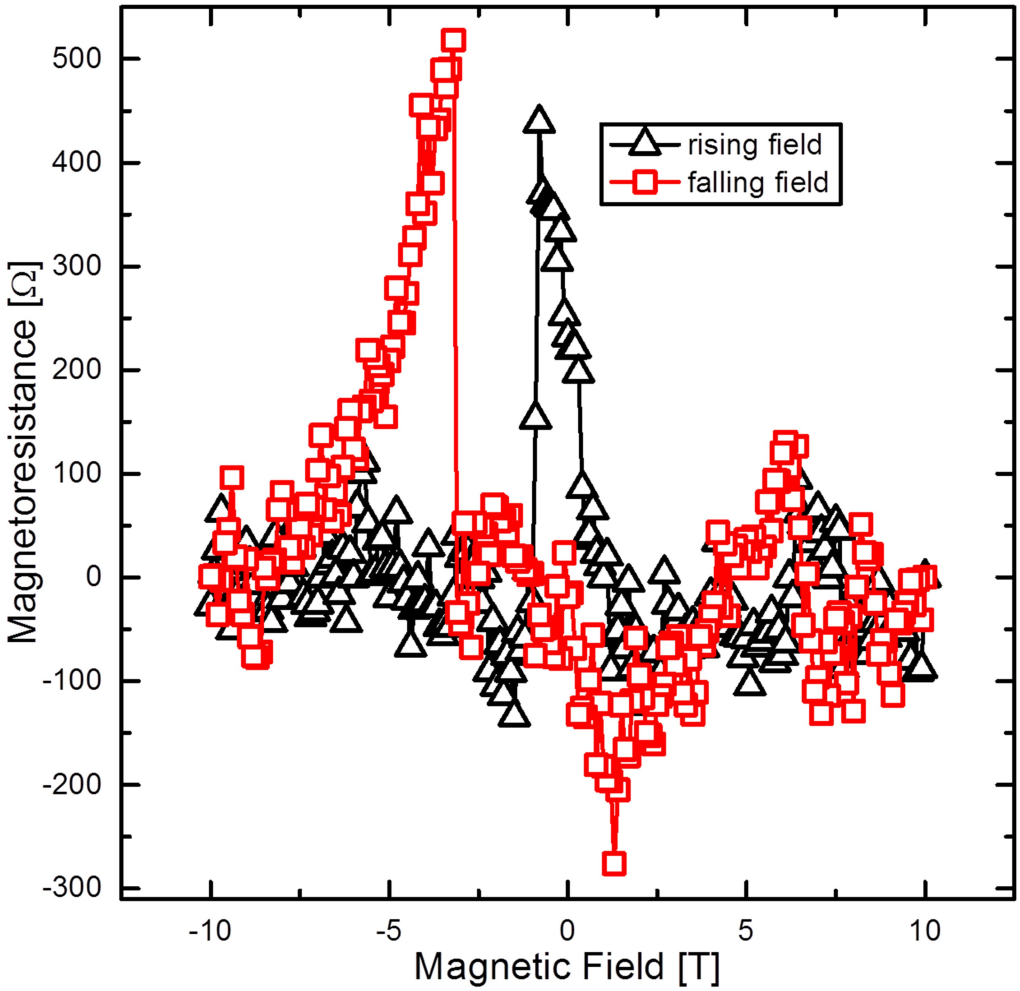

Figure 25: MR measurement with the external field parallel to S0355(3)-B7 and with subtracted background function. MR jumps around -0.9 T and -3.1 T are clearly visible.

An explanation for these phenomena and their characteristics can be found by considering the free energy of the nanoclusters, which is influenced by the external magnetic field as well as by the magnetic anisotropy effects arising from the crystal structure of MnAs, the magnetocrystalline anisotropy, and the morphology of the respective nanoclusters, the shape anisotropy. Also, coupling effects between the clusters play a role. The interplay of those effects generates a manifold of more or less favorable orientations for the cluster's magnetizations. Since the clusters have only weak magnetic axes in the (0001) or sample plane and a hard magnetic axis perpendicular to this plane, one can assume that their magnetizations are oriented in the sample plane. This reduces the evaluation of the magnetization's energetical manifold to a one-dimensional problem. The free energy of a nanocluster can then be plotted as a function of the rotational in-plane angle of the magnetization. This graph is referred to as an energy landscape, exposing a variety of minima which represent favorable positions of the magnetizations.

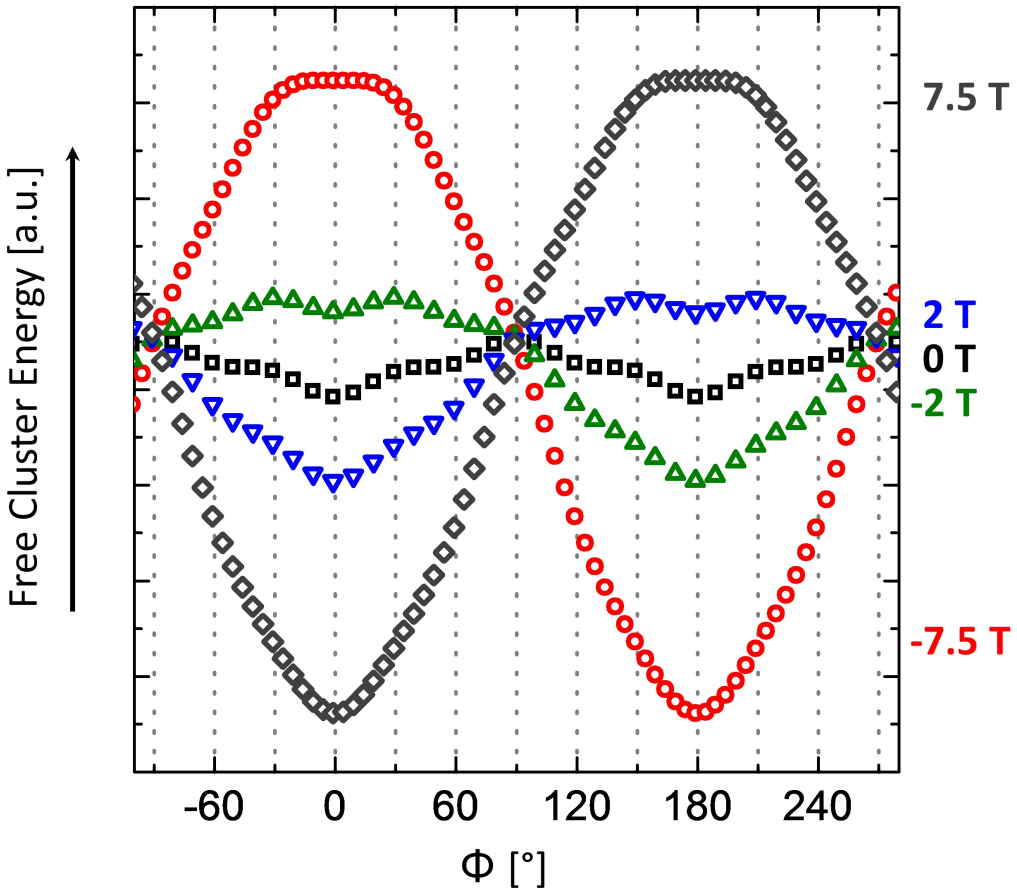

Figure 26: Energy landscape for an elongated nanocluster comparable to the clusters in the investigated sample S0355(3)-B7 and exposed to external magnetic fields with different strengths and parallel to the elongation direction of the cluster.

Figure 26 shows the energy landscape for one cluster in the investigated arrangement under the influence of different external magnetic fields. In the absence of a field, the energy landscape is dominated by the magnetocrystalline anisotropy with its six-fold symmetry, showing six minima with relative angles of about 60 ° and slightly shifted by the shape anisotropy caused by the clusters elongation. The two significantly deeper and identical minima at 0 ° and 180 ° mark magnetization orientations parallel to the clusters elongation direction. Here, a superposition of magnetocrystalline and shape minima occurs, thus one achieves an energetically favorable orientation. If one switches on an external magnetic field parallel to the clusters elongation direction, the influence of the Zeeman energy becomes visible in form of a sine-like profile establishing in the energy landscape. At field values of 2 T, one can already observe a deep valley establishing in the direction of the applied field, while several other minima are still

visible. At a higher field value of 7.5 T, all minima vanish except the one that is induced by the external field. Figure 27 shows a comparable energy landscape for the case with the external magnetic field oriented perpendicular to the cluster's elongation direction and in sample plane.

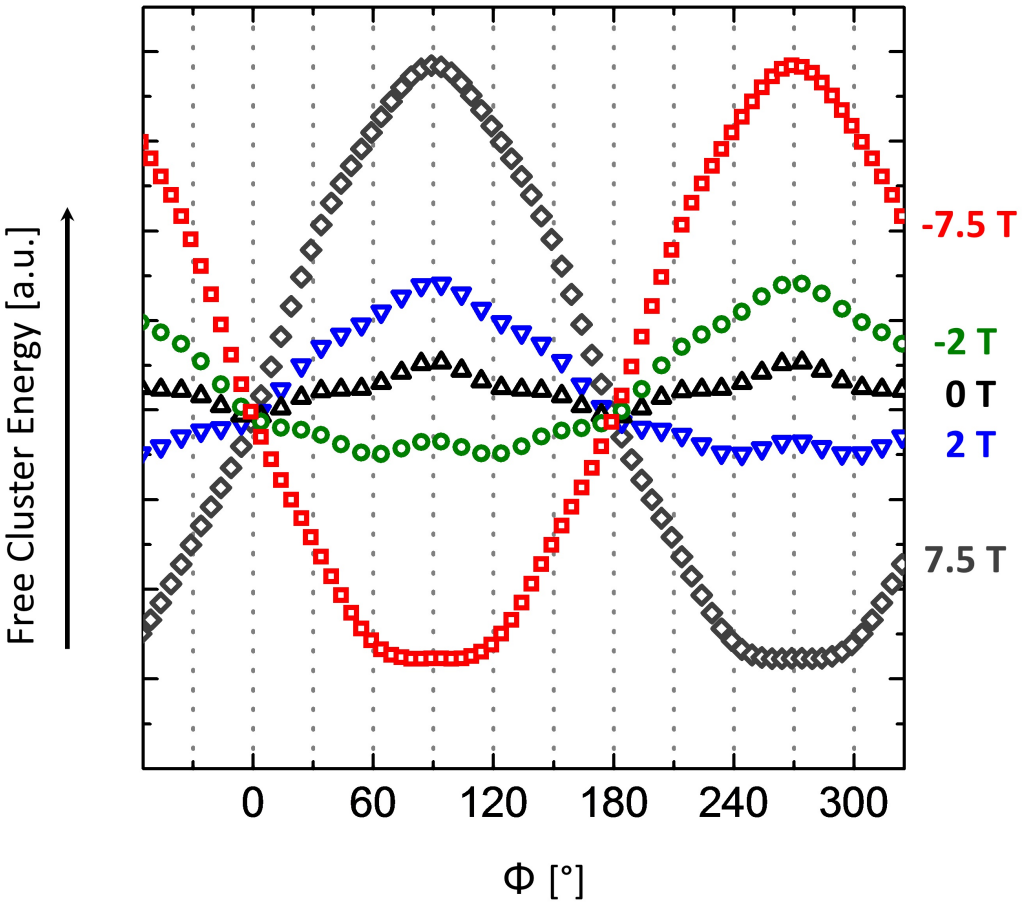

Figure 27: Energy landscape for an elongated nanocluster comparable to the clusters in the investigated sample S0355(3)-B7 and exposed to external magnetic fields with different strengths and perpendicular to the elongation direction of the cluster.

These considerations help one to interpret the magnetoresistance jumps observed in the measurements. Figure 28 shows the correlation between the external magnetic field and the magnetizations in the nanocluster arrangement, leading to the magnetoresistance characteristics shown in figure 24 and being influenced by the different energy landscapes at different fields like shown in figure 27. Starting at waypoint I, the external magnetic field is at -10 T and both cluster magnetizations are aligned along the external field. Thus, the relative angle of the magnetizations results in a low magnetoresistance of the cluster interface. With decreasing external field (waypoint II), the magnetizations rotate into the direction of the cluster elongation.

This is caused by minima of the shape anisotropy energy in the energy landscape, which become the dominant minima with decreasing field. Since a jump is observed in the MR measurement at that point, it is concluded that the magnetizations turn into opposite orientations. From waypoint III, where the field polarity is changed and the field increases towards 10 T, the magnetizations turn out of the shape anisotropy minima continuously, which causes the MR to decrease slowly back to the baseline. Here, the cluster magnetizations are again aligned to the external field, which is also the case at waypoint IV. When decreasing again towards waypoint V, no jump is seen in the MR measurement. This is correlated to the cluster magnetizations turning back into the elongation directions again somewhat comparable to waypoint II, however, here they turn into a parallel aligned state during the field reduction and reversal, yielding no change in the relative angle and thus in the MR.

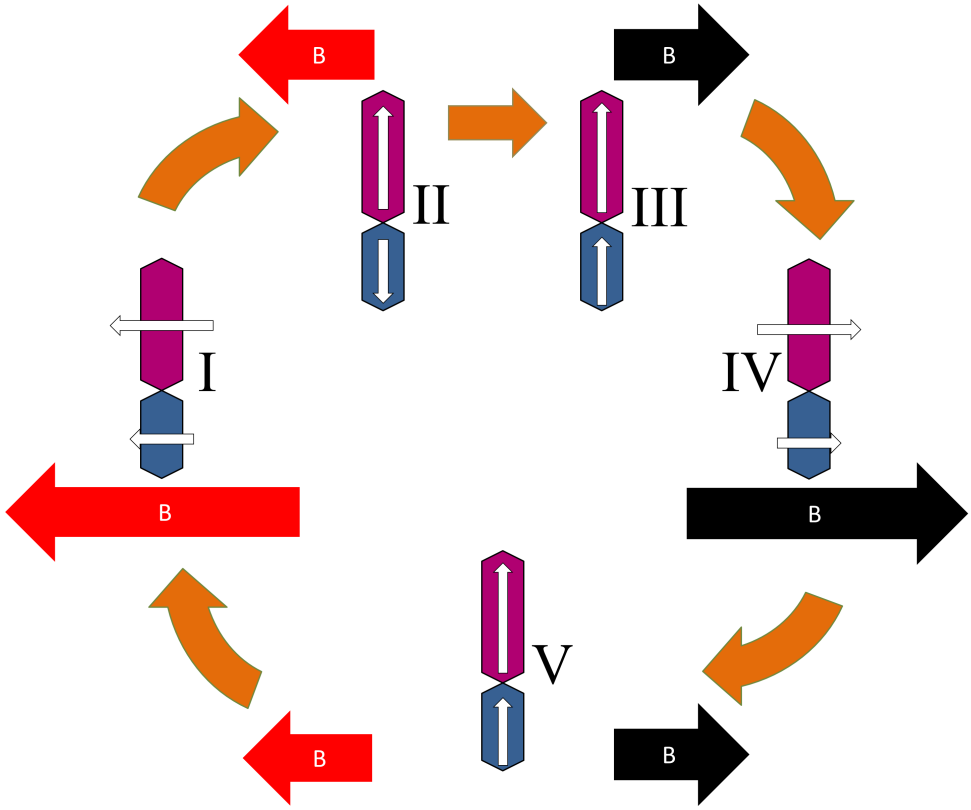

Figure 28: Possible magnetization rotation sequence leading to the observed MR characteristics in case of the perpendicular configuration of field and nanocluster arrangement. The big red arrows represent the external magnetic field, the white arrows depict the cluster magnetizations.

For the measurement with the external magnetic field parallel to the cluster's elongation direction (figure 25), the energy landscapes for different fields are shown in figure 26, and the

explanation for the MR characteristics is shown in figure 29. At waypoint I, the external field is at -10 T and both cluster magnetizations are parallel aligned to it. With decreasing field, the restriction to the minimum in the elongation direction gets weaker, and the magnetization of the smaller cluster jumps in the adjacent minimum caused by the magnetocrystalline anisotropy. This jump causes the first MR jump in figure 25. Since this happens prior to the field polarity change, one can suppose that this jump is thermally activated. Such thermal effects are further described and explained in chapter 6.1. After the jump and with decreasing and afterwards invertedly rising external field (waypoint III), the magnetization of the larger cluster follows continuously. With this process, the relative angle between the magnetization direction decays continuously to zero, causing the MR to fall to the baseline until the external field has reached +10 T. Here, at waypoint IV, both magnetizations point in elongation direction and are aligned parallel to the external field. With falling field around waypoint V, the magnetizations stay in their shape anisotropy minima, which persists over the field inversion point. With rising inverted field at waypoint VI, the small cluster jumps into an adjacent minimum caused by the magnetocrystalline anisotropy, since the increasing Zeeman contribution in the energy landscape lets the shape anisotropy minimum pointing in opposite field direction become shallow, before it completely vanishes. This magnetization jump causes the second MR jump in figure 25. Afterwards, the larger cluster turns its magnetization continuously towards field direction until both cluster magnetizations are aligned parallel to the external magnetic field and parallel to each other.

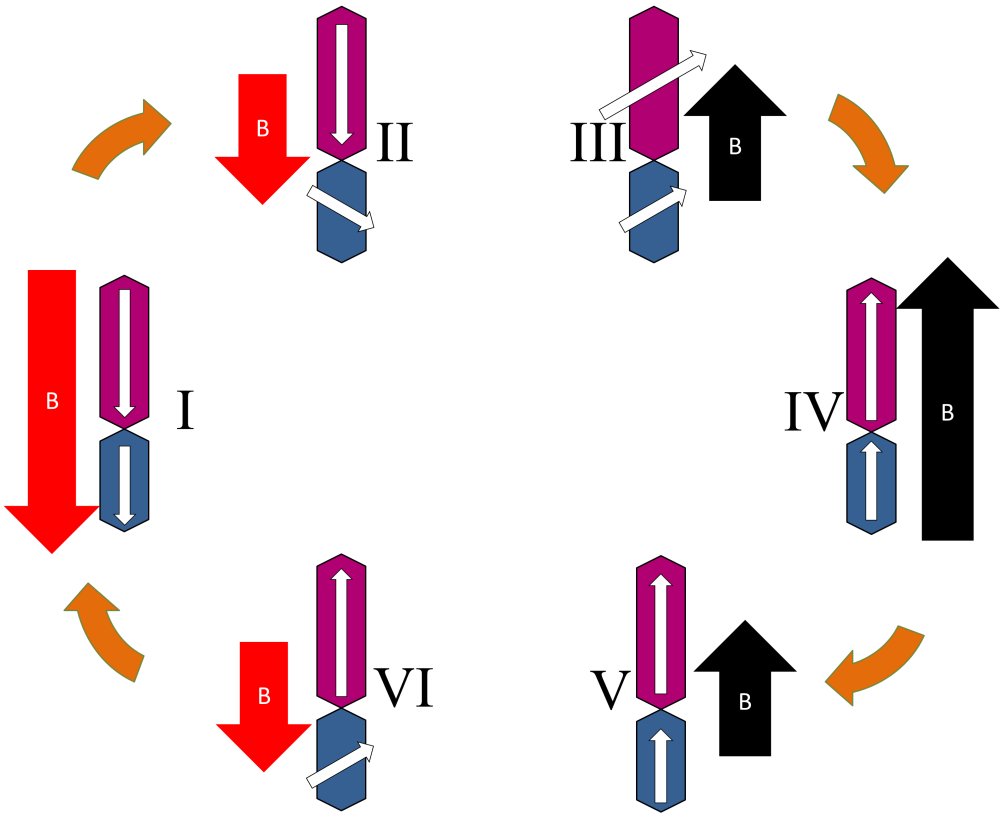

Figure 29: Possible magnetization rotation sequence leading to the observed MR characteristics in case of the parallel configuration of field and nanocluster arrangement. The big red arrows represent the external magnetic field, the white arrows depict the cluster magnetizations.

These explanations show that the model based on the cosine-like angle-resistance function and energy density landscape is applicable to find possible sequences of the change of the magnetic structure of the clusters related to the observed MR effects. However, in case of the first jump in the parallel configuration, the model reaches its limit when the consideration of a thermally influenced jump in advance to the field inversion needs to be assumed in order to describe the experiment. Also, in case of the perpendicular configuration, an explanation can be found, however, it still contains a certain randomness regarding the information whether the clusters jump into a parallel (falling field branch) or antiparallel (rising field branch) orientation. This lack of information is caused by the rather small amount of information one can achieve about the magnetic structure of the cluster system during the measurement. The only measure and thus certain information one achieves in situ with changing external field and a defined sample temperature is the overall resistance which is measured. All other considerations including the energy landscapes, conductivity characteristics and magnetization directions are based on considerations about known facts which yield a certain picture of the observed phenomena's

roots when combined.

Despite these limitations, one finds a correlation between observed MR jumps and the nanocluster arrangement's setup together with the external circumstances. The central information of these measurements and the related considerations is that

- MnAs nanocluster arrangements show discrete magnetoresistance jumps and
- the observed features can be correlated to external influences as well as properties of the material system and the structure's geometry.

5.3 Background function

As mentioned above, the background of the MR measurements seen in figures 23 has been subtracted to provide a better visibility of the investigated jump features. Figure 30 shows the subtracted background function as well as the corresponding sample temperature for each measurement point. The temperature has a deviation at the beginning of the measurement around -10 T caused by a not yet reached equilibrium temperature of the sample itself. This effect can also be seen in the MR background in the same region. Besides that, one can observe a "butterfly"-like temperature progress, which is caused by a MR effect in the resistive temperature sensor attached to the cryostat chamber, influencing the temperature control to slightly adjust the cryostat temperature. A certain delay in this process causes the butterfly-like asymmetry. This effect is considered as small, however, it is also accounted for the subtracted background function.

Up to 1 T, the MR has a parabolical characteristic, which can be related to the ordinary MR, described in chapter 3.1, acting on the conducting parts of the structure. Above 1 T, the dominating effect in the MR background is a positive, large linear magnetoresistance. This effect has also been observed by Johnson et al. in other, strongly disordered MnAs-GaAs hybrids, where its MR ratio is found to increase at lower temperatures[Joh10]. In case of the nanoclusters, it is supposed that a part of the probe current flows through the GaAs matrix below the MnAs clusters. Since the samples are grown at comparatively high temperatures, one can assume that diffusion takes place and Mn atoms migrate into the GaAs matrix, generating a disordered MnAs-GaAs hybrid. The shunting current passes through these areas and experiences a linear magnetoresistance, which then appears in the MR measurements.

The visibility and magnitude of this effect is, on the one hand, an indication that the isolation between the nanocluster structures and the GaAs matrix needs to be improved. Depending on the respective sample, the observed linear MR effect varied in its magnitude - while the

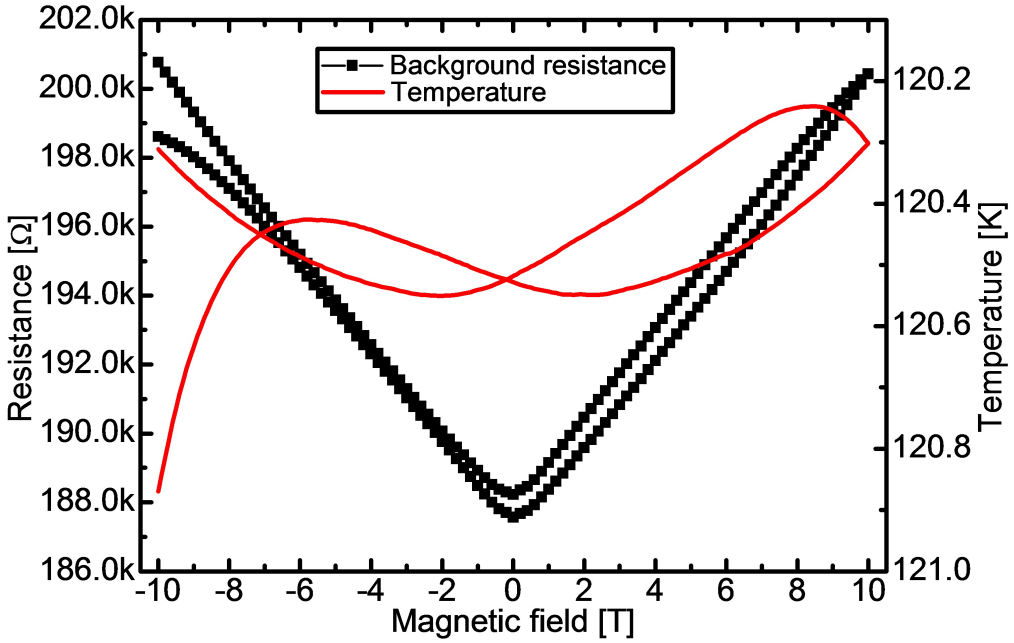

Figure 30: Subtracted background function for the measurement of the parallel configuration of cluster arrangement and external field. The black dots show the MR background, the red curve indicates the sample temperature drift over the measurement.

(uncorrected) MR curves on the sample observed in figure 20 showed only a slight linear MR and comparatively high MR ratio jumps, the linear MR is dominant in other measurements, as shown e.g. in figure 23. This variation can be interpreted as a variation in isolation quality between cluster and matrix material. On the other hand, it gives an explanation on the comparatively low MR ratio observed in the jump features. Since only a part of the current passes the clusters and thus the domain interfaces, only this part undergoes the influence of the spin-dependent transport through these structures.

6 Thermally activated magnetoresistance effects

6.1 Néel-Brown-Law

With decreasing spatial extensions in the low sub-micron scale regions, magnetoelectronic device structures suffer increasingly from the influence of thermal energy. The magnetization of a single domain particle is kept in a certain direction mainly by anisotropy effects (see chapter 2). Anisotropy constants can be understood as energy densities. This means that the energies which apply for a certain magnetic domain scale with the domain volume. With decreasing domain sizes, the probability of a magnetization inversion is rising. Plenty of research work has been performed addressing the influence of thermal energy on the behavior of micro- and nanoscopic magnetic systems.[Atk03 All94] A first quantitative description of this phenomenon has been given by the Néel-Brown-law in 1949:[Nee49 Bro63]

$$\frac{1}{\tau} = f_0 \cdot e^{-\frac{\Delta E}{kT}}, \tag{25}$$

where τ represents the mean residence time during which a defined magnetic state is persistent, f_0 is the attempt frequency and ΔE is the energy barrier which has to be overcome by the magnetic particle in order to reorient its magnetization. The attempt frequency can be seen as an upper limit of "attempts" the particle undergoes to change its magnetization state, while the exponential factor defines the probability of how many of those attempts will result in a magnetization state change.[Cof12] This defines the mean time this particular magnetic state will be occupied by the particle.

The value of the attempt frequency depends on experimental conditions such as the particle volume, the material system including its anisotropy effects and also the temperature.[Dic93 Sta59] Typical values for f_0 are in the range of 10^9 to 10^{13} Hz[Les96], however, they can also vary strongly depending on the experimental conditions.[Bod04]

The energy ΔE, which keeps the single domain particle in a certain magnetic state, can be seen as the barrier in the energy landscape which confines this magnetic state. As mentioned above, an energy landscape is influenced by the magnetocrystalline anisotropy energy and, if present, the shape anisotropy energy. In addition, coupling to other magnetic particles can also influence the energy barrier (see chapter 2, superparamagnetism). External magnetic fields can also play a role, since they strongly influence the energy landscape over the Zeeman energy contribution. An applied external magnetic field flattens or, depending on the field value and anisotropy constant, defines minima in the energy landscape. This effect is, for example, demonstrated in figures 26 and 27.

The Néel-Brown-law applies only for single-domain particles up to a certain size. Wernsdorfer et al. have found that in case of elongated nickel nanowires with a diameter of about 65 nm and a length of 2 µm, the Néel-Brown law does not apply, since the magnetization reversal is performed in a nucleation process. The initial volume of this process is around two magnitudes smaller than the actual nanowire.[Wer96] However, they showed that the Néel-Brown-law applies for ferromagnetic particles with a size of 15 to 30 nm.[Wer97].

6.2 Dynamic effects in MnAs resistance measurements

During the investigations of the magnetoelectronic properties of MnAs nanoclusters, several resistance jumps have been observed which could not be reproduced by repeating the corresponding external magnetic field sequences. An example for these randomly occurring jumps in a MR measurement can be seen in the set of measurement graphs shown in figure 20 of chapter 5. Here, many jumps occurred during the whole measurement sequence, however, they did not appear at recurring positions in the external magnetic field sequences. These randomly-appearing resistance changes can be traced back to the influence of thermal energy on the micromagnetic structure of the sample. Based on the thermal origin and the random-like appearance of this effect being comparable to random telegraph noise, it is referred to as magnetic random telegraph noise (RTN).[Fi15b] Although RTN is a random phenomenon, its characteristic parameters like the frequency and the recurring probability of certain states can be correlated with the respective temperature of a measurement, as described in the passage above. In front of this background, the RTN in MnAs nanocluster samples is investigated and described qualitatively and quantitatively.

The transport measurements for the investigation of thermally activated, dynamic effects in MnAs nanoclusters have been performed on two different nanocluster samples shown in figure 31. The first sample is a comparatively simple lateral nanowire-like structure with four contacts attached. One of these contacts, which can only be seen as a shadow in the SEM image, has been damaged during the lithography processing. The remaining three contacts subdivide the cluster into one shorter and one longer section. The longer section, which has a length of about 3.5 µm and a width of 400 nm has been used for the measurements. In this section, the cluster exhibits a partly rough morphology at its lateral edges.
The second sample shows a slightly more complex geometry: it consists of two elongated nanoclusters with different lengths, which enclose a relative angle of 120 ° and are merged at their interface. The longer cluster has a length of around 950 nm, the smaller of around 600 nm, while both have a width of around 300 nm. The merging area is indicated by a constriction where the cluster arrangement has a width of only 250 nm.

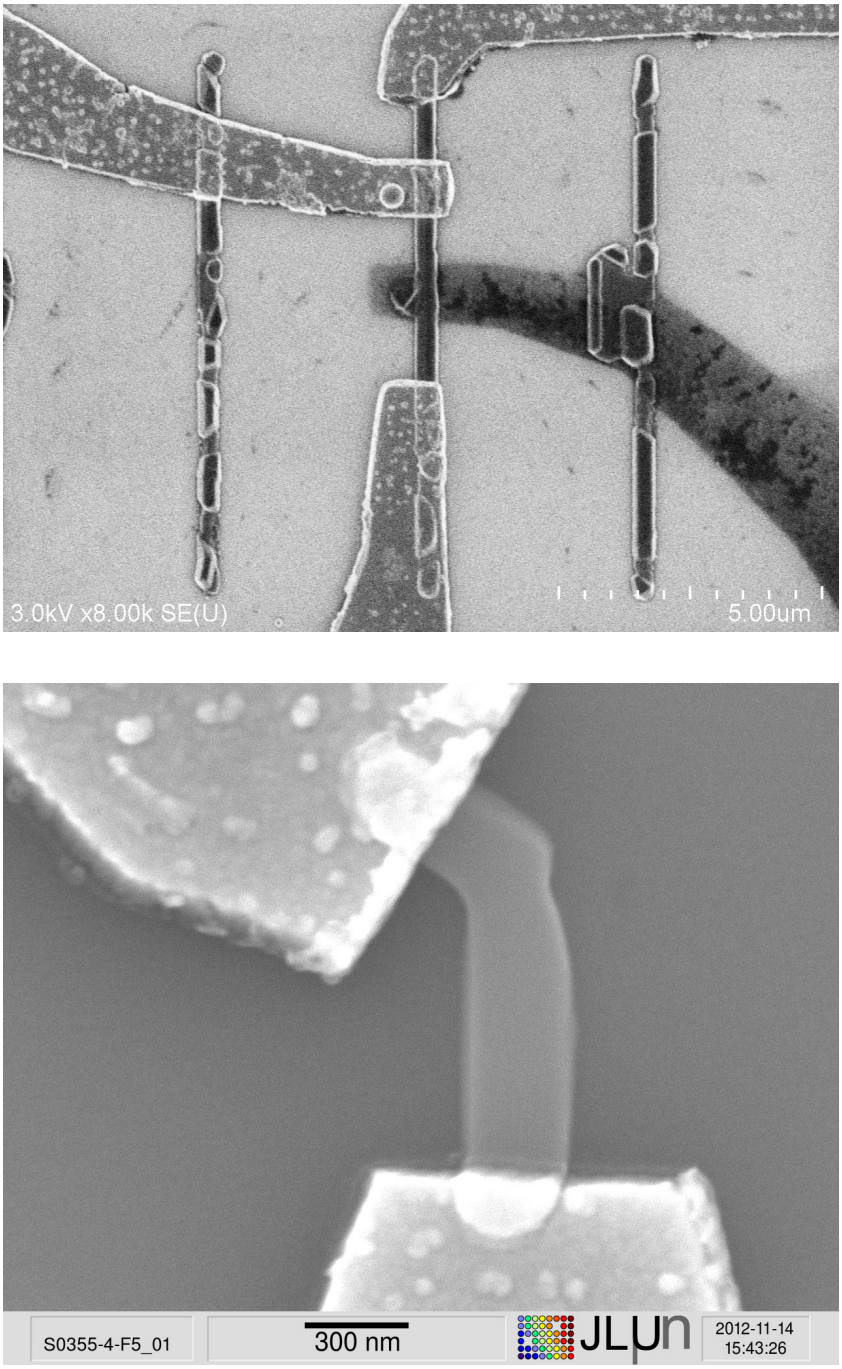

Figure 31: Top image: Scanning electron microscopy image of a nanowire-like cluster, bottom image: Scanning electron microscopy image of a merged, angled two-cluster arrangement.

Kato et al. have shown that elongated, nanowire-like MnAs clusters with no spatial partition can form several magnetic domains.[Kat15] Thus, the formation and stabilization of a micromagnetic structure including domain walls and small, intermediate domains between larger adjacent

domains is possible. A simple approach is a model system consisting of three domains with two interfaces. If one assumes that the two larger domains keep fixed magnetization directions, while the intermediate domain with its comparatively small volume can undergo thermally activated magnetization switching occurring on measurable time scales, it is likely that thermally activated fluctuations can also be observed in the resistance measurements. The fixing of the larger domain magnetizations can be explained by the relatively high barriers in the energy landscape, while the magnetization of the intermediate domain with its small volume encounters smaller energy barriers, enabling it to revert its magnetization direction by thermal activation. The resistance of this model arrangement is then a function of the intermediate domain's magnetization direction, since the other magnetization directions are fixed. It determines the MR of both domain walls. A schematic drawing of this model for the two investigated structures can be seen in figure 32.

The time-dependent resistance measurements on the two shown samples have been performed without and with applied constant external magnetic fields and at several constant sample temperatures. Depending on the measurement routine used, which determines the required apparative sequences, the acquisition time for one datapoint varied between 15 and 25 seconds, approximately. Figure 33 shows measurements on the nanowire-like structure shown in figure 31(top). Three measurements with different sample temperatures (154 K, 160 K, 165 K) have been performed on this sample, all with a probe current of 2 nA and absent external magnetic field. They have been normalized for comparison.

In all three measurement curves, one can see that the resistance shows jumps between two recurring values. Between the jumps, the resistance stays on the level within a certain, usual range of noise. The time intervals between the jumps define the occupation durations of a certain state corresponding to a respective resistance value. It varies from step to step and appears to be subject to a random process. However, one can observe that the average time which the system spends in one of the resistance states, referred to as the "mean residence time" in the following, changes for different temperatures. With increasing temperature, one can observe that the residence time intervals become shorter for both occupied states. While the shown section of the 154 K measurement contains five jumps, the 160 K measurement exhibits 30 and the 165 K measurement 60 jumps.

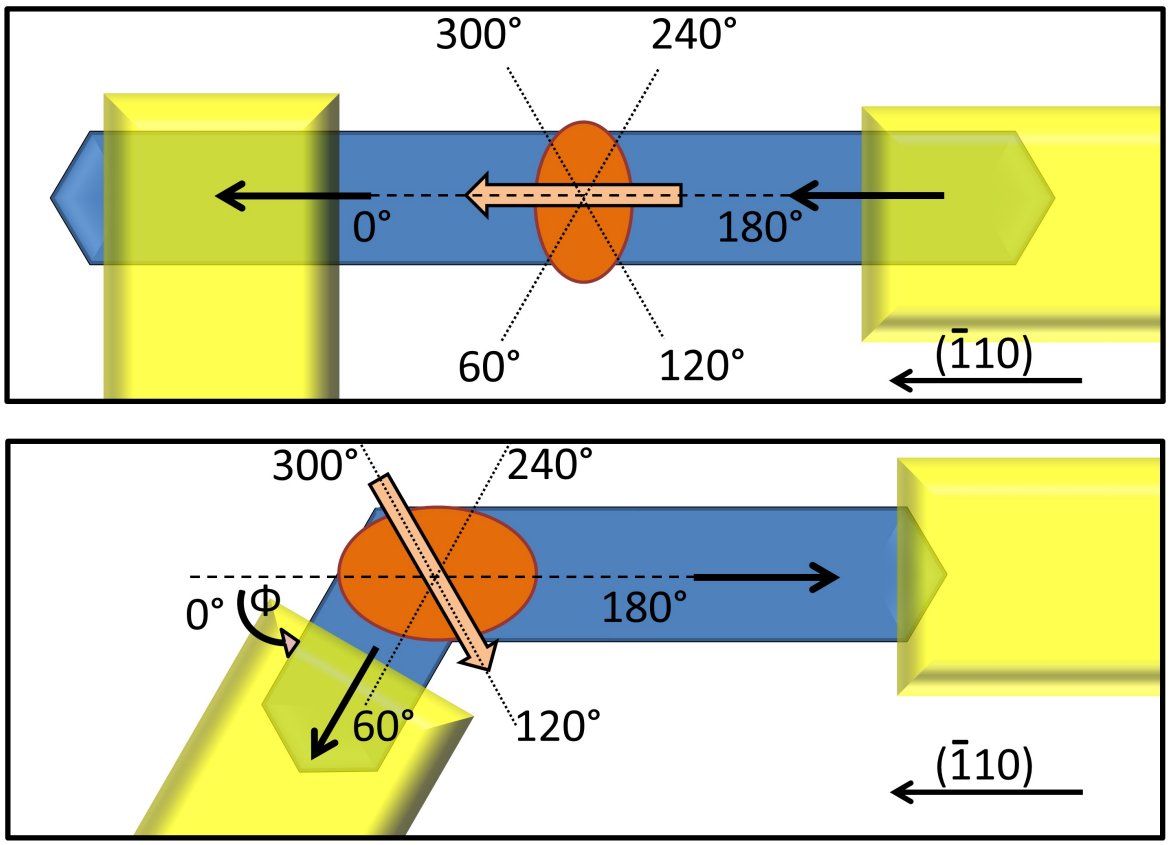

Figure 32: Three-domain-models for the two thermally investigated samples. The upper image shows the nanowire sample, the lower shows the angled nanocluster arrangement. The blue areas represent the external domains with fixed magnetizations (shown as black, solid arrows), while the deep orange area depicts the intermediate domain with its variable magnetization orientation (bright orange).

Figure 34 shows four time-dependent measurements on the merged, angled nanocluster sample seen in figure 31(bottom). The measurements were performed at 65 K, twice at 70 K, and 80 K. In the 65 K-measurement, one can observe that three resistance levels are occupied by the system. In the measurements at the two higher temperatures, only two resistance levels are occupied in the measurements, whereas several narrow jumps in the first 70 K-measurement indicate short occupations on the lowest level, which are not resolvable at this measurement repetition rate. At 80 K, also the jumps between the two stronger occupied levels become partly non-resolvable due to the repetition rate. Again, one can observe that the mean residence time for all resistance states decreases with increasing temperature. Concerning the occupation of

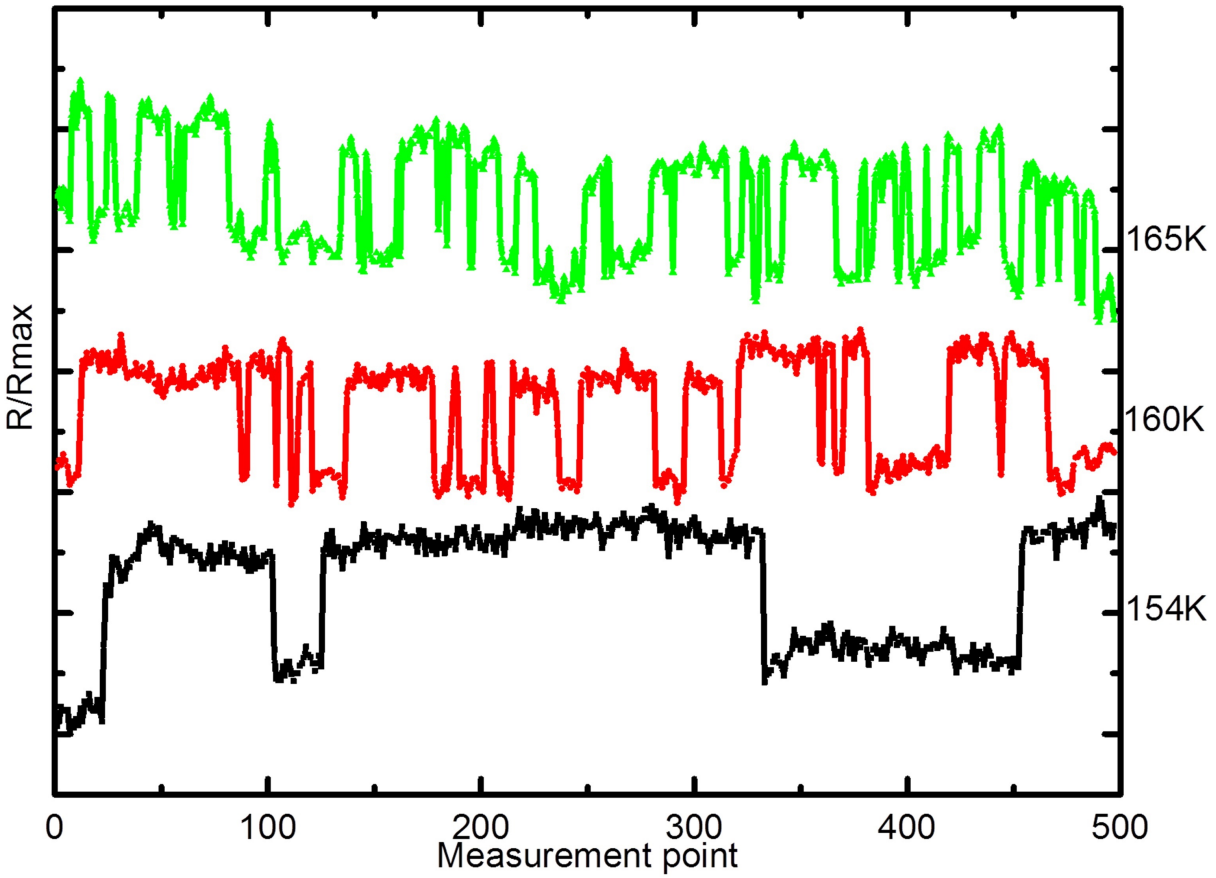

Figure 33: Time-dependent measurements on the nanowire-like cluster shown in figure 31(top). The total of 500 datapoints corresponds to a time interval of approximately 2 hours.

the resistance levels, the middle level is the most occupied one, followed by the higher and then the lower level.

For a quantitative examination of these thermally induced phenomena, the mean residence times and the occupation probabilities for the respective levels in all measurements have been counted and are evaluated in the following. The recurring resistance levels are not categorized by their absolute values here, since the ohmic resistance of the whole system comprising clusters, matrix and contacts also shows a temperature dependence, which hinders the comparability of absolute resistance values at different temperatures. Instead, the resistance levels are distinguished relative to each other as low, middle (in case of the merged, angled cluster sample), and high level.

6.2.1 Mean residence times

Figure 35 shows the mean residence times for the two observed resistance levels on the single elongated cluster sample (figure 31(top)). For the measurement at 154 K, the higher resistance

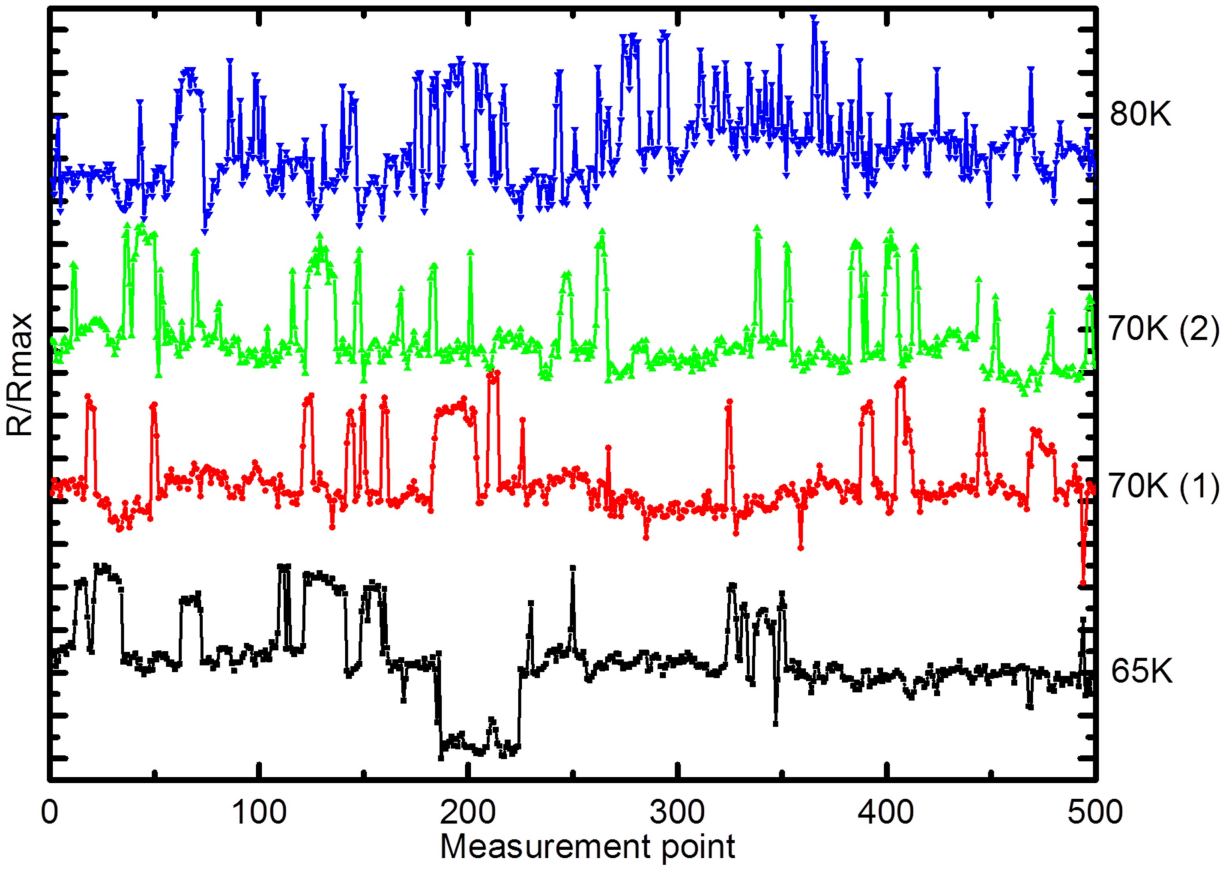

Figure 34: Time-dependent measurements on the merged, angled nanocluster arrangement shown in figure 31(bottom). The total of 500 datapoints corresponds to a measurement duration of approximately 2 hours.

level (level 2) has a mean residence time of 2975 s, which is more than twice the value of the mean residence time of the lower resistance level (level 1) with 1381 s. In the intermediate temperature measurement at 159 K, the difference between the two mean residence times is significantly smaller, with 262 s for level 2 and 334 s for level 1. At the highest temperature (164 K), the mean residence time is 125 s for level 2 and 108 s for level 1.

The mean residence times for the three levels in the measurements on the merged, angled two-cluster sample (figure 31(bottom)) are shown in figure 36. For the intermediate temperature value of 72 K, two measurements were performed. At all temperatures, the highest mean residence time is found for the middle resistance level (level 2) with 414 s at 67 K, 408 s and 346 s at 72 K and 191 s at 83 K. The highest resistance level 3 shows an intermediate mean residence time in all cases. It is 104 s, at 67 K, 141 s and 70 s at 72 K and 53 s at 83 K. The lowest resistance level 1 always shows the shortest mean residence times. At 67 K, it measures 49 s, and 26 s and 16 s at 72 K. At the highest temperature of 83 K, this resistance level was not observed at all.

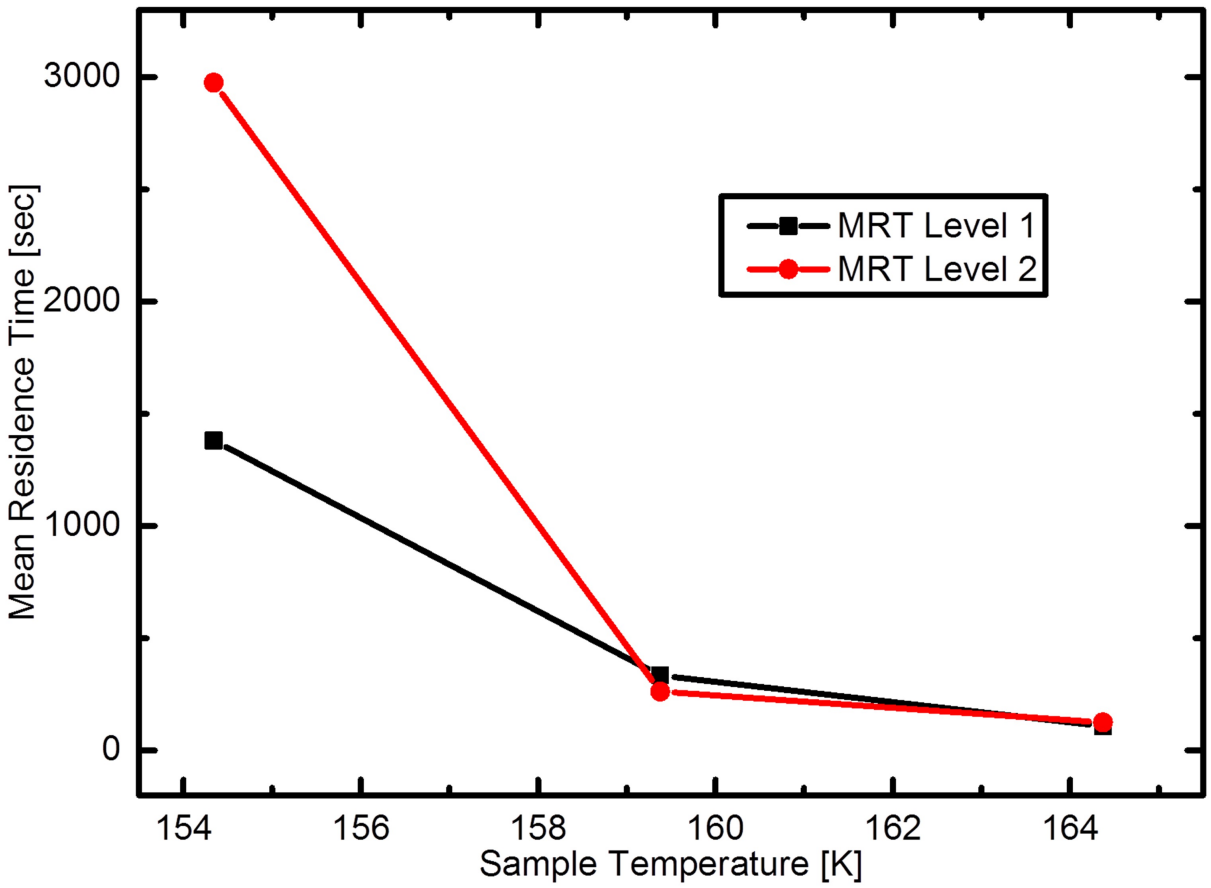

Figure 35: Mean residence times (MRT) for the two resistance levels observed on the nanowire sample.

In the case of all observed levels in both samples, one can see a general trend of a falling mean residence time with rising temperature. This effect can be qualitatively explained using the Néel-Brown-law which is explained above in equation 25. Given a model system with a small, fluctuating domain as described before, one can assume that the magnetization of this domain points in a certain direction, represented by a minimum in the cluster's energy landscape confined by an energy barrier ΔE. At a temperature T, the mean residence time τ specifies the average time until the magnetization is rotated into another direction by thermal excitation. If the temperature rises, the exponential term takes on a higher value and thus the mean residence time falls. This trend can be seen more or less clearly for all levels in the above figures. However, one can observe that the slopes of the levels have different values. This appears very clearly in case of the nanowire measurements (figure 35) between 154 K and 159 K, for example. The explanation for this behavior can also be found in the energy landscape for the small intermediate domain. If one assumes that the energy landscape is formed by the magnetocrystalline and shape anisotropy as well as the coupling energies to the adjacent big domains, one can imagine

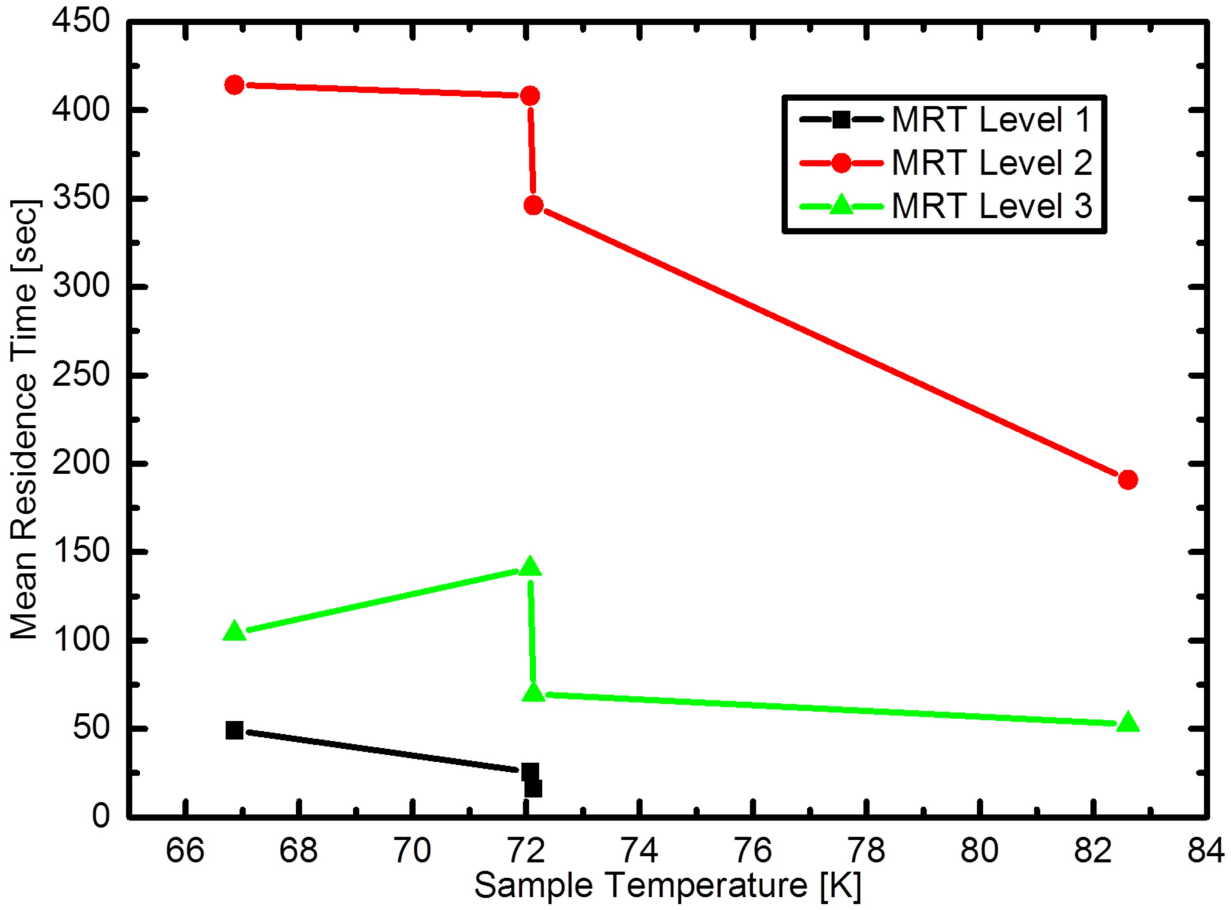

Figure 36: Mean residence times (MRT) for the three resistance levels observed on the angled nanocluster arrangement.

that the occurrence of minima with different barrier heights is possible. In addition, one has to consider that an energy landscape with six different minima causing a resistance distribution with only two or three levels shows a degeneracy, meaning that more than one magnetization orientation leads to the same resistance level. A more detailed, quantitative treatment of these considerations is shown in chapter 6.2.3.

6.2.2 Occupation probabilities

The occupation probabilities $p_{occ}(\text{Level } x)$ of the observed resistance levels were calculated as the ratio of the overall time spent in one resistance state and the complete measurement time:

$$p_{occ}(\text{Level } x) = \frac{t_{occ}(\text{Level } x)}{\sum_{i=1}^{n} t_{occ}(\text{Level } i)}, \tag{26}$$

with $t_{occ}(\text{Level } x)$ as the total time the resistance limit x is occupied in one measurement. n is the number of resistance levels which are observed in one measurement.

In case of the nanowire sample, the occupation probabilities are shown in figure 37. While the probabilities at 154 K differ strongly with 68 % for the higher resistance level 2 and 32 % for the lower resistance level 1, the probabilities at 159 K and 164 K are much more equally distributed with values near 50 %.

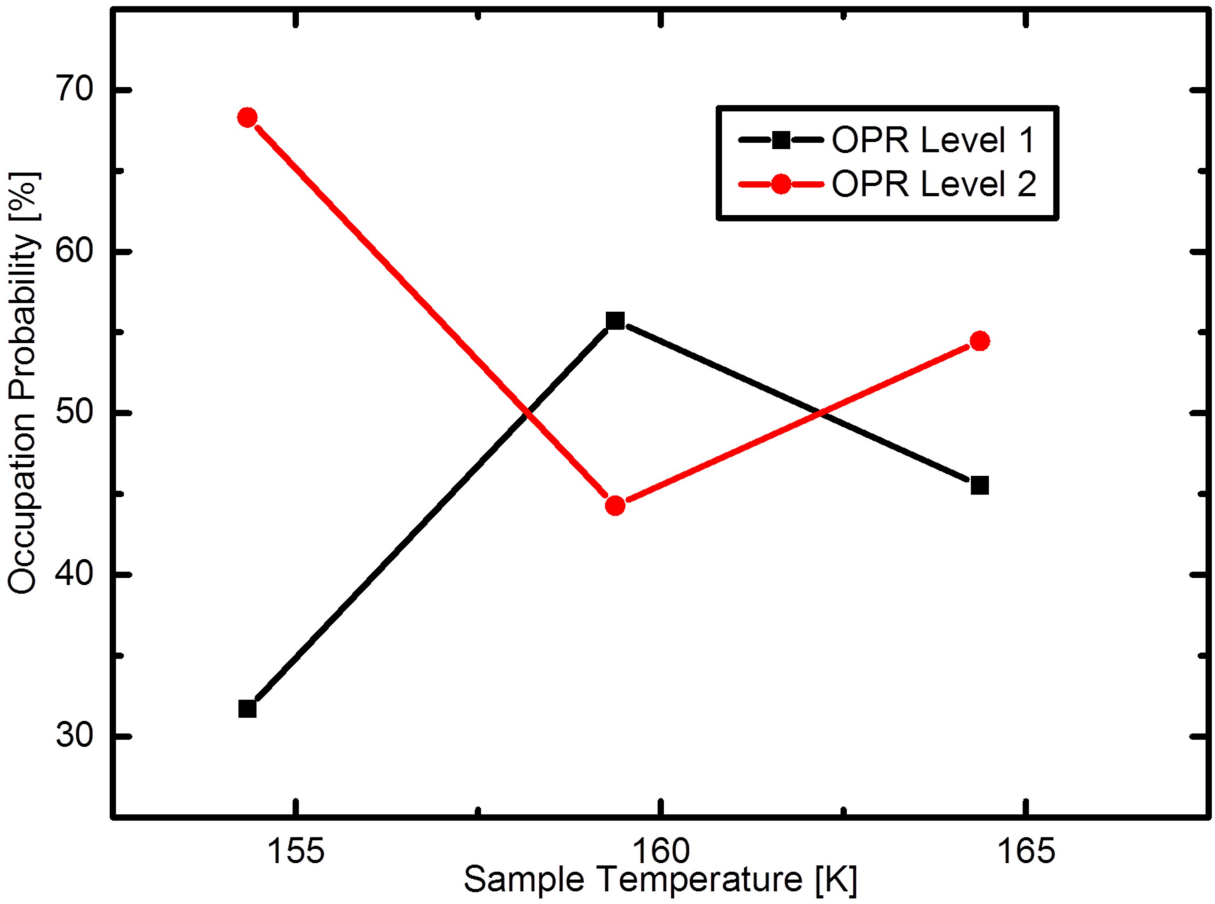

Figure 37: Occupation probabilities for the two resistance levels observed in the nanowire sample.

For the angled sample, the occupation probabilities are shown in figure 38. Here, the distribution is more distinct compared to the case of the nanowire sample. The dominant resistance level at all temperatures is the middle resistance level 2, which occupies around 80 % of the measurement time in all cases. It is followed by the highest resistance level 3 which takes on about 20 % of the measurement time. The lowest resistance level 1 is hardly occupied. While its occupation probability in case of the 67 K measurement is around 3 %, it is only observed for very short periods in the range of several measurement steps at 72 K, resulting in probabilities of clearly beyond 1 %.

The consideration of the occupation probabilities has to be seen critically, especially concerning

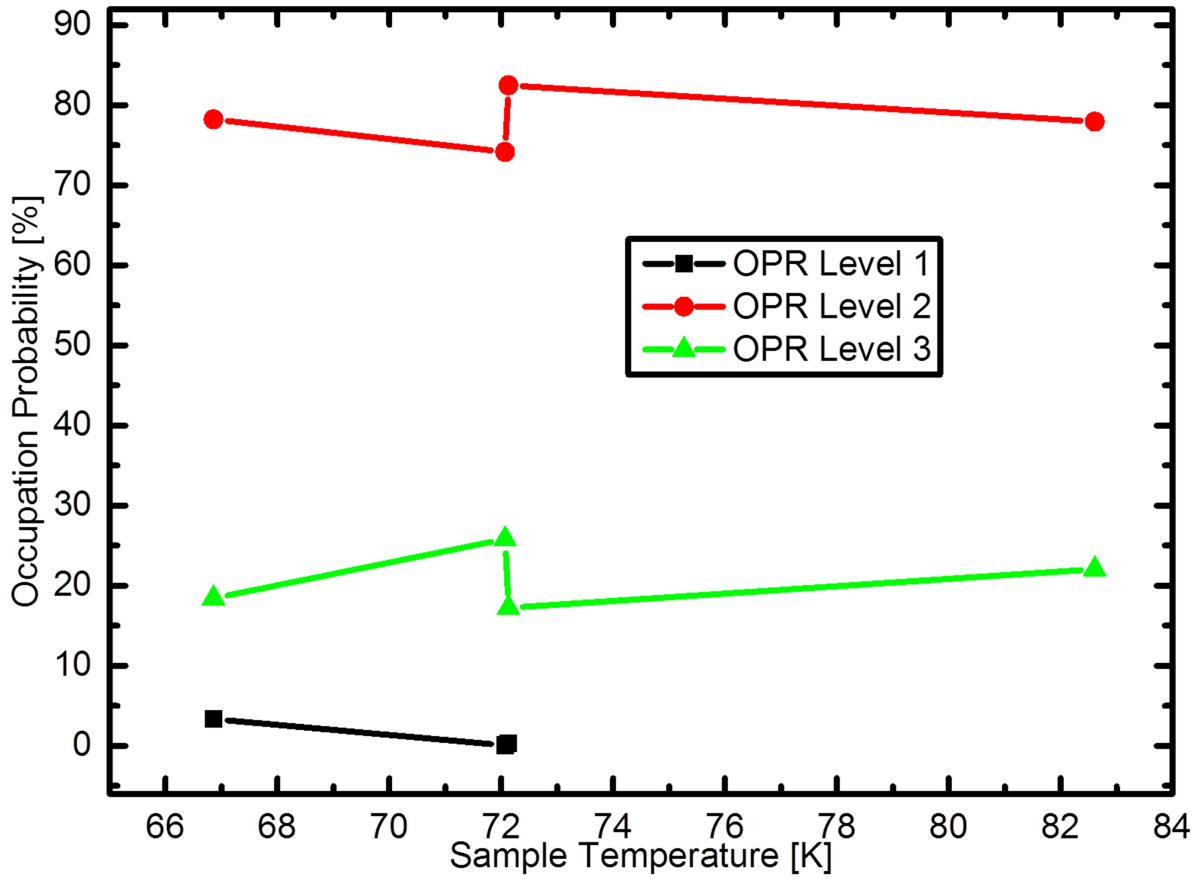

Figure 38: Occupation probabilities for the three resistance levels observed in the angled nanocluster arrangement.

the low temperature measurements. Taking a look at the measurement graphs in figures 33 and 34, one can observe that in case of the lowest temperatures only a few measurement periods per level can be observed. In case of the nanowire sample, only three periods on each observable level occur, resulting in a comparatively high statistical error. However, in case of the angled nanocluster sample, the mean residence times are lower, resulting in a higher count of segments per resistance level and thus a better statistical quality.

6.2.3 Energy landscape fit

The free energy E_I of an intermediate domain enclosed between two fixed, big domains and regarding its in-plane orientation angle Φ is

$$E_I = E_{\mathrm{Z}} + E_{\mathrm{A,mc}} + E_{\mathrm{A,sh}} + E_{\mathrm{cpl},1} + E_{\mathrm{cpl},2}, \tag{27}$$

$$= -V_{\mathrm{I}} \cdot M_{\mathrm{MnAs}} \cdot B \cdot cos(\Phi - \Theta) + V_{\mathrm{I}} K_{mc} \cdot sin(6\Phi) + V_{\mathrm{I}} K_{\mathrm{sh}} \cdot sin(\Phi - \epsilon)^2 \tag{28}$$

$$- J_1 M_{\mathrm{MnAs}}^2 \cdot cos(\Phi - \gamma_1) - J_2 M_{\mathrm{MnAs}}^2 \cdot cos(\Phi - \gamma_2),$$

with E_{Z} for the Zeeman energy with V_{I} as the volume of the intermediate domain, M_{MnAs} for the magnetization of MnAs and B for the external field oriented in angle Θ. $E_{\mathrm{A,mc}}$ represents the magnetocrystalline anisotropy energy with K_{mc} as anisotropy constant, and $E_{\mathrm{A,sh}}$ stands for the shape anisotropy energy with K_{sh} as shape anisotropy constant and ϵ as the elongation direction of the domain's shape. The terms $E_{\mathrm{cpl,i}}$ are the energies resulting from coupling to the magnetizations of the adjacent domains, with J_{i} as the respective coupling constants and γ_{i} as angles describing the orientations of the adjacent magnetization's orientations. For simplification, the coupling constants J_{i} contain the volumes of the domains involved as a factor: $J_{\mathrm{i}} = J \cdot V_{\mathrm{I}} V_{\mathrm{i}}$, with V_{i} as volumes of the adjacent domains.

The magnetization M_{MnAs} is a constant which is calculated as a product of the Mn density in MnAs, $n_{\mathrm{MnAs}} = 2.96 \cdot 10^{28}\ m^{-3}$, and the magnetic momentum per Mn atom, which is $3.4\,\mu_B$: $2.96 \cdot 10^{28}\ m^{-3} \cdot 3.4\ \mu_B = 9.33 \cdot 10^5 \frac{J}{T \cdot m^3}$.[Har03]The magnetic anisotropy constant for the in-plane hexagonal anisotropy term has been determined by M. T. Elm as $1.62 \cdot 10^5 \frac{J}{m^3}$ in SI units, using a curve fit on FMR measurements.[El10b] The remaining parameters such as the domain volume, shape anisotropy constant and the coupling constants serve as degrees of freedom for a fit of the determined values for the mean residence times at the different temperatures.

Prior to performing the fit, one has to consider several assumptions to simplify the computational process. To perform a fit of the measured mean residence times, one has to define a fit function describing this time based on the energy landscape of the intermediate cluster. If one assumes that the mean residence time for an orientation of the intermediate domain's magnetization (corresponding to a resistance level) is defined by the energy barrier confining this state, one has to determine the energy barrier height to perform the calculation. Since an energy landscape can show asymmetrically confined minima, i.e. minima which are confined by two barriers of different height, the depopulation of a state can happen with two different mean residence times. To take both into account, one forms the depopulation frequency as the reciprocal of the mean residence time. This frequency can be seen as the number of successful depopulations of the magnetic state over the respective energy barrier per time. Since two possible energy barriers can confine the minimum, one can sum up the two particular depopulation frequencies to the overall depopulation frequency of this minimum. It is further assumed that a depopulation from a state being represented by a minimum in the energy landscape takes only place by a jump into a neighbouring minimum. This strongly simplifies the number of possible depopulation channels.

Another issue to be dealt with is the degeneracy of the resistance levels, since more than

one minimum may contribute to a single resistance level, when a six-minimum magnetic energy landscape causes a three-level resistance distribution. Similar to the case above, this situation is dealt with by just adding up the respective depopulation frequencies of all minima contributing to a certain resistance level. One then achieves an overall depopulation frequency for this resistance level, which reciprocally is the mean residence time for this resistance level.

The energy landscape used for the fit of the mean residence times of the nanowire sample is shown in figure 39 as a blue curve. In this case, the coupling to the two adjacent domains with their magnetizations oriented towards the $(\bar{1}10)$-direction, which is identical to the Φ=0 -direction in sample plane, is supposed to be very dominant, resulting in an energy landscape with only three relevant minima. A contribution of the minimum at 180 ° is not taken into account due to its energetically unfavorable high position and flat energy barriers. The corresponding resistance diagram is shown as red curve. One can see that the three minima, named A, B and F, form a resistance distribution of two levels R1 and R2, which is in accordance to the observed phenomena.
This energy landscape is in accordance with the significantly different occupation probabilities observed at the lowest temperature: the degeneracy of resistance level 2 being fed by two minima while level 1 is not degenerate might be a key for understanding this phenomenon. Based on the shown energy landscape characteristics, the fit functions for the mean residence times τ_1 for level R1 and τ_2 for level R2 in the nanowire measurement have been set up as follows:

$$\tau_1 = (f_0 \cdot (e^{-\frac{E_{A\to B}}{kT}} + e^{-\frac{E_{A\to F}}{k_B T}}))^{-1} \quad \text{and} \tag{29}$$

$$\tau_2 = (f_0 \cdot (e^{-\frac{E_{B\to A}}{kT}} + e^{-\frac{E_{F\to A}}{k_B T}}))^{-1}, \tag{30}$$

with f_0 as attempt frequency, $E_{X\to Y}$ as barrier heights for the respective magnetization orientation changes from minimum X to minimum Y, k_B as Boltzmann's constant and T as temperature. The energy barriers are calculated from the energy landscape as the difference of the energy maximum between the two minima and the energy of the initial minimum.

These expressions can be understood by taking a look at the energy landscape of the nanowire sample in figure 39. The low resistance level R1 can only be observed when the magnetization direction points in the direction of in minimum A. A measurement period occupying resistance level R1 ends when the magnetization leaves minimum A towards minimum B or F. This change happens over the energy barriers $E_{A\to B}$ or $E_{A\to F}$. Backwards, when the resistance level R2 is occupied, the magnetization is oriented in minimum B or F. This state is degenerate, since two different minima yielding the same resistance value contribute to it. It changes with the magnetization leaving one of those minima towards minimum A over the energy barriers $E_{B\to A}$

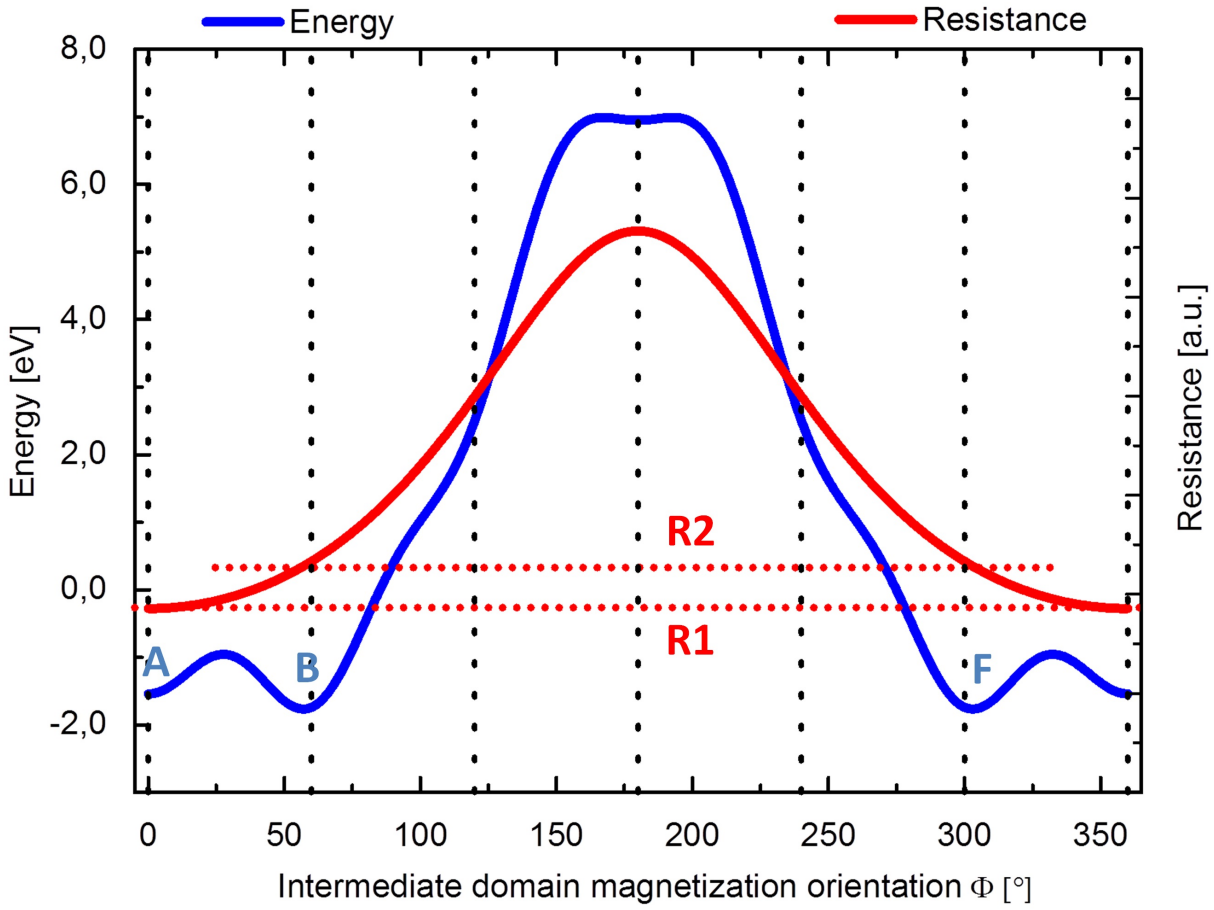

Figure 39: Energy landscape (blue) and resistance characteristics (red) for the in-plane magnetization orientation of the intermediate domain in the nanowire sample. The two resistance levels arising from the three minima are shown as dashed red lines.

or $E_{F\to A}$. The fit of the measured mean residence times for the nanowire sample is shown in figure 40, plotted in an Arrhenius graph logarithmically against the reciprocal temperature. The dots represent the measured mean residence times with statistical error bars, the lines depict the fit curves. The values for the energy landscape used for the fits are $f_0 = 5 \times 10^{12}\,\mathrm{Hz}$, $J1 = J2 = 3.8 \times 10^{-31}\,\frac{T^2 m^6}{J}$, $V_\mathrm{D} = 3.814 \times 10^{-25}\,m^3$ and $K_\mathrm{shape} = 1.2566 \times 10^6\,\frac{J}{m^3}$. These are also the values with which the energy landscape shown in figure 39 was calculated. The comparison between measured values with error bars and the fit curves show a quite good agreement, except the level 2 value for the middle temperature, which is slightly off the fit curve.

The energy landscape used for the fit of the angled nanocluster sample is shown in figure 41. Here, the two adjacent domains are supposed to point in the directions of their cluster's elongation, with the smaller domain pointing at 60 ° and the bigger at 180 ° like shown in the schematic drawing in figure 32. The intermediate domain is described with a shape anisotropy

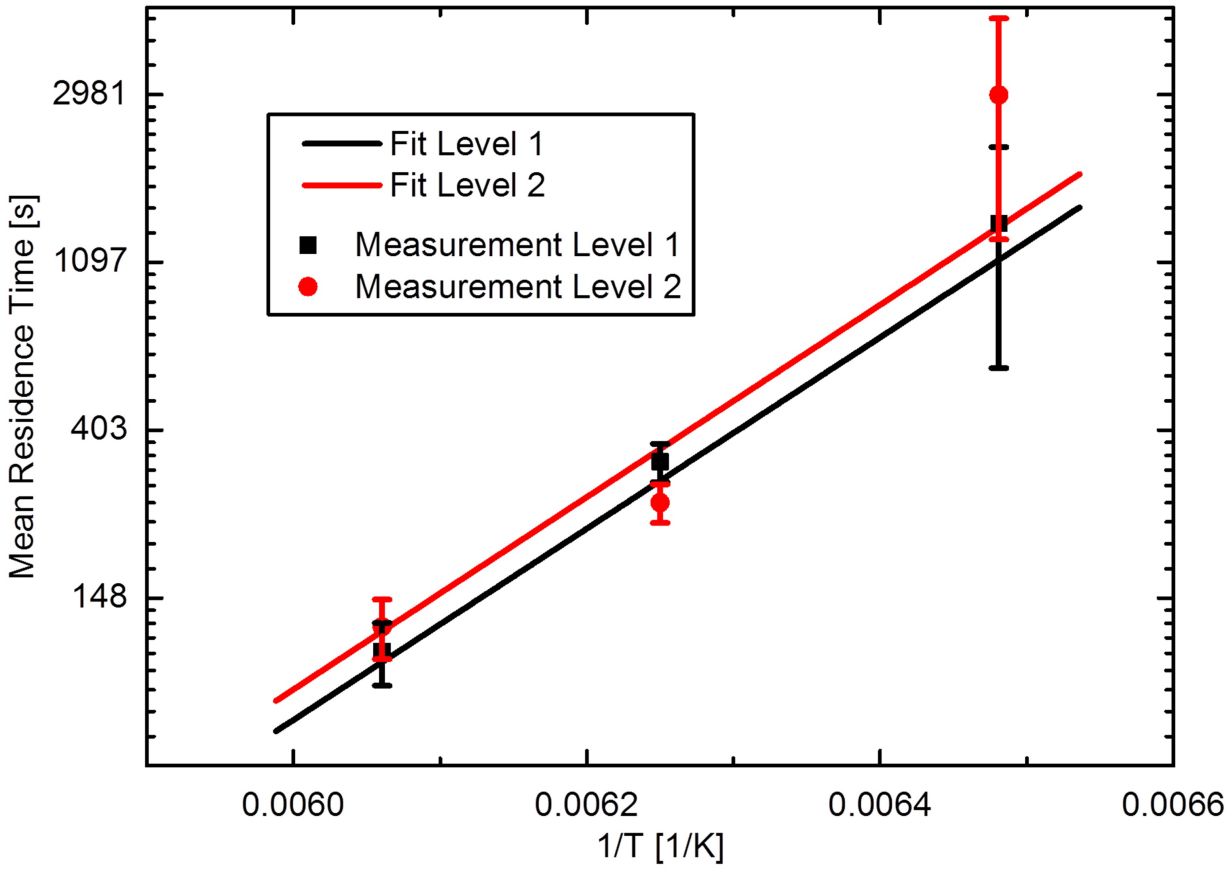

Figure 40: Fit of the evaluated mean residence times for the nanowire sample. The dots represent the values extracted from the measurements including their standard error. The lines show the fit performed with the described mean residence time expression.

parallel to the elongation direction of the larger cluster. In its energy landscape, one can see six minima, named A - F, which are caused by the magnetocrystalline anisotropy. The shape anisotropy brings in a two-fold symmetry with indentations around 0 ° and 180 °. The lowest resistance level R1 is solely fed by minimum C. Level R2 and R3 are degenerate with R2 being measured when the magnetization is in minimum B or D and R3 in minimum A, E and F. This yields the observed three-level-distribution of the resistance.

The depopulation channels for level R1 are C $\rightarrow$ B and C $\rightarrow$ D. Resistance level R2 can be left with B $\rightarrow$ A, B $\rightarrow$ C, D $\rightarrow$ C and D $\rightarrow$ E. Level R3 is left over A $\rightarrow$ F, A $\rightarrow$ B and E $\rightarrow$ D, while changes in-between the neighboured minima E, F and A cannot be resolved by measuring the resistance. Based on these depopulation channels, the fit functions for the mean residence

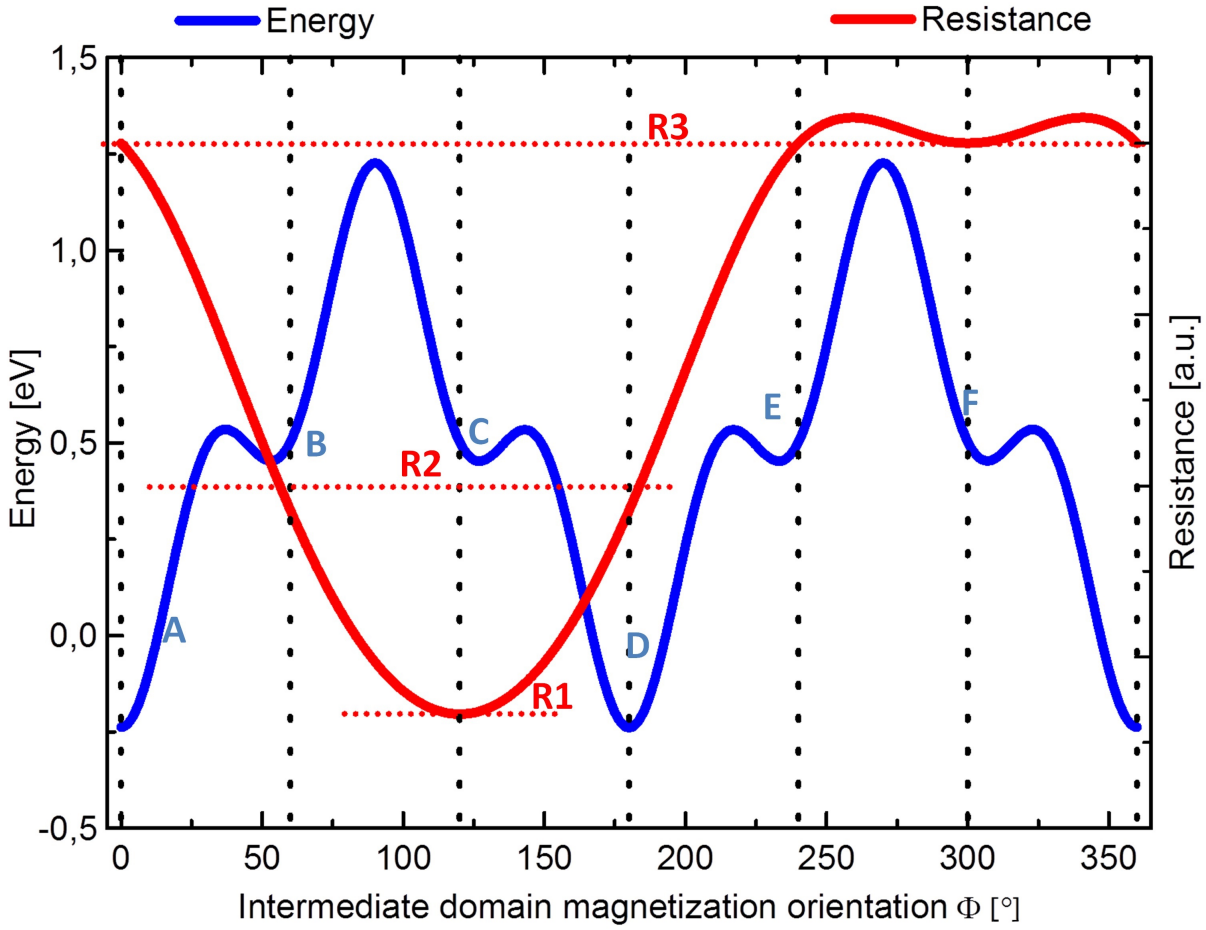

Figure 41: Energy landscape (blue) and resistance characteristics (red) for the in-plane magnetization orientation of the intermediate domain in the angled nanocluster arrangement. The three resistance levels arising from the six minima are shown as dashed red lines.

times can be set up as follows:

$$\tau_1 = (f_{0,Level1} \cdot (e^{-\frac{E_{C\to B}}{k_B T}} + e^{-\frac{E_{C\to D}}{k_B T}}))^{-1}, \tag{31}$$

$$\tau_2 = (f_{0,Level2} \cdot (e^{-\frac{E_{B\to A}}{k_B T}} + e^{-\frac{E_{B\to C}}{k_B T}} + e^{-\frac{E_{D\to C}}{k_B T}} + e^{-\frac{E_{D\to E}}{k_B T}}))^{-1} \text{ and} \tag{32}$$

$$\tau_3 = (f_{0,Level3} \cdot (e^{-\frac{E_{A\to B}}{k_B T}} + e^{-\frac{E_{E\to D}}{k_B T}}))^{-1}. \tag{33}$$

During the fit process, it was found that the use of individually defined attempt frequencies for each mean residence time improves the quality of the fit curves considerably. The fits which were obtained using these functions can be seen in figure 42. All three fits are in accordance with the measured values within their error bars, except for two values for levels 2 and 3 at the intermediate temperature. The used fit parameters are $f_{0,\text{ Level 1}}$=0.856 Hz, $f_{0,\text{ Level 2}}$=0.085 Hz, $f_{0,\text{ Level 3}}$=0.413 Hz, $V_\text{D} = 3.573 \times 10^{-25}\, m^3$ and $K_\text{shape} = 6.82 \times 10^5\, \frac{J}{m^3}$. The influence of the coupling terms on the fit quality was found to be negligible, thus they were set to zero here.

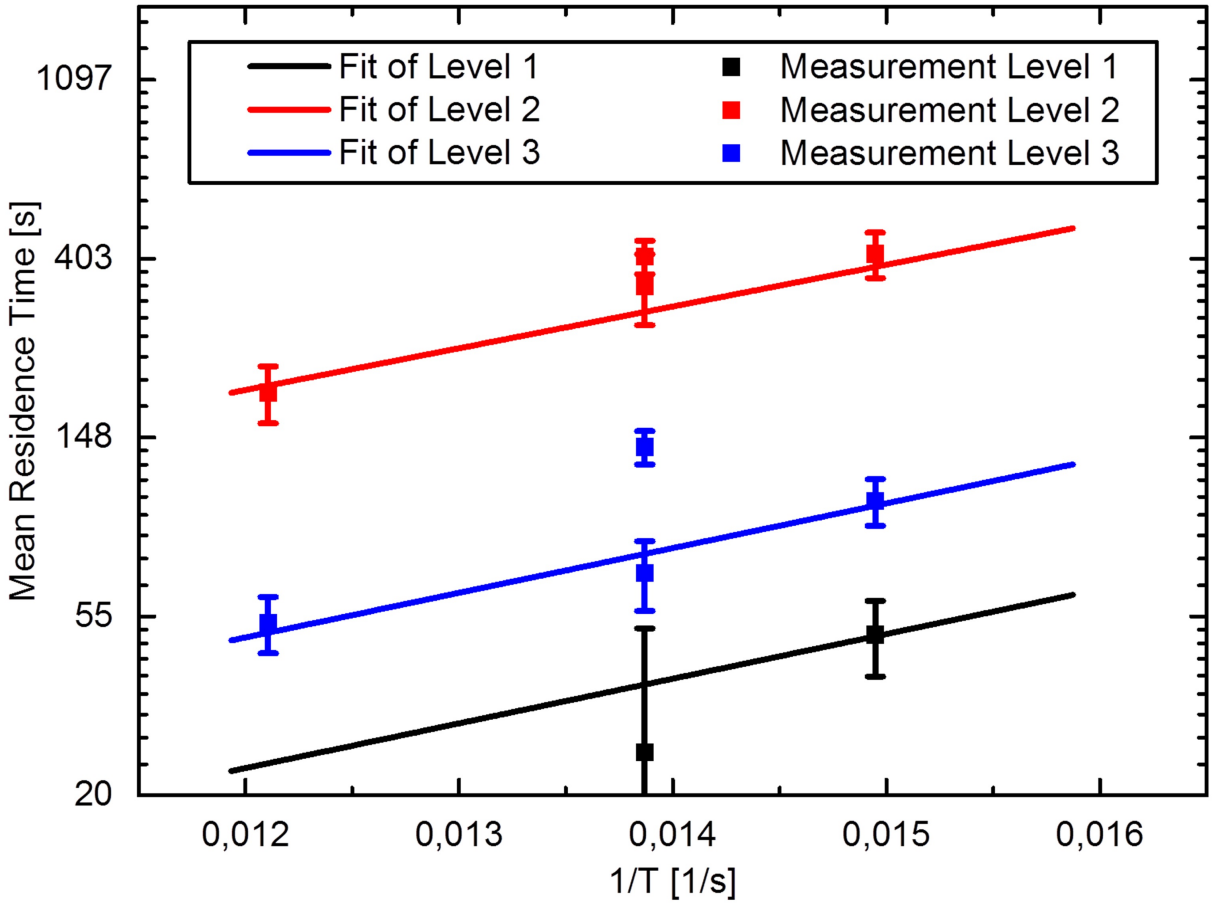

Figure 42: Fit of the evaluated mean residence times for the angled nanocluster arrangement. The dots represent the values extracted from the measurements including their standard error. The lines show the fit performed with the described mean residence time expression.

In this case, several issues mark that the shown model, which is comparatively simple with only one variable domain magnetization orientation, meets its limits. The good agreement between fit function and measured values can only be reached using different and remarkably low values for the attempt frequencies. These values are all below 1 Hz and thus differ by several orders of magnitude from the usually reported attempt frequencies of about 10^{10} Hz.[Les96] However, Bode et al. reported a strong scattering between 10^{-8} Hz and 10^{11} Hz concerning their attempt frequency calculations, due to large uncertainties in the measured parameters. Since the angled nanocluster sample poses a more complex volume morphology compared to the MnAs nanowire, it can be supposed that the three-domain-model as applied here is already too simplified to face this complexity.

For both sample geometries, the fit value for the intermediate domain volume is small compared

to the size of the nanoclusters. $V_{\mathrm{D}} = 3.814 \times 10^{-25}\, m^3$ for the nanowire and $V_{\mathrm{D}} = 3.573 \times 10^{-25}\, m^3$ for the angled arrangement both are in the range of a cubic volume with an edge length of only several nanometers. This indicates that the inversion of the fluctuating volume is performed in a nucleation process. This will be discussed in the following chapter 6.2.4.

Despite the good accordance between measurements and fit curves, the presented model has its limitations. As a three-domain model with only one (intermediate) domain being subject to a thermal change, it does not take into account that a thermal activation of domain walls can result in the formation of a more complex domain structure. Besides that, possible thermally activated effects of the adjacent, large domains are also not covered. The set of free parameters for the fit, including the attempt frequencies and the coupling constants, allows a broad adaption between fit and experiment. In the publication of Fischer et al. regarding the observed RTN effects, the three-domain model for the angled system is based on a slightly different external domain configuration.[Fi15b] Here, the external domain magnetizations are considered to have a relative angle of 60 ° instead of the 120 °-configuration shown in this chapter. In case of the 120 °-configuration, the accordance between fit and experiment is slightly better regarding the middle and high resistance levels. However, a high relative angle of the external magnetizations stands in conflict to the MFM observations, where angled systems tend to expose low relative angles after being exposed to an external magnetic field. Regarding this observation, the 60 °-configuration appears to be more probable. Against this background, both discussed configurations can be understood as valid compromises between the accordance of experimentally observed phenomena and the adaption of a simplified theoretical model.

6.2.4 Domain wall migration

The magnetization reversal mechanism of a domain depends mainly on its size. The crucial limit for this size is the critical length $l_{crit} = 2\pi L = 2\pi\sqrt{\frac{A}{k_{eff}}}$, depending on the magnetic exchange stiffness A and the effective anisotropy constant k_{eff}.[Bod04] Small particles with dimensions beyond the half of this critical length perform a magnetization reversal in coherent rotation, i.e. the whole particle changes its magnetization instantly. In bigger particles, a nucleation process takes place, where the magnetization reversal starts in a small volume and spreads over the rest of the particle, while a domain wall migration is observable.

Two observations on the thermally induced resistance jumps indicate that the magnetization reversal in the intermediate domain takes place in a nucleation process.
In the mean residence time fits, the intermediate domain volume served as a variable fit parameter.

In both cases, the found volumina have dimensions much smaller than those of the nanocluster systems studied. For the nanowire arrangement, the domain volume of $V_\mathrm{D} = 3.814 \times 10^{-25}\,m^3$ corresponds to a cube with an edge length of 7.25 nm. In case of the angled arrangement, a domain volume of $V_\mathrm{D} = 3.573 \times 10^{-25}\,m^3$ is found corresponding to a 7.1 nm large cube. The exchange stiffness for MnAs has been assumed to $10^{-11}\,\frac{J}{m}$ by Engel-Herbert et al., and with the magnetocrystalline anisotropy constant determined by Elm as $1.62 \cdot 10^5\,\frac{J}{m^3}$, one achieves a critical length of 49 nm.[El10b Eng06] The found volume sizes are smaller than half of this length, however, it is still one magnitude below the longest cluster extent. This leads to the assumption that the fit values for the intermediate domain volume can be interpreted as the initial nuclei for the reversal of a larger area's magnetization.

The second indication for a nucleation process is the profile of the observed jump features. If one takes a closer look at the jumps, one can observe that they extend over several measurement points in nearly all cases for the two samples. Figure 43 shows exemplarily one jump per sample depicting this behavior. The jumping sequence is defined as the duration over which the resistance value performs a monotonous increase. In most cases, this duration extends over about four measurement steps, as shown for the two jumps in figure 43. This observation is suspected to be caused by the nucleation process of the intermediate domain's magnetization reversal. Assuming that this nucleation starts at one side of the domain in a small volume below the critical length and extends over the whole width of the cluster arrangement, one can approximate a value for the domain wall migration velocity. One measurement point takes around 15 s of time, and the cluster arrangements have a width of around 300 nm. With a four point lasting jump, one can calculate a domain wall speed of $5\,\frac{nm}{s}$.

This value is magnitudes lower than domain wall velocities in systems where the wall is driven by external influences such as a current or an external magnetic field. Here, the velocities can be as fast as $100\,\frac{m}{s}$ or higher.[Par08 Mei07] However in case of thermally activated domain wall migration, one can observe significantly lower values for the velocity. In the manner of a zero-point calibration for the observation of spin-transfer torque driven domain wall migration, Alvarez et al. have observed thermally activated domain wall velocities in the range of around $10\,\frac{nm}{s}$, which is in accordance to the velocities observed in the shown measurements.[Alv10]

Concluding, one can state that a nucleation process as magnetization reversal mechanism in the case of the thermally activated jumps in MnAs nanoclusters is much more likely than observing coherent magnetization changes. The large cluster extension compared to the critical length indicates that a coherent magnetization reversal is comparatively improbable. In addition,

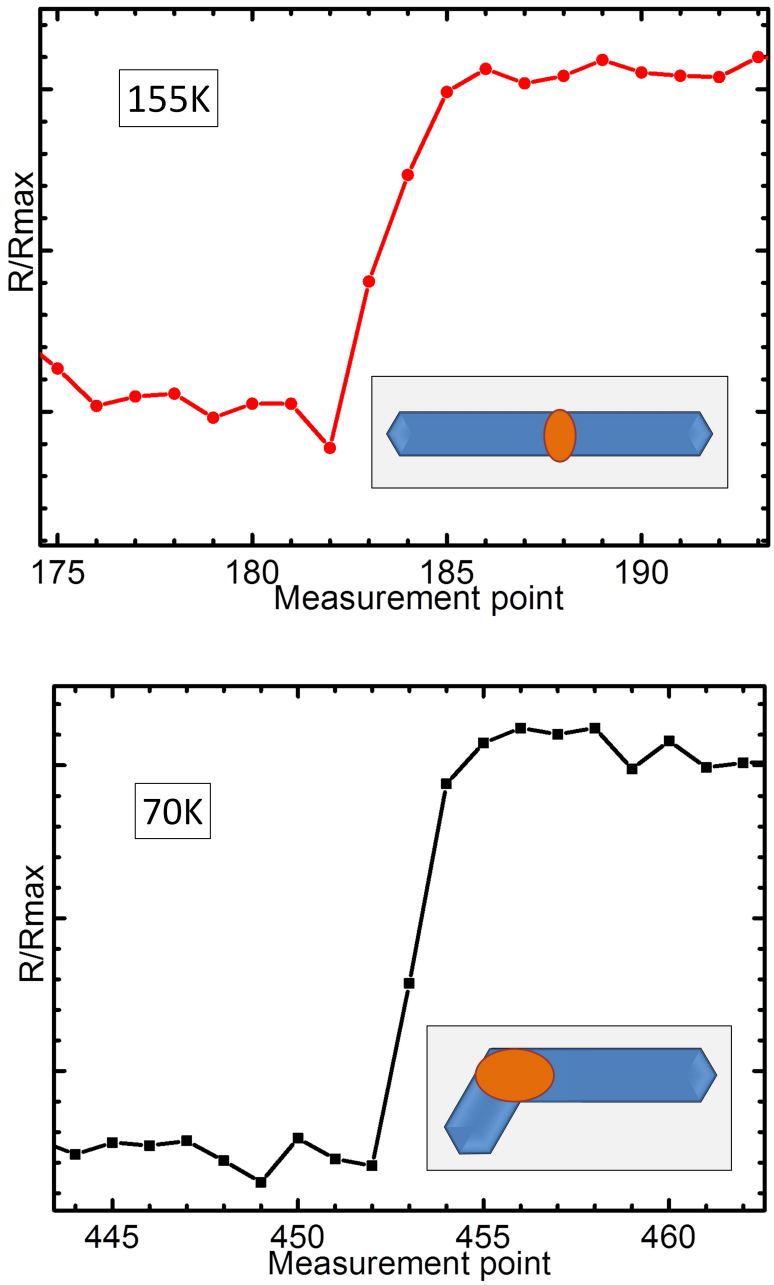

Figure 43: Two exemplary resistance jumps extracted from measurements on the nanowire sample at 155 K (left) and the angled nanocluster arrangement at 70 K (right). The extension of the jump over several measurement points is clearly visible.

the observed jumps show a time dependence indicating a thermally driven domain wall migration with a velocity comparable to earlier observations.

6.2.5 Influence of the external magnetic field

Up to this point, all shown temperature-dependent measurements have been performed without the influence of an external magnetic field. However, this topic is quite interesting in combination with the observed thermally activated jumps and thus will be discussed in the following.

The energy landscape for the intermediate domain includes a Zeeman term representing the energy arising from the coupling between the domain's magnetization and an external magnetic field B. With rising external field, the Zeeman term becomes stronger compared to the field-independent contributions from anisotropy and inter-cluster coupling. At smaller fields, this causes a tilt and a flattening of the existing minima, since the Zeeman term has the profile of a cosine with a 2π-symmetry, while the shape anisotropy energy has a π-symmetry and the magnetocrystalline anisotropy energy has a $\frac{\pi}{3}$-symmetry. With further increasing field, the minima disappear and one global Zeeman minimum in the direction of the external field remains. This effect can also be seen in figures 26 and 27. Figure 44 shows the time-dependent measurements on the angled, merged nanocluster sample which is shown in figure 31(bottom). The measurements were performed with applied external magnetic fields of five different field values, all with an orientation in sample plane and perpendicular to the elongation direction of the larger part of the cluster, i.e. the $(\bar{1}10)$-direction of MnAs. The sample temperature was held constant at 100 K and thus slightly higher than in the case of the statistically evaluated measurements. At zero field, one can observe well-defined resistance jumps comparable to the ones shown above. However, they are not restricted to a recurrent set of levels, which can be related to the higher sample temperature inducing a more complex micromagnetic structure beyond the operating range of the presented three-domain model. At an external field of 1 T, one can observe that the large, well-defined jumps become less probable. In addition, many smaller jumps near the time resolution-induced detection limit of the measurement apparatus appear, which look like a kind of noise. For higher fields above 3 T, no jumps can be observed in this sample.

The reason for this observation can be found in the influence of the external field on the energy landscape. At 1 T, the minima get flattened and tilted but are still existing, which enables the magnetization to perform jumps between them which can be seen in the resistance. However, the energy barriers become smaller due to the tilt in the energy landscape caused by the Zeeman energy. At higher fields, no minima but the single Zeeman minimum are remaining. Thus, no resistance jumps can be observed any more at those field values.

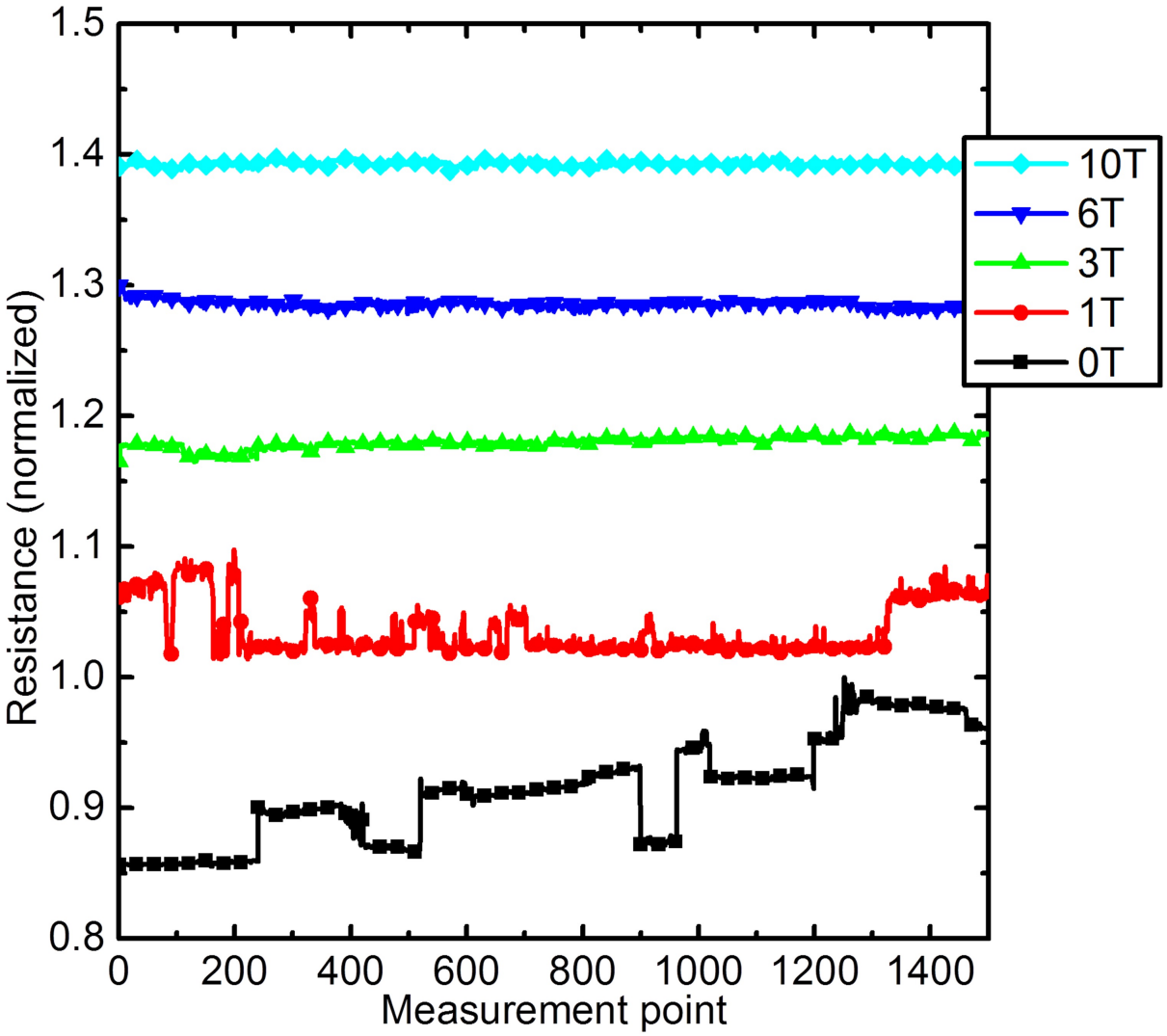

Figure 44: Time-dependent measurements on the angled nanocluster arrangement performed at different constant external magnetic fields perpendicular to the $(\bar{1}10)$-direction in sample plane.

Part III
Conclusion

7 Summary

The aim of this work was the realization of GMR-like magneto-electronic structures based on SA-MOVPE grown MnAs nanoclusters. New nanocluster arrangement layouts have been developed, numerous single clusters and arrangements have been contacted and investigated, and also, a first GMR-like MR behavior in such a structure has been observed, discussed and published.[Fi15a] However, the process leading to this achievement led also to new findings concerning the synthesis and investigation of MnAs nanoclusters as well as the interpretation of the observed interplay of magnetoelectronic and thermally activated phenomena.[Fi15b]

At the beginning of this work, a first standardized process for the synthesis of single-contacted MnAs nanoclusters had already been established. This process has been continuously further developed and improved. The parameters for the MnAs nanocluster growth have been adapted regarding a realization of a better isolation between clusters and substrate using a thicker AlGaAs layer. The alignment procedure for the contact lithography has been improved to a higher stability and thus better success rate in the contacting process. In addition, the application of a polymer cover layer has been introduced to prevent the nanoclusters being affected by atmospheric condensing water.

Improvement and innovation also had to take place concerning the magnetoresistance measurement process. The practiced measurement routines had to be adapted for the investigation of very small functional structures. In particular, this comprises the introduction of procedures preventing a sample damage caused by electrostatic discharges by applying improved electrical grounding equipment on the user and the measuring equipment. Additional, the existing measurement programs have been modified to avoid a damage of the clusters caused by voltage peaks occurring during contact switching sequences.

For the understanding of the MR characteristics of MnAs nanoclusters, a high number of resistance measurements on various samples with different geometries and arrangement setups under differently combined external influences has been performed. It has been found that a GMR-like spin valve characteristics is realized in an arrangement of two elongated, clearly separated nanoclusters connected by a gold layer. This observation is further explained con-

sidering the special magnetic anisotropy conditions in elongated MnAs nanoclusters, which is described using an energy landscape comprising magnetocrystalline and shape anisotropy as well as coupling effects between the clusters and to the external magnetic field. The comparatively low MR ratio in this case is explained by shunt currents passing parallel to the cluster arrangement through the matrix. This phenomenon is related to the observation of a linear MR effect which is more or less dominant, depending on the isolation between clusters and matrix as well as on the disorder and Mn doping in the respective matrix areas. The influence of thermal activation on the GMR-like characteristics is also considered.

Besides the first observation of a spin-valve behavior in a MnAs nanocluster arrangement, the influence of thermal energy on the MR behavior has been a major part of this work. In numerous measurements, a high amount of spontaneous jumps occurred which could not be related to any recurring external influences and thus had to be explained by internal processes. The investigation of two compact, merged nanocluster arrangements over a longer measurement time with constant external parameters allowed a quantitative approach to this issue, since the observed resistance jumps occurred between recurring resistance levels. The statistical evaluation of these jumps showed a relation to the sample temperature, which could be explained by the Néel-Brown-law in combination with the occurrence of nucleation-induced magnetization reversal processes. Here, a quantitative analysis was possible applying a simple three-domain-model as a base for the setup of a fit function.

8 Outlook

Selective-area grown MnAs as a material for functional micro- and nanostructures still has a newcomer position amongst materials which are used for the synthesis of magnetoelectronic nanostructures. Most work related to MnAs is performed on its combination with GaAs as a diluted magnetic semiconductor or hybrid system.[Ohn96]

One of the most influential parameters affecting the observation of spin-valve like behavior in the MnAs nanocluster structures is the temperature. Since the Curie-temperature of MnAs is slightly above room temperature, the expectation for nanoclusters, which are large enough to be above the critical length and small enough to form a single magnetic domain, was that temperatures below T_C do not significantly affect their functionality. However, when the formation of a non-trivial domain structure occurs, it becomes possible that small volumes in the cluster systems form domains of sufficiently small size, which can undergo changes caused by thermal excitation. The domain walls leading to the formation of this micromagnetic structure

can be established at incisions of the cluster shape.[Bru99] Nucleation processes can initialize the inversion of bigger volumes strongly affecting the observed MR characteristics. The quintessence of this finding concerning future device setups based on MnAs clusters is that the setups should be based on morphologically well-defined, simply shaped and sufficiently separated nanoclusters, since here, one finds the highest probability of achieving a single-domain magnetic structure. An ideal cluster size should be below the dimensions of the investigated, merged systems exposing thermally activated effects in chapter 6.2, but still be above the critical length for coherent thermal rotation discussed in chapter 6.2.4, which is important for the achievement of working temperatures near room temperature.

The MR performance of the investigated structures has also been influenced by the quality of the isolation between the substrate and the nanocluster arrangements. In most of the measurements, a strong and dominant linear magnetoresistance was observed, whose MR ratio was often significantly higher than the MR of the observed jumps. This effect is related to shunt currents passing through the matrix, which are not experiencing spin-dependent transport effects in the cluster arrangement. This lowers the MR ratio of the jumps, which in contrast to the linear MR are the interesting and desired feature for the observations. The linear MR of the matrix is caused by disordered GaAs:Mn in the area surrounding the nanoclusters, which originates from the diffusion of Mn into the substrate during growth. Possible approaches to overcome this issue are an even thicker AlGaAs isolation layer, lowering the diffusion of Mn, or the use of other, isolating substrates. First work on this possible improvements has been already performed by developing alternative buffer layers for growth on insulating substrates like glass.[Sak15]

With these improvements, it is imaginable that GMR-like MnAs nanocluster arrangements with better MR ratios, well-defined functionality devoid of thermally activated effects and higher working temperatures can be realized. The proof of MR jumps with significant ratios has been given with this work, and the tools for the needed improvements are abundant, which gives the evidence for SA-MOVPE grown MnAs nanoclusters being a highly interesting model system for future planar magnetoelectronics.

Part IV

Appendix

9 Bibliography

References

[Aha64] Aharoni, A. Thermal Agitation of Single Domain Particles, *Phys. Rev.* **1964**, 135, A447-A449

[Ala11] del Alamo, J.A. Nanometre-scale electronics with III-V compound semiconductors *Nature* **2011**, 479, 317

[All94] Ultrathin films: magnetism on the microscopic scale, *J. Magn. Mag. Mat* **1994**, 129, 160-185

[All02] Allwood, D.A.; Xiong, G.; Cooke, M.D.; Faulkner, C.C.; Atkinson, D.; Vernier, N.; Cowburn, R.P. Submicrometer Ferromagnetic NOT Gate and Shift Register, *Science* **2002**, 296, 2003-2006 **2010**, 104, 137205

[All05] Allwood, D.A.; Xiong, G.; Faulkner, C.C.; Atkinson, D.; Petit, D.; Cowburn, R.P. Magnetic Domain-Wall Logic, *Science* **2005**, 309, 1688

[Alv10] Alvarez, L.S.E.; Wang, K.Y.; Lepadatu, S.; Landi, S.; Bending, S.J., Marrows, C.H. Spin-Transfer-Torque-Assisted Domain-Wall Creep in a Co/Pt Multilayer Wire, *Phys. Rev. Lett.* **2010**, 104, 137205

[Atk03] Atkinson, D; Allwood, D.A.; Xiong, G.; Cooke, M.D.; Faulkner, C.C.; Cowburn, R.P. Magnetic domain-wall dynamics in a submicrometre ferromagnetic structure, *Nature Materials* **2003**, 2, 85

[Aws07] Awschalom, D.D.; Flatte, M.E. Challenges for semiconductor spintronics, *Nature Physics* **2007**, 3, 153

[Bai88] Baibich, M.N.; Broto, J.M.; Fert, A.; Nguyen Van Dau, F.; Petroff, F. Giant Magnetoresistance of (001)Fe/(001)Cr Magnetic Superlattices, *Phys. Rev. Lett.* **1988**, 61, 2472-2475

[Bel06] Beleggia, M.; De Graef, M.; Millev, Y.T. The equivalent ellipsoid of a magnetized body, *J. Appl. Phys. D* **2006**, 39, 891-899

[Bin89] Binasch, G.; Gruenberg, P.; Saurenbach, F.; Zinn, W. Enhanced Magnetoresistance in layered Magnetic Structures with Antiferromagnetic Interlayer Exchange, *Phys. Rev. B* **1989**, 39, 4828-4830

[Bod04] Bode, M.; Pietzsch, O., Kubetzka, A.; Wiesendanger, R. Shape-Dependent Thermal Switching Behavior of Superparamagnetic Nanoislands, *Phys. Rev. Lett.* **2004**, 92, 067201-1 - 067201-4

[Boe90] Böer, K.W. Survey of semiconductor physics, *Van Nostrand Reinhold, New York* **1990**, ISBN 0-442-23793-6

[Bro63] Brown, W.F. Thermal Fluctuations of a Single-Domain Particle, *Phys. Rev.* **1963**, 130, 1677-1686

[Bru99] Bruno, P. Geometrically Constrained Magnetic Wall, *Phys. Rev. Lett.* **1999**, 83, 2425-2428

[Che11] Chen, L.; Yang, X.; Yang, F.; Zhao, J.; Misuraca, J.; Xiong, P.; von Molnár, S. Enhancing the Curie Temperature of Ferromagnetic Semiconductor (Ga,Mn)As to 200 K via Nanostructure Engineering, *Nano Lett.* **2011**, 11, 2584-2589

[Chr94] Christensen, N.E.; Gorczyca, I. Optical and structural properties of III-V nitrides under pressure, *Phys. Rev. B* **1994**, 50, 4397-4415

[Cof12] Coffey, W.T.; Kalmykov, Y.P. Thermal fluctuations of magnetic nanoparticles: Fifty years after Brown, *J. Appl. Phys.* **2012**, 112, 121301

[Das03] Das, A.K.; Pampuch, C.; Ney, A.; Hesjedal, T.; Däweritz, L.; Koch, R; Ploog, K.H. Ferromagnetism of MnAs Studied by Heteroepitaxial Films on GaAs(001), *Phys. Rev. Lett.* **2003**, 91, 087203-1

[De63a] De Blois, R.W.; Rodbell, D.S.: Magnetic First-Order Phase Transition in Single-Crystal MnAs, *Phys. Rev.* **1963**, 130, 1347-1360

[De63b] De Blois, R.W.; Rodbell, D.S. Magnetic First Order Phase Transition and Anisotropy in Single Crystal MnAs, *J. Appl. Phys.* **1963**, 34, 1101-1103

[Dic93] Dickson, D.P.E.; Reid, N.M.K.; Hunt, C.; Williams, H.D.; El-Hilo, M.; O'Grady, K. Determination of f_0 for fine magnetic particles, *J. Magn. Magn. Mater.* **1993**, 125, 345-350

[Die94] , Dieny, B. Giant magnetoresistance in spin-valve multilayers, *J. Magn. Mag. Mat.* **1994**, 136, 335-359

[Eid13] Eid, K.F.; Ocola, L.E.; Liu, X.; Furdyna, J.K. Large antisymmetric magnetoresistance across chemically etched GaMnAs nanoconstrictions, *Appl. Phys. Lett.* **2013**, 102, 242407

[Elm08] Elm, M.T.; Klar, P.J.; Heimbrodt, W.; Wurstbauer, U.; Reinwald, M; Wegscheider, W. Annealing-induced transition from a (311) A-oriented Ga0.98Mn0.02As alloy to a GaMnAs/MnAs hybrid structure studied by angle-dependent magnetotransport, *J. Appl. Phys.* **2008**, 103, 093710

[El10a] Elm, M.T.; Michel, C.; Stehr, J.; Hofmann, D.M.; Klar, P.J.; Ito, S.; Hara, S.; Krug von Nidda, H.-A. Comparison of the magnetic properties of GaInAs/MnAs and GaAs/MnAs hybrids with random and ordered arrangements of MnAs nanoclusters, *J. Appl. Phys.* **2010**, 107, 013701

[El10b] Elm, M.T. Tuning the magnetic interactions in GaAs:Mn/MnAs hybrid structures by controlling shape and position of MnAs nanoclusters, *Dissertation*, Justus-Liebig-Universität Gießen, **2010**

[El11a] Elm, M.T.; Klar, P.J.; Ito, S.; Hara, S. Influence of ordered arrangements of cluster chains on the hopping transport in GaAs:Mn/MnAs hybrids at low temperatures, *Phys. Rev. B* **2011**, 83, 235305

[El11b] Elm, M.T.; Klar, P.J.; Ito, S.; Hara, S.; Krug von Nidda, H.-A. Effect of the cluster magnetization on the magnetotransport at low temperatures in ordered arrays of MnAs nanoclusters on (111)B GaAs, *Phys. Rev. B* **2011**, 84, 035309

[Eng06] Engel-Herbert, R., Hesjedal, T., Schaadt, D.M., Däweritz, L., Ploog, K.H. Micromagnetic properties of MnAs(0001)/GaAs(111) epitaxial films, *Appl. Phys. Lett.* **2006**, 88, 052505

[Fi15a] Fischer, M.; Elm, M.T.; Sakita, S.; Hara, S.; Klar, P.J. Magnetoresistance effects and spin-valve like behavior of an arrangement of two MnAs nanoclusters, *Appl. Phys. Lett.* **2015**, 106, 032401

[Fi15b] Fischer, M.; Elm, M.T.; Kato, H.; Sakita, S.; Hara, S.; Klar, P.J. Analysis of the magnetic random telegraph noise in individual arrangements of a small number of coupled MnAs nanoclusters, *Phys. Rev. B* **2015**, 92, 165306

[Fre06] Freescale Semiconductor, Inc. Freescale Leads Industry in Commercializing MRAM Technology, *press release*, July, 10, **2006**

[For08] Fortuna, S.A.; Wen, J.; Chun, I.S.; Xiuling, L. Planar GaAs Nanowires on GaAs (100) Substrates: Self-Aligned, Nearly Twin-Defect Free, and Transfer-Printable, *Nano Lett.* **2008**, 8, 4421-4427

[Gid05] Giddings, A.D.; Khalid, M.N.; Jungwirth, T.; Wunderlich, J.; Yasin, S.; Campion, R.P.; Edmonds, K.; Sinova, J.; Ito, K.; Wang *et al.* Large Tunneling Anisotropic Magnetoresistance in (Ga,Mn)As Nanoconstrictions, *Phys. Rev. Lett.* **2005**, 94, 127202

[Gou07] Gould, C.; Pappert, K.; Schmidt, G; Molenkamp, L.W. Magnetic Anisotropies and (Ga,Mn)As-based Spintronic Devices, *Adv. Mat.* **2007**, 19, 323-340

[Har06] Hara, S.; Fukui, T. Hexagonal ferromagnetic MnAs nanocluster formation on GaInAs/InP(111)B layers by metal-organic vapor phase epitaxy, *Appl. Phys. Lett.* **2006**, 89, 113111

[Har08] Hara, S.; Kawamura, D.; Iguchi, H.; Motohisa, J.; Fukui, T. Self-assembly and selective-area formation of ferromagnetic MnAs nanoclusters on lattice-mismatched semiconductor surfaces by MOVPE, *J. Cryst. Growth* **2008**, 310, 2390-2394

[Har12] Hara, S; Sakita, S.; Yatago, M. Selective-Area Growth and Electrical Characterization of Hybrid Structures between Semiconducting GaAs Nanowires and Ferromagnetic MnAs Nanoclusters, *J. J. Appl. Phys.* **2012**, 51, 11PE01

[Har02] Hartmann, T.; Lampalzer, M.; Klar, P.J.; Stolz, W.; Heimbrodt, W.; Krug von Nidda, H.-A.; Loidl, A.; Svistov, L. Ferromagnetic resonance studies of (Ga,Mn)As with MnAs clusters, *Physica E* **2002**, 13, 572-576

[Har03] Hartmann, T. Experimentelle Untersuchungen am magnetischen Hybridsystem (Ga,Mn)As / MnAs, *Dissertation*, Philipps-Universität Marburg **2003**

[Hei10] Heiliger, C.; Czerner, M.; Klar, P.J.; Hara, S. Magnetic Sensor Devices Based on Ordered Planar Arrangements of MnAs Nanocluster, *IEEE T. Magn.* **2010**, 46, 1702-1704

[Hol05] Holub, M.; Shin, J.; Chakrabarti, S., Bhattacharya, P. Electrically injected spin-polarized vertical-cavity surface-emitting lasers, *Appl. Phys. Lett* **2005**, 87, 091108

[Iba09] Ibach, H.; Lüth, H. Festkörperphysik, *Springer-Verlag Berlin Heidelberg* **2009**, ISBN 978-3-540-85794-5

[Ito09] Ito, S.; Hara, S.; Wakatsuki, T.; Fukui, T. Magnetic domain characterizations of anisotropic-shaped MnAs nanoclusters position-controlled by selective-area metal-organic vapor phase epitaxy, *Appl. Phys. Lett.* **2009**, 94, 243117

[Jag96] Jäger, E.; Perthel, R. Magnetische Eigenschaften von Festkörpern, *Akademie Verlag, Berlin*, **1996**

[Joh85] Johnson, M.; Silsbee, R.H. Interfacial charge-spin coupling: Injection and detection of spin magnetization in metals, *Phys.. Rev. Lett.* **1985**, 55, 1790-1793

[Joh10] Johnson, H.G., Bennett, S.P., Barua, R., Lewis, L.H., Heiman, D. Universal properties of linear magnetoresistance in strongly disordered MnAs-GaAs composite semiconductors, *Phys. Rev. B* **2010**, 82, 085202

[Jul75] Julliere, M. Tunneling between ferromagnetic films, *Phys. Lett. A* **1975**, 54A, 225-226

[Jun05] Jungwirth, T.; Wang, K.Y.; Mašek, J.; Edmonds, K.W.; König, J.; Sinova, J.; Polini, M.; Goncharuk, N.A.; MacDonald, A.H.; Sawicki, M.; Rushfort, A.W.; Campion, R.P.; Zhao, L.X.; Foxon, C.T.; Gallagher, B.L. Prospects for high temperature ferromagnetism in (Ga,Mn)As semiconductors, *Phys. Rev. B* **2005**, 72, 165204

[Kae02] Kästner, M.; Däweritz, L.; Ploog, K.H. Surface reconstruction, screw dislocations and anisotropic step flow growth of MnAs on GaAs (111)B substrates, *Surface Science* **2002**, 511, 323-330

[Kas56] Kasteleijn, P.W.; Van Kranendonk, J. Constant Coupling Approximation for Heisenberg Ferromagnetism, *Physica* **1956**, 22, 317-337

[Kat15] Kato, H.; Sakita, S.; Hara, S. Selective-area growth and magnetic characterization of lateral MnAs nanowires, *J. Cryst. Growth* **2015**, 414, 151-155

[Khv13] Khvalkovskiy, A.V.; Apalkov, D.; Watts, S.; Chepulskii, R.; Beach, R.S.; Ong, A.; Tang, X.; Driskill-Smith, A.; Butler, W.H.; Visscher, P.B.; Lottis, D.; Chen, E.; Nikitin, V.; Krounbi, M. Basic principles of STT-MRAM cell operation in memory arrays, *J. Phys. D* **2013**, 46, 074001

[Kit91] Kittel, C. Einführung in die Festkörperphysik, 9. Auflage, *R. Oldenbourg Verlag München Wien* **1991**

[Kit48] Kittel, C. On the Theory of Ferromagnetic Resonance Absorption, *Phys Rev.* **1948**, 73, 155-161

[Kom11] Komagata, K.; Hara, S.; Ito, S.; Fukui, T. Ferromagnetic MnAs Nanocluster Composites Position-Controlled on GaAs (111)B Substrates toward Lateral Magnetoresistive Devices, *Jpn. J. Appl. Phys.* **2011**, 50, 06GH01

[Kru06] Krug von Nidda, H.-A.; Kurz, T.; Loidl, A.; Hartmann, T.; Klar, P.J.; Heimbrodt, W.; Lampalzer, M.; Volz, K.; Stolz, W. Tuning the magnetic properties of GaAs:Mn/MnAs hybrids via the MnAs cluster shape, *J. Phys.: Condens. Matter* **2006**, 18, 6071-6083

[Les96] Leslie-Pelecki, D.L.; Rieke, R.D. Magnetic Properties of Nanostructured Materials, *Chem. Mater.* **1996**, 8, 1770-1783

[Mei07] Meier, G; Bolte, M; Eiselt, R; Krüger, B; Kim, D.-H.; Fischer, P. Direct Imaging of Stochastic Domain-Wall Motion Driven by Nanosecond Current Pulses, *Phys. Rev. Lett.* **2007**, 98, 187202

[Mir04] Mironov, V.L. Fundamentals of Scanning Probe Microscopy, *The Russian Academy of Sciences Institute for Physics of Microstructures, Nizhniy Novgorod, Russia* **2004**

[Mor97] Morishita, Y.; Iida, K.; Abe, J.; Sato, K. Substrate-Orientation Dependence on Structure and Magnetic Properties of MnAs Epitaxial Layers, *Jpn. J. Appl. Phys.* **1997**, 36, L1100-L1103, Part 2, No. 8B

[Mun89] Munekata, H.; Ohno, H.; von Molnar, S.; Segmüller, A.; Chang, L.L.; Esaki, L. Diluted Magnetic III-V Semiconductors, *Phys. Rev. Lett.* **1989**, 63, 1849-1852

[Nee49] Néel, L. Influence des fluctuations thermiques sur l'aimantation de grains ferromagnétiques très fins, *CR Hebd. Acad. Sci.* **1949**, 228(8), 664-666

[Ohn96] Ohno, H.; Shen, A.; Matsukura, F.; Oiwa, A; Endo, A.; Katsumoto, S.; Iye, Y. (Ga,Mn)As: A new diluted magnetic semiconductor based on GaAs, *Appl. Phys. Lett.* **1996**, 3, 363-365

[Oka89] Okamoto, M. The As-Mn (Arsenic-Manganese) System, *Bulletin of Alloy Phase Diagrams* **1989**, Vol. 10 No. 5 549-554

[Par05] Parish, M.M.; Littlewood, P.B. Classical magnetotransport of inhomogenous conductors, *Phys. Rev. B* **2005**, 72, 094417

[Pap07] Pappert, K.; Huempfner, S.; Gould, C.; Wenisch, J.; Brunner, K.; Schmidt, G.; Molenkamp, L.W. A non-volatile-memory device on the basis of engineered anisotropies in (Ga,Mn)As, *Nature Phys.* **2007**, 3, 573-578

[Par95] Parkin, S.S.P. Giant Magnetoresistance in Magnetic Nanostructures, *Annu. Rev. Mat. Sci.* **1995**, 25, 357-388

[Par08] Parkin, S.S.P.; Hayashi, M.; Thomas, L. Magnetic Domain-Wall Racetrack Memory, *Science* **2008**, 320, 190-194

[Pet94] Petroff, P.M.; DenBaars, S.P. MBE and MOCVD Growth and Properties of Self-Assembling Quantum Dot Arrays in III-V Semiconductor Structures, *Superlattices and Microstructures* **1994**, 15, 1

[Pri98] Prinz, G.A. Magnetoelectronics, *Science* **1998**, 282, 1660

[Rah01] Rahman, M; Deng, L.G.; van den Berg, J.; Wilkinson, C.D.W. Minimization of dry-etch damage in III-V semicondurctors, *J. Phys. D: Appl. Phys.* **2001**, 34, 2792-2797

[Rei09] Reig, C.; Cubells-Beltran, M.-D.; Ramirez Munoz, D. Magnetic Field Sensors Based on Giant Magnetoresistance (GMR) Technology: Applications in Electrical Current Sensing, *Sensors* **2009**, 9, 7919-7942

[Rey01] Reyntjes, S; Puers, R. A review of focused ion beam applications in microsystem technology, *J. Micromech. Microeng.* **2011**, 11, 287-300

[Sak15] Sakita, S.; Hara, S. Growth of AlGaAs nanostructures on crystallized Al2O3 interlayers for semiconducting nanowire growth on glass substrate, *Jap. J. Appl. Phys.* **2015**, 54, 075504

[Sta59] Stacey, F.D. Thermal Activation of Ferromagnetic Domains, *Proc. Phys. Soc. (London)* **1959**, 73, 136

[Sto39] Stoner, Edmund C. Collective Electron Ferromagnetism. II. Energy and Specific Heat, *Proc. R. Soc. Lond. A* **1939**, 169, 339-371

[Sug02] Sugahara, S; Tanaki, M. Tunneling magnetoresistance in fully epitaxial MnAs/AlAs/MnAs ferromagnetic tunnel junctions grown on vicinal GaAs(111)B substrates, *Appl. Phys. Lett.* **2002**, 80, 1969-1971

[Tan02] Tanaka, M. Ferromagnet (MnAs)/III-V semiconductor hybrid structures, *Semicond. Sci. Technol.* **2002**, 17, 327-341

[Tho57] Thomson, W. On the Electro-Dynamic Qualities of Metals: Effects of Magnetization on the Electric Conductivity of Nickel and of Iron, *Proceedings of the Royal Society of London* **1856-1857**, 8, 546-550

[Wak09] Wakatsuki, T.; Hara, S.; Ito, S.; Kawamura, D.; Fukui, T. Growth Direction Control of Ferromagnetic MnAs Grown by Selective-Area Metal-Organic Vapor Phase Epitaxy, *Jpn. J. Appl. Phys.* **2009**, 48, 014C137

[Wer96] Wernsdorfer, W.; Bonet Orozco, E.; Hasselbach, K.; Benoit, A.; Meier, J.; Ansermet, J.-Ph.; Barbara, B. Nucleation of Magnetization Reversal in Individual Nanosized Nickel Wires, *Phys. Rev. Lett.* **1996**, 77, 1873-1876

[Wer97] Wernsdorfer, W.; Bonet Orozco, E.; Hasselbach, K.; Benoit, A.; Barbara, B.; Demoncy, N.; Loiseau, A.; Pascard, H.; Mailly, D. Experimental Evidence of the Néel-Brown Model of Magnetization Reversal, *Phys. Rev. Lett.* **1997**, 78, 1791-1794

[Wol01] Wolf, S. A.; Awschalom, D. D.; Buhrman, R. A.; Daughton, J. M.; von Molnár, S.; Roukes, M. L.; Chtchelkanova, A. Y.; Treger, D. M.. Spintronics: A Spin-Based Electronics Vision for the Future, *Science* **2001**, 294, 1488-1495

[Ye03] Ye, S.; Klar, P.J.; Hartmann, T.; Heimbrodt, W.; Lampalzer, M.; Nau, S.; Torunski, T.; Stolz, W.; Kurz, T.; Krug von Nidda, H.-A. *et al.* Anisotropy of the magnetotransport in (Ga,Mn)As/MnAs paramagnetic-ferromagnetic hybrid structures, *Appl. Phys. Lett.* **2003**, 83, 3927-3929

10 Acknowledgements

An dieser Stelle möchte ich allen Personen danken, die durch ihr Engagement zum Entstehen dieser Arbeit beigetragen haben:

- Prof. Dr. Peter J. Klar für die Möglichkeit, diese Arbeit in seiner Arbeitsgruppe durchzuführen, sein Vertrauen in mich, und seine vorbildliche, positive Art, die mir oft geholfen hat, Herausforderungen zu meistern und die richtigen Wege zu gehen
- Prof. Dr. Christian Heiliger für die Übernahme des Zweitgutachtens und die gute Zusammenarbeit im Bezug auf die theoretischen Aspekte dieser Arbeit
- Very special thanks to Prof. Dr. Shinjiro Hara for being my host professor during all stays at the Research Center for Integrated Quantum Electronics in Sapporo. He gave me extraordinary support during my research work and life in Japan
- Prof. Dr. Detlev M. Hofmann für die Beteiligung an der Prüfungskommission
- Dr. Matthias Elm für seine umfassende Hilfe bei sämtlichen fachlichen Belangen rund um MnAs-Cluster und das Leben in Japan, sowie für die stets freundschaftliche Zusammenarbeit
- Allen Mitarbeitern und Studierenden der Arbeitsgruppe Klar und des I. Physikalischen Instituts für die positive, produktive und freundschaftliche Arbeitsatmosphäre, insbesondere Dr. Torsten Henning, Martin Becker, Steve Petznick, Dr. Daniel Reppin, Dr. Florian Gather und Andreas Rühl
- All colleagues and students at the RCIQE in Sapporo for their professional support and incredible hospitality during my stays in Japan, especially Shinya Sakita, Hiroaki Kato, Dr. Yoshinori Kohashi, Dr. Eugene Hori and Yusuke Kumazaki
- Markus Szauter und Andreas Katzer für ihren engagierten Einsatz am Helium-Verflüssiger, ohne den die gezeigten Messungen nicht hätten durchgeführt werden können
- Meinen Freunden, die mir stets einen Gegenpol zur Forschungsarbeit geboten haben und für jede zeitliche Einschränkung Verständnis hatten
- Meinen Eltern, die mich durch mein gesamtes Studium und darüber hinaus mit allen Kräften unterstützt haben

11 Selbstständigkeitserklärung

Hiermit versichere ich, die vorgelegte Thesis selbstständig und ohne unerlaubte fremde Hilfe und nur mit den Hilfen angefertigt zu haben, die ich in der Thesis angegeben habe. Alle Textstellen, die wörtlich oder sinngemäß aus veröffentlichten Schriften entnommen sind, und alle Angaben die auf mündlichen Auskünften beruhen, sind als solche kenntlich gemacht. Bei den von mir durchgeführten und in der Thesis erwähnten Untersuchungen habe ich die Grundsätze guter wissenschaftlicher Praxis, wie sie in der Satzung der Justus-Liebig-Universität zur Sicherung guter wissenschaftlicher Praxis niedergelegt sind, eingehalten. Gemäß § 25 Abs. 6 der Allgemeinen Bestimmungen für modularisierte Studiengänge dulde ich eine Überprüfung der Thesis mittels Anti-Plagiatssoftware.

Ort und Datum Martin Fischer